

**University of Alberta**

**Kinetics of Liquid-Solid Reactions in Naphthenic Acid Conversion and  
Kraft Pulping**

by

Ling Yang

A thesis submitted to the Faculty of Graduate Studies and Research  
in partial fulfillment of the requirements for the degree of

Doctor of Philosophy  
in  
Chemical Engineering

Chemical & Materials Engineering Department

©Ling Yang  
Fall 2009  
Edmonton, Alberta

Permission is hereby granted to the University of Alberta Libraries to reproduce single copies of this thesis and to lend or sell such copies for private, scholarly or scientific research purposes only. Where the thesis is converted to, or otherwise made available in digital form, the University of Alberta will advise potential users of the thesis of these terms.

The author reserves all other publication and other rights in association with the copyright in the thesis and, except as herein before provided, neither the thesis nor any substantial portion thereof may be printed or otherwise reproduced in any material form whatsoever without the author's prior written permission.

## **Examining Committee**

Dr. Gray R. Murray, Chemical & Materials Engineering

Dr. Robert E. Hayes, Chemical & Materials Engineering

Dr. Natalia Semagina, Chemical & Materials Engineering

Dr. Jeff M. Stryker, Chemistry

Dr. Marc A. Dube, University of Ottawa

## ABSTRACT

Two liquid-solid reactions, in which the morphology of the solid changes as the reactions proceed, were examined. One is the NA conversion in oil by decarboxylation on metal oxides and carbonates, and the other is the Kraft pulping in which lignin removal by delignification reaction. In the study of the NA conversion, CaO was chosen as the catalyst for the kinetic study from the tested catalysts based on NA conversion. Two reaction mixtures, carrier oil plus commercial naphthenic acids and heavy vacuum gas oil (HVGO) from Athabasca bitumen, were applied in the kinetic study. The influence of TAN, temperature, and catalyst loading on the NA conversion and decarboxylation were studied systematically. The results showed that the removal rate of TAN and the decarboxylation of NA were both independent of the concentration of NA over the range studied, and significantly dependent on reaction temperature. The data from analyzing the spent catalyst demonstrated that calcium naphthenate was an intermediate of the decarboxylation reaction of NA, and the decomposition of calcium naphthenate was a rate-determining step. In the study on the delignification of the Kraft pulping, a new mechanism was proposed for the heterogeneous delignification reaction during the Kraft pulping process. In particular, the chemical reaction mechanism took into account the heterogeneous nature of Kraft pulping. Lignin reacted in parallel with sodium hydroxide and sodium sulfide. The mechanism consists of three key kinetic steps: (1) adsorption of hydroxide and hydrosulfide ions on lignin; (2) surface reaction on the solid

surface to produce degraded lignin products; and (3) desorption of degradation products from the solid surface. The most important step for the delignification process is the surface reaction, rather than the reactions occurring in the liquid phase. A kinetic model has, thus, been developed based on the proposed mechanism. The derived kinetic model showed that the mechanism could be employed to predict the pulping behavior under a variety of conditions with good accuracy.

## **ACKNOWLEDGMENT**

My last few years were not easy, but there have been too many wonderful people helping and supporting me for this journey.

First of all, I would like to thank my advisor, Dr Gray, for adopting me. To me, he is not only my mentor, but also a role model in my life, as he always points out the most important point or direction I need to work on, and always get back to me quickly when I need his help, even he is extremely busy. I also appreciate his understanding and patience through the years, which have allowed me to accomplish my degree although I was away from my husband, lost two advisors, and had my baby in 2006.

I thank Dr. Liu for his advice and support during my first two-year study. Also, I would like to thank Dr. Natalia Semagina, Dr. Robert E. Hayes, Dr. Marc A. Dube, and Dr. Jeffrey M. Stryker for being my committee members.

Among those people, I have to mention Chunli, Lichun, and Chunfeng. They are my best friends and sisters, who helped me so much in these years, especially throughout my pregnancy while my husband was still in the States. I just can't imagine how I could have gone these days without them.

I also thank Brian, Claudia, Shaofeng, Tuyet, Andree, Mildred, and Shihong for their help, cooperation, and friendship.

I would like to thank my husband, my son, and my mom. They are the reasons make me never give up and push me towards the finish line. I want to dedicate all my work to them, who have been waiting for today for so long.

Finally, I would like to thank NSERC and Suncor Energy for financial supports.

SECTION 1	OVERALL INTRODUCTION AND CONTENTS OF THESIS...	1
1.1	Research Objectives.....	3
	References.....	5
SECTION 2	CONVERSION OF NAPHTHENIC ACIDS .....	6
2.1	Literature Review .....	6
2.1.1	Approaches for Removal of NA from Oils.....	6
2.1.2	Catalysts Active for Decarboxylation of NA.....	8
2.1.3	Thermal Decomposition of Carboxylic salts .....	10
2.1.4	Reaction Mechanism of Ketonic Decarboxylation of NA.....	12
2.1.5	Kinetics of decarboxylation of NA.....	17
2.2	Experimental Materials and Methods .....	20
2.2.1	Materials .....	20
2.2.1.1	Naphthenic Acid-2 (NA) .....	20
2.2.1.2	Carrier Oil .....	21
2.2.1.3	HVGO.....	22
2.2.1.4	Catalyst Preparation.....	22
2.2.2	Experimental Equipment .....	24
2.2.3	Reaction Procedure.....	24
2.3	Methods of Analysis .....	26
2.3.1	Characterization of Naphthenic Acid by Gas Chromatography- Electron Impact Mass Spectrometry (GC-MS) .....	26
2.3.1.1	Derivatization Procedure .....	28
2.3.1.2	GC-MS Analysis.....	28
2.3.2	Infrared Spectroscopy (IR) .....	29
2.3.3	TAN Measurement .....	32
2.3.4	Particle Size Distribution.....	36
2.3.5	Scanning Electron Microscope (SEM) .....	36
2.3.6	Energy Dispersive X-ray Spectroscopy (EDX)/SEM Analysis and Auger Electron Spectroscopy (AES) .....	38
2.3.7	X-ray Diffraction (XRD) .....	39
2.3.8	Thermal Gravimetric Analysis (TGA).....	40

2.3.9 GC Analysis.....	40
2.4 Results.....	42
2.4.1 Characterization of Commercial Naphthenic Acid.....	43
2.4.2 Error Analysis.....	46
2.4.3 Catalyst Screening.....	47
2.4.4 Analysis of Solids and Catalysts from Screening Experiments.....	53
2.4.4.1 Particle Size Distribution.....	53
2.4.4.2 SEM.....	54
2.4.4.3 XRD.....	58
2.4.4.4 IR Spectra.....	61
2.4.4.5 TGA.....	63
2.4.5 Solubility of Calcium Naphthenate in the Oil.....	66
2.4.6 Kinetics of Catalytic Decarboxylation of NA in Oil.....	70
2.4.6.1 Influence of Initial TAN.....	73
2.4.6.2 Influence of Catalyst Loading.....	76
2.4.6.3 Influence of Temperature.....	78
2.4.6.4 Activation Energy.....	81
2.4.6.5 Kinetic reactions on Heavy Vacuum Gas Oil (HVGO).....	84
2.4.6.6 Analysis of Solid Samples after the Reaction.....	89
2.4.6.7 Reaction in an impeller-mixed batch reactor.....	92
2.5 Discussion.....	94
2.5.1 Error Analysis.....	94
2.5.2 Characterization of Naphthenic Acid.....	95
2.5.3 Catalyst Screening Based on IR Analysis and TAN Measurement..	96
2.5.4 Evidences of the Formation of Naphthenate Salts in Solid Samples	100
2.5.5 Evidence of Decarboxylation of NA in the Liquid Phase.....	101
2.5.6 Solubility of Calcium Naphthenate in the Oil.....	102
2.5.7 Kinetics of Catalytic Decarboxylation of NA in Oil.....	103
2.5.7.1 Influence of TAN of oil mixtures.....	104
2.5.7.2 Influence of Temperature.....	106
2.5.7.3 Kinetic Reactions of HVGO.....	107

2.5.7.4	Transport Resistance.....	108
2.5.7.5	Proposed mechanism of Liquid-Phase Catalytic Decarboxylation of NA in Oil and Implications for Process Design .....	110
2.6	Conclusions.....	111
2.7	Recommendations.....	113
	References .....	115
SECTION 3 MODEL OF KRAFT PULPING KINETICS .....		124
3.1	Literature Review .....	124
3.1.1	Wood Chemistry and Structure .....	124
3.1.2	The Kraft Pulping Process .....	126
3.1.3	Previous Kinetic Models in Kraft pulping Process.....	127
3.2	Development of the kinetic model.....	137
3.2.1	Reaction Mechanism .....	138
3.2.2	Assumptions .....	140
3.2.3	Adsorption isotherm .....	141
3.2.4	Reaction Rate.....	143
3.3	Estimation of Kinetic Parameters .....	148
3.4	Discussion.....	156
3.4.1	Model Prediction at the Low Liquor-to-wood Ratio .....	156
3.4.2	Heats of Adsorption and Activation Energy.....	160
3.5	Recommendations.....	162
3.5.1	Experimental Studies .....	162
3.5.2	Theoretical Studies .....	163
	References .....	164
APPENDIX A Reaction of Model Compounds of Naphthenic Acids .....		169
APPENDIX B Simulation of Vapor-Liquid Equilibria of Model System Using HYSYS.....		173
APPENDIX C Reaction of the Model System in A Parr Reactor .....		177
APPENDIX D Calibration Curve of TAN Measurement.....		179
APPENDIX E GC Calibration Curves .....		180

Table 2-1 Physical Properties of NA .....	21
Table 2-2 Physical Properties of Carrier Oil .....	21
Table 2-3 Properties of HVGO Used in the Experimental Study.....	21
Table 2-4 Catalyst Preparation .....	23
Table 2-5 Composition of 4% Calcium Naphthenate.....	31
Table 2-6 Recommended Size of Test Portion.....	31
Table 2-7 Parameters Used in the Measurement of the Particle Size Distribution of the Fresh Particles .....	36
Table 2-8 GC Gas Flow Rates .....	41
Table 2-9 Operation Conditions of GC.....	41
Table 2-10 Distribution of Carbon Numbers and Z Families of the NA Sample	44
Table 2-11 Results of TAN Measurement of the Liquid Samples .....	46
Table 2-12 Errors in Measurements of TAN and CO <sub>2</sub> from Different Batches ..	47
Table 2-13 Particle Size Distribution of the Tested Catalysts.....	54
Table 2-14 Results of EDX Analysis of the Fresh Mixture of CaO and Kaolin Clay .....	67
Table 2-15 Results of EDX Analysis of the Post-reacted Mixture of CaO and Kaolin Clay.....	67
Table 2-16 Calculation of Rate Constant of rates of TAN Reduction and CO <sub>2</sub> Production .....	82
Table 2-17 Overall Activation Energies of the Reactions of TAN Reduction and Decarboxylation of NA .....	83
Table 2-18 Decomposition Data on Carbonates .....	98
Table 2-19 the Slope of the Regression Lines of TAN Reduction and CO <sub>2</sub> Production rate.....	108
Table 3-1 Cooking Conditions Used by Santos, et al. (1997).....	148
Table 3-2 Cooking Conditions Used by Wilder and Daleski (1965).....	149
Table 3-3 Kinetic Parameters Estimated from the Experimental Data of Santos, et al.....	151
Table 3-4 Proportionality Factors: F <sub>1</sub> and F <sub>2</sub> .....	160

Table 3-5 Calculation of Activation Energy and Frequency Factors .....	162
Table B-1 Boiling Point Distribution of NA.....	174
Table B-2 BP Distribution of the Carrier Oil .....	175
Table B-3 Results of HYSYS Simulation of the Mixture of NA and Carrier oil with Different TAN at 385 °C .....	176

Figure 2-1 Batch Reactor and Fluidized Sand Bath .....	24
Figure 2-2 Fragmentation Pathways Yielding the Dominant Ions in t-BDMS Derivatives of NA .....	26
Figure 2-3 IR Spectra of an Oil Sample .....	30
Figure 2-4 IR Spectrum of 4% Calcium Naphthenate.....	31
Figure 2-5 Titration Curve of KOH Standardization with Standard KHP Solution .....	34
Figure 2-6 Titration Curve of the Titration Solvent Titrated with KOH.....	35
Figure 2-7 Titration Curve of an Oil Sample Titrated with KOH .....	35
Figure 2-8 3-D Distribution of Carbon Numbers and Z Families of the NA Sample. ....	45
Figure 2-9 IR Spectra of Oil Samples from the Thermal Reaction .....	48
Figure 2-10 IR Spectra of Oil Mixtures before and after the Reaction in Presence of Prepared and Commercial CaO.....	49
Figure 2-11 IR Spectra of Oil Mixtures before and after the Reaction in Presence of Non-dried and Dried CaO at 385 °C for 3 hours .....	50
Figure 2- 12 IR Spectra of Oil Mixtures before and after the Reaction in Presence of CaO and CaCO <sub>3</sub> at 385 °C for 3 hours .....	51
Figure 2-13 Results from TAN Measurement and FTIR Analysis for the Tested Catalysts.....	52
Figure 2-14 SEM Micrograph of the Fresh CaO .....	55
Figure 2-15 SEM Micrographs of the Solids after the Reaction with 20 wt% of CaO Loading.....	56
Figure 2-16 SEM Micrographs of the Solid Sample after the Reaction with 40 wt% of CaO Loading .....	57
Figure 2-17 XRD Profile of CaO before and after the Reaction .....	58
Figure 2-18 XRD Profile of CaO before and after the Reaction .....	60
Figure 2-19 IR Spectra of Solid Samples before and after the Reaction with the Low Initial TAN of 3 .....	61
Figure 2-20 IR Spectra of 4% Calcium Naphthenate and the Solid Sample after the Reaction with the high Initial TAN of 45 .....	62

Figure 2-21 TGA Results Showing Mass Loss of 4% Calcium Naphthenate.....	64
Figure 2-22 TGA Results of Post-Reaction Solid Samples and 4% Calcium Naphthenate .....	65
Figure 2-23 Elemental Composition of the Fresh Mixture of CaO and Kaolin Clay by AES Analysis .....	68
Figure 2-24 Elemental Composition of the Post-reacted Mixture of CaO and Kaolin Clay by ASE Analysis .....	69
Figure 2-25 Reduction of TAN at 365 °C against time for the carrier oil mixtures with initial TAN of 8.5 without and with addition of 20 wt% of CaO. Error bars show 2 times the standard deviation of experiments. ....	71
Figure 2-26 CO <sub>2</sub> Production at 365 °C against time for the carrier oil mixtures with initial TAN of 8.5 without and with addition of 20 wt% of CaO. Error bars show 2 times the standard deviation of experiments. ....	72
Figure 2-27 Reduction of TAN at 365 °C against time for three carrier oil mixtures with different initial TAN in presence of 20 wt% of CaO. Error bars show 2 times the standard deviation of experiments.....	74
Figure 2-28 CO <sub>2</sub> production at 365 °C against time for three carrier oil mixtures with different initial TAN in presence of 20 wt% of CaO. Error bars show 2 times the standard deviation of experiments .....	75
Figure 2-29 Reduction of TAN against time for three carrier oil mixtures with the same initial tan and different CaO loading at three different temperatures. Error bars show standard deviation of experiments.	77
Figure 2-30 CO <sub>2</sub> Production against time for three carrier oil mixtures with the same initial TAN and different CaO loading at three different temperatures. Error bars show standard deviation of experiments.	78
Figure 2-31 Reduction of TAN versus reaction time at different temperatures for three carrier oil mixtures with the same initial TAN in presence of 20 wt% of CaO. Error bars show standard deviation of experiments .....	79
Figure 2- 32 CO <sub>2</sub> production versus reaction time at different temperature for three carrier oil mixtures with the same initial TAN in presence of	

20 wt% of CaO. Error bars show 2 times the standard deviation of experiments.....	80
Figure 2-33 An Arrhenius Plot for the TAN Reduction Reaction.....	82
Figure 2-34 An Arrhenius Plot for the CO <sub>2</sub> Production Reaction.....	83
Figure 2-35 TAN reduction versus time for two oil samples with similar initial TAN in thermal reactions. The regression lines re only for the isothermal period after 5 minutes heating-up. ....	85
Figure 2-36 CO <sub>2</sub> production versus time for two oil samples with similar initial TAN in thermal reactions. The regression lines are only for the isothermal period after 5 minutes heating-up. ....	86
Figure 2-37 TAN reduction versus time for two oil samples with similar initial TAN in the presence of 20 wt% CaO. Error bars show 2 times the standard deviation of experiments .....	87
Figure 2-38 CO <sub>2</sub> production versus time for two oil samples with similar initial TAN in the presence of 20 wt% CaO. Error bars show 2 times the standard deviation of experiments .....	88
Figure 2-39 IR Spectra of Toluene Washing Residue .....	89
Figure 2-40 IR Spectra of Pentane Washing Residue .....	90
Figure 2-41 IR Spectra of CaO after Toluene/Pentane Washing .....	91
Figure 2-42 Reduction of TAN versus reaction time at 385 °C in the Parr reactor for a carrier oil mixture with initial TAN of 40.4 in presence of 30 wt% of CaO (the reactor took one hour to reach 385 °C from the ambient temperature) .....	93
Figure 3-1 Chemical Components of Wood.....	125
Figure 3-2 the Structure Features of Softwood Tracheids (L: Lumen; P: primary wall; S <sub>1</sub> : inner layer; S <sub>2</sub> : middle layer; S <sub>3</sub> : outer layer; M: middle lamella) .....	126
Figure 3- 3 Flow Sheet of the Kraft Pulping Process .....	127
Figure 3-4 Lignin Removal at Different Temperatures with Low Liquor-to-wood Ratio(5:1).....	152

Figure 3-5 Effective Alkali Consumption at Different Temperature with Low Liquor-to-wood Ratio (5:1) vs Time.....	152
Figure 3-6 Hydrosulfide Ion Consumption at Different Temperature with Low Liquor-to-wood Ratio (5:1) vs Time.....	153
Figure 3-7 Lignin Removal Rate at Different Temperatures with High Liquor-to- wood Ratio (50:1). The symbols are Experimental Data of Santos, et al. ....	154
Figure 3-8 Effective Alkali Consumption at Different Temperature with High Liquor-to-wood Ratio (50:1) vs Time.....	154
Figure 3-9 Hydrosulfide Consumption at Different Temperature with High Liquor-to wood Ratio (50:1) vs Time.....	155
Figure 3-10 Lignin Removal Rate at High Liquor-to-wood Ratio (200:1) .....	156
Figure 3-11 Calculated vs Experimental Lignin Content under Low Liquor-to- wood Ratio.....	157
Figure 3-12 Calculated vs Experimental Hydroxide Concentration under Low Liquor-to-wood Ratio	157
Figure 3-13 Calculated vs Experimental Hydrosulfide Concentration under Low Liquor-to-wood Ratio .....	158
Figure 3-14 lnk versus Reciprocal of Temperature .....	161
Figure A-1 Schematic of the Experimental Setup for the Model Compound Reaction System .....	169
Figure A-2 The Optimized Temperature Program for GC .....	170
Figure A-3 Chromatogram of the Mixture of Decane and Heptanone and Butyric Acid .....	171
Figure A-4 Chromatogram of the reaction products.....	172
Figure C-1 Parr Reactor System .....	177
Figure D-1 Calibration Curve for TAN Measurement Relating TAN of Oil Sample and Mass Ratio of NA to Carrier Oil.....	179
Figure E-1 Calibration Curve for Nitrogen Relating Peak Area Registered by GC and Volume of Nitrogen injected .....	180

Figure E-2 Calibration Curve for Nitrogen Relating Peak Area Registered by GC  
and Volume of Nitrogen injected ..... 181

## **SECTION 1 OVERALL INTRODUCTION AND CONTENTS OF THESIS**

Chemical reaction engineering tends to focus mainly on homogeneous reactions or on catalytic reactions wherein the morphology of the solid does not change with extent of reaction. In many cases the analysis of liquid-solid reactions is complicated by change in the solid phase as the reaction proceeds. This thesis examines two cases; one in which the reaction intermediates in the conversion of naphthenic acid (NA) accumulate as a partly soluble intermediate salt that dramatically changes the physical structure of the reacting solid, and the second the Kraft pulping of lignin wherein the delignification reaction progressively alters and dissolves the lignin polymer.

The study on the conversion of NA in oil was summarized in Section 2. Corrosion problems in petroleum refining operations due to NA in crude oils have been recognized since the early 20<sup>th</sup> century (Derungs 1956; Gutzeit 1977; Heler et al. 1963). The presence of relatively high levels of petroleum acids in crude oils tends to cause serious equipment corrosion, especially at high temperature (230-400 °C), and leads to high maintenance costs, and the mechanism of the corrosion is complex and still not well understood. When the bitumen is distilled to recover the gas oil, many of these acidic components are concentrated, and this acidity makes the distilled fraction less attractive to downstream refineries. Therefore, any reduction in naphthenic acid content would alleviate corrosion-associated problems. The term naphthenic acid is a general identifier used to describe all organic acid present in crude oils and petroleum fractions. NA is a complex mixture of acids, and its structure is

primarily represented by alky-substituted cycloalkyl carboxylic acids with the general formula  $R(CH_2)_nCOOH$ , where R is a cyclopentane, cyclohexane or multicyclic ring. The cycloalkyl carboxylic acids may also include single ring and fused multiple ring structures, and the carboxyl group is usually bonded or attached to a side chain rather than directly to the cycloalkyl ring. Because of the inherent structural complexity of NA, the identification of the exact structure of mixtures of NA is impossible. The acid content of crude oil is usually described by total acid number (TAN) which is defined as the amount of potassium hydroxide (in mg) required to neutralize 1 gram of oil sample. TAN number does not correlate directly to corrosion, but in general low acid number (TAN < 2 mg KOH/g oil) is preferred and safe for refinery equipment.

Section 3 summarizes the development of a kinetic model of the Kraft pulping. The kraft pulping, introduced in 1879, still plays a dominant part in pulp industry worldwide today. Therefore, there is a strong economic incentive for better knowledge of the process, especially of the pulping kinetics. The accurate design and control of the pulping process require a reliable model that accounts for both the pulping kinetics and the transport limitations in the wood chips, as well as the flow characteristics in the digester. Further difficulties in the analysis of the pulping processes arise from the complex nature of the wood. From literature review, it is found that although many efforts have been made in modeling the Kraft process, most of the investigators assumed Kraft pulping as a pseudo-homogeneous system, and neglected the heterogeneous nature of the pulping process. This has been due mainly to the complexity of the reactions

involved. In this study, a new mechanism is proposed for the heterogeneous delignification reaction during Kraft pulping process. The mechanism consists of three key kinetic steps: adsorption of hydroxide and hydrosulfide ions on lignin; surface reaction on the solid surface to produce degraded lignin products; desorption of degradation products from the solid surface. The most important step for the delignification process is the surface reaction, rather than reactions occurring in the liquid phase. A kinetic model was developed based on the proposed mechanism.

## **1.1 Research Objectives**

For the study on the conversion of NA, the objective is to study the kinetics of decarboxylation of NA in the liquid phase. Liquid phase processing is desirable for heavy gas oils and crude oils, where complete conversion to vapor phase for reaction would require a too high temperature. Through the experimental study, the effectiveness of alkali metal and alkaline earth metal oxides and carbonates for decarboxylation of NA can also be evaluated. In our study, a commercial mixture of naphthenic acids in a carrier oil was used as a model system. The reagent powders of  $\text{Li}_2\text{O}$ ,  $\text{CaO}$ ,  $\text{CaCO}_3$ ,  $\text{BaO}$  and  $\text{MgO}$  were tested in a batch reactor and their effectiveness in the decarboxylation reaction were determined based on acid conversion. Based on the results, one catalyst was selected for further kinetic study. Two reaction mixtures, carrier oil plus commercial naphthenic acids and heavy vacuum gas oil (HVGO) from

Athabasca bitumen, were applied in the kinetic study. The reaction series were designed to investigate the influence of the TAN of the oil mixture, the temperature, and the catalyst loading on decarboxylation of NA. Moreover, the post-reacted solid samples were analyzed by using various analytical techniques to study the solid intermediate product.

For the kinetic study of Kraft pulping process, the objective is to examine the delignification during the Kraft pulping process from a chemical reaction engineering science perspective. In particular, the chemical reaction mechanism takes into account the heterogeneous nature of Kraft pulping. Lignin reacts in parallel with sodium hydroxide and sodium sulfide. To avoid too many parameters and to reduce the complexity of the kinetic model involved, we treat lignin or lignin segments as one class with the same reactivity. Two delignification reactions take place during cooking: (1) lignin reacts with sodium hydroxide alone, and (2) lignin reacts with the combination of sodium hydroxide and sodium sulfide. In addition, the developed heterogeneous pulping model is based on a lumped parameter approximation, in which the chemical species in wood are lumped, for example, to lignin and carbohydrates, without referring to a specific chemical compound, removing the complexity of the detailed chemistry involved. Moreover, small chips (<2-3 mm) are taken into account in our model in which diffusion is negligible because transport processes within the small chips are not significant. Additional terms would be required in order to model larger chips.

## References

Derungs, W. A. (1956). "Naphthenic acid corrosion- an old enemy of the petroleum industry." *Corrosion-National Association of Corrosion Engineers*, 12, 41-46.

Gutzeit, J. (1977). "Naphthenic acid corrosion in oil refineries." *Materials Performance*(October), 24-35.

Heler, J. J., Merrick, R. D., and Marquand, E. B. (1963). "Corrosion of refinery equipment by naphthenic acid." *Material Protection*(September), 90-96.

## **SECTION 2 CONVERSION OF NAPHTHENIC ACIDS**

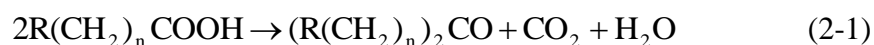
### **2.1 Literature Review**

#### **2.1.1 Approaches for Removal of NA from Oils**

Several approaches to reduce naphthenic acidity in petroleum oils have been developed. The most straightforward solution is to blend the feed with high NA content with the low acid ones, but the acidic compounds remain in the blend and the value of the low acidic feed is reduced, although NA content of the feed is diluted to an acceptable level. Another approach is addition of corrosion inhibitor(Edmondson 1987; Petersen et al. 1993), but the resulting stable emulsions are difficult to separate from the treated crude. Acidity reduction can also be realized by washing oil with basic solutions of NaOH and KOH(Verachtert 1980). Caustic treatment can substantially remove NA, but the process generates significant amounts of waste water and emulsions that are difficult and expensive to separate. This method also incorporates salts into the crude oil that can cause fouling downstream. Varadaj used an adsorbent to adsorb NA from the oil feed. Disclosed adsorbents include carbon black, spent or coked FCC catalysts, and selected clays(Chamberlain 2004; Silva 2007; Varadaraj 2002; Zhang et al. 2005). Water was also applied in the treated feed in Varadaj's approach. According to US patents(Bearden et al. 1999; Bienstock et al. 2000; Blum et al. 1998)naphthenic acids can be removed from the petroleum fraction by a moderate thermal treatment in which the oil feed was heated without addition of catalyst between 315 and 400 °C to convert NAs into neutral

compounds. However, hydrocarbon was also cracked significantly when exposed to such high temperature. Siskin et al.(Siskin et al. 2001) invented a process for removal of NA from petroleum oil feed in which alcohol and a base were added to convert naphthenic acids into an ester. The base was selected from Group IA and IIA metal carbonates, hydroxides, phosphates, and a mixture of a hydroxide and phosphate. Some other processes(Ferguson and Reese 1986; Sartori et al. 2001; Varadaraj et al. 1999) were invented to convert naphthenic acids in oil into a neutral compound in which amine homologues, such as monoethanolamine, ethoxylated amine, and polymeric amines are introduced to form a water-in-oil emulsion of amine salt. Although a number of methods have been suggested for high acid content petroleum, each method has its processing problems for commercialization. For example, addition of corrosion inhibitors, amine homologues, or washing oil with basic solutions would reduce the acid content in the crude, but the resulting stable emulsions are difficult to separate. For adsorption method, a large amount of water is required. Consequently, significant processing challenges remain in the upgrading of NA containing petroleum fractions and whole crude oils.

Catalytic decarboxylation of carboxylic acid is a well-established chemical reaction. With catalysts active for decarboxylation reactions, NA can be catalytically converted into neutral ketones and carbon dioxide at moderate temperatures. The basic reaction for the catalytic decomposition of naphthenic acids is illustrated by Equation (2-1).



This catalytic conversion is actively catalyzed By Group I and Group II oxides, carbonates at temperature of 300-450 °C. Of these, carbonates and oxides of alkaline earth metals (Ca, Mg, and Ba) and rare earth oxides (Fe, Mn, Cr, and Zn) are active to varying extents.

### **2.1.2 Catalysts Active for Decarboxylation of NA**

The literature abounds with reports on the decarboxylation of carboxylic acids on metal oxide. Alkyl carboxylic acids, especially acetic acid and propionic acid, have been the subject of the research. A great number of metal and metal oxides are found to be active for decarboxylation of carboxylic acids: Cu(Bowker and Madix 1981), Fe(Kishi and Ikeda 1980), Cr<sub>2</sub>O<sub>3</sub>(Swaminathan and Kuriacose 1970),  $\alpha$ -Fe<sub>2</sub>O<sub>3</sub>(Pestman et al. 1995; Pestman et al. 1997b), CeO<sub>2</sub>, MnO<sub>2</sub>(Glinski and Kaszubski 2000; Glinski and Kijenski 2000; Glinski et al. 1995) , ZrO<sub>2</sub>(Parida and Mishra 1999; Pestman et al. 1997b), MgO(Parrott et al. 1978; Spitz et al. 1986; Zhang et al. 2006), CaO(Zhang et al. 2006) and TiO<sub>2</sub>(Groff and Manogue 1983; Pestman et al. 1995). Most of these studies targeted much more concentrated acids from other sources, not naphthenic acids in crude oil at all. NA should be chemically similar to the fatty acids, but their concentration in crude oil and HVGO is quite low. Few studies reported on real naphthenic acids in crude oil feed. Moser et al. (Moser 1940)invented a process in which the vapor of mineral oil containing NA was passed through the catalyst over the temperature range of 250 to 300 °C. NA was eliminated quickly and converted into CO<sub>2</sub> and ketone/hydrocarbons, steam was desired to applied to avoid

cracking of the hydrocarbons. The catalysts tested in their study were the basic carbonates, lithium oxide, and the alkaline earth metals oxides. The oxides and corresponding salts of the rare earths, especially thorium oxide, iron, manganese, chromium, uranium, cadmium, and zinc, were also effective to some extent. Of these, the carbonates of lithium and the alkaline earth metal, and particularly the group of metals having molecular weights below sodium, such as lithium, magnesium, and calcium, were particularly effective. Curtis et al. (Curtis et al. 1974) studied decarboxylation of stearic and palmitic acids on various metallic oxide and carbonate catalysts. Magnesium oxide was selected as the most active catalyst for the preparation of ketone, and the most suitable temperature range is 330-360 °C. Leung et al. (Leung et al. 1995) reported the pyrolysis of pure saturated carboxylic acids ranging from C<sub>4</sub> to C<sub>12</sub> at a WHSV of 0.46 h<sup>-1</sup> over alumina at 450 °C and atmospheric pressure. The lower molar mass carboxylic acids had higher yield of symmetrical ketones than the higher molar mass carboxylic acids. Further pyrolysis of ketone-containing product yielded hydrocarbons. The pyrolysis of dodecanoic acid and diundecyl ketone gave a similar composition of the pyrolytic products, which indicated that all the carboxylic acid degraded to hydrocarbons via the symmetrical ketone. Monoenes were the major hydrocarbon products from ketones. Ding et al. (Ding et al. 2008) studied NA removal by catalytic decarboxylation on alkaline earth oxide catalysts, with bitumen-derived HVGO as an oil feed. CaO exhibited a much higher activity for NA removal among the tested catalysts at 350 °C. XRD profile of the spent CaO from a continuous reactor indicated the formation of

Ca(OH)<sub>2</sub>, no peak associated with CaCO<sub>3</sub> was found, which was different from the XRD profile of the spent CaO from an autoclave reactor, showing the peaks responding to Ca(OH)<sub>2</sub> and CaCO<sub>3</sub>. The author attributed this difference to the shorter contact time between CaO and CO<sub>2</sub> in the flow reactor comparing with that in the autoclave reactor. No other intermediates or by products were observed. In this work, the spent catalysts were analyzed by using XRD, SEM, EDX/SEM, and AES to trace the formations of intermediates. Zhang et al. (Zhang et al. 2004) studied catalytic NA conversion in crude oil in the presence of MgO, CaO, Ag<sub>2</sub>O, and CuO, CaO shows a high acid conversion of about 70%, and 30% for MgO. Ag<sub>2</sub>O and CuO had no positive influence in the NA conversion. In their later work (Zhang et al. 2006), MgO was selected as a catalyst to study its activity and deactivation on NA conversion in crude oil using a flow reaction apparatus, the results showed that the higher temperature applied, the longer the catalytic capacity lasted. However, no detailed information about the kinetics was reported. Therefore, in our work, we conducted the experimental study to explore the kinetics of NA conversion by decarboxylation, and to reveal the reaction pathway of NA conversion in oil.

### **2.1.3 Thermal Decomposition of Carboxylic salts**

Guarino(Guarino 2006) proposed that the formation of butyrate due to the interaction between butyric acid and carbonate/oxide was an intermediate step in the decarboxylation reaction to produce ketone. The reaction between butyric acid and the oxide/carbonate forming butyrate was followed by thermal

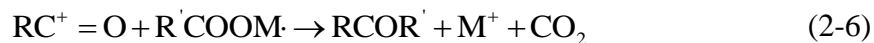
decomposition of butyrate, in which CO<sub>2</sub>, H<sub>2</sub>O, C<sub>7</sub>H<sub>14</sub>O, intermediates were formed, and then C<sub>7</sub>H<sub>14</sub>O was reacted with intermediates to form alkenes and other ketones. A number of studies on the thermal decomposition of carboxylic salts to produce ketone have been conducted by the researchers. Thermal decomposition of salts of carboxylic acids yields symmetrical ketones, and the mixtures of salts of two different acids pyrolyze to produce unsymmetrical ketone (Hites and Biemann 1972).

To study the mechanism of the decomposition of the carboxylic salts, several authors investigated the pyrolysis of salt mixtures by labeling one salt with <sup>13</sup>C or <sup>14</sup>C in the carbonyl group to observe the source of the carbonyl group in the resulting unsymmetrical ketone. Some reaction mechanisms were developed based on their observations. Bell (Bell and Reed 1952) reported that <sup>13</sup>C content of the carbonyl carbon atom of the acetaldehyde obtained in the pyrolysis of a mixture of barium acetate with <sup>13</sup>C in the carboxyl group and barium formate. The fission of the carbon-carbon bond in the acetate took place in the reaction. A free radical mechanism was proposed to interpret the results.



Lee (Lee and Spinks 1953) developed a two-step mechanism in which an acyl carbonium ion was produced by a fairly fast reversible reaction followed by a rate-controlling displacement reaction





Miller proposed a mechanism involving carbanions (Miller et al. 1950):



Although a number of data on the thermal behavior of carboxylate salts were reported, data on thermal stabilities of naphthenates so far were only occasionally reported in the literature. Al-sammerrai (Al-Sammerrai and Abdul-Razaak 1984) investigated the thermal decomposition of sodium and potassium cyclohexane butyrates, and found that the sodium and potassium cyclohexane butyrates possessed a wider stability range of their melts than the sodium alkanoate, and noted as well that the stability increased on replacing the sodium with the potassium cation, the decomposition temperature under nitrogen started at 703 K for sodium cyclohexane butyrate and 723 K for potassium cyclohexane butyrate.

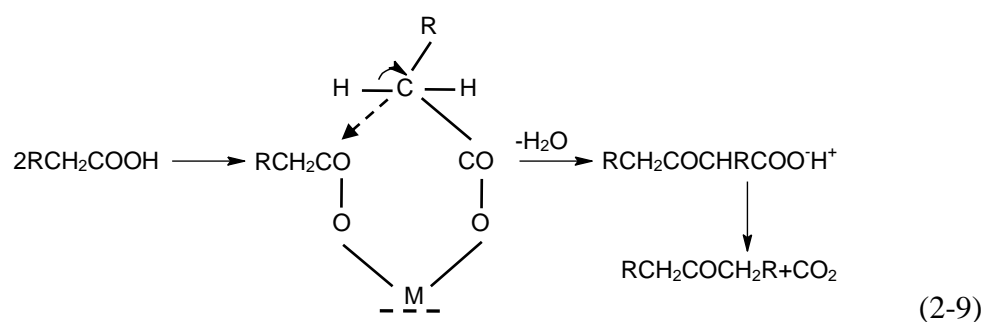
#### 2.1.4 Reaction Mechanism of Ketonic Decarboxylation of NA

Although many studies have explored the mechanism of the decarboxylation reaction, and several different reaction mechanisms have been proposed, the mechanism of this reaction remains under debate.

The first mechanistic proposal was probably that of Bamberger (Bamberger 1910) who proposed acetic anhydride as reaction intermediate during bimolecular ketonization of acetic acid. According to the work by

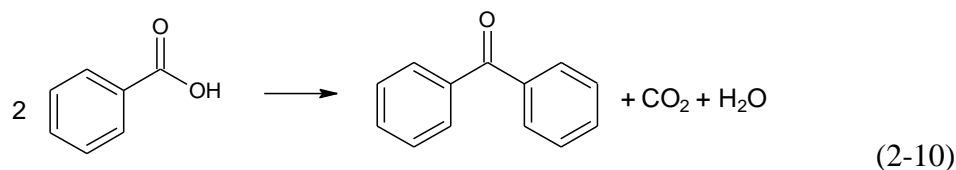
Lorenzelli et al. (Lorenzelli et al. 1980), acetic anhydride was very unstable in the presence of surface hydroxyl groups and formed adsorbed acetates on the surface of  $\alpha\text{-Fe}_2\text{O}_3$  at room temperature. Therefore, anhydride was not likely to be an intermediate in the ketonization reaction.

Neunhoeffer and Paschke proposed a  $\beta$ -keto acid intermediate, which was found in the decarboxylation reaction of carboxylic acids possessing an  $\alpha$ -hydrogen atom (Pestman et al. 1997a). The keto-acid mechanism involves a cyclic six-membered transition state which could have any degree of ionic character.

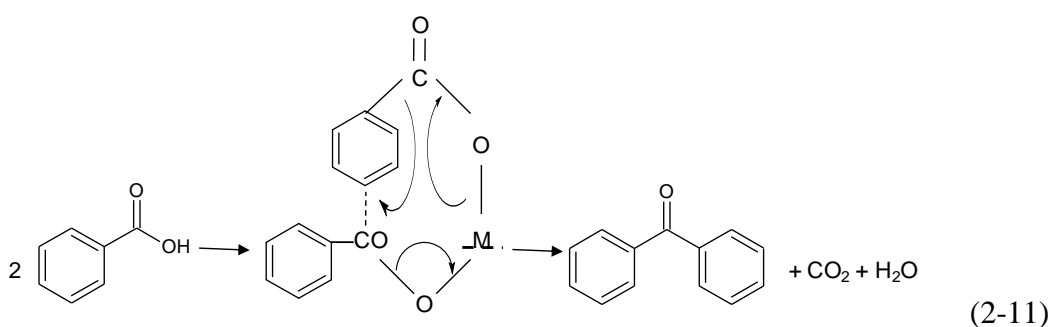


Isotopic tracer studies of pyrolysis of dicarboxylic acid salts support this mechanism (Kwart and King 1969; Lee and Spinks 1953). When mixtures of acetate labeled with  $\text{C}^{14}$  in the carboxyl group and unlabeled formate, benzoate, or p-toluate were pyrolyzed, all the labeled carbon was found in  $\text{CO}_2$ .

For those carboxylic acids that do not possess an  $\alpha$ -hydrogen atom, this mechanism is inadequate. For example, the formation of benzophenone from benzoic acid gives:



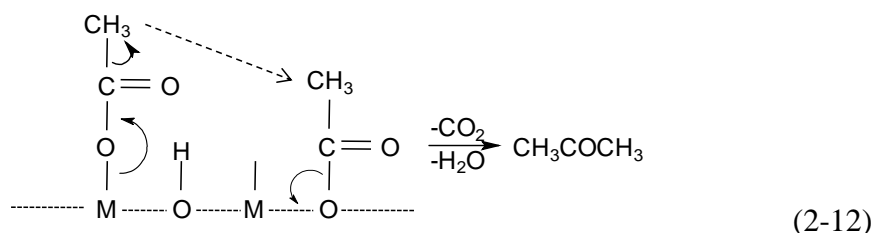
To explain the ketonization of carboxylic acids that lack an  $\alpha$ -hydrogen atom, Kwart and Kim (Kim and Barteau 1990) proposed a concerted mechanism for ketonization of aromatic acids. According to the concerted mechanism, the pathway of formation of benzophenone from benzoic acid is as follows:



Aromatic acids cannot form keto acids, but their ketonization can be interpreted by the concerted mechanism in which the ionic character arises by loss of carbon dioxide rather than by loss of  $\alpha$ -hydrogen. In the concerted mechanism, the carboxylic acid was deprotonated by a base to give the carboxylate, which was simultaneously attacked by the second carboxylic acid group to form the acid intermediate. The mechanism was in accordance with a number of experimental observations. Kim and Barteau reported (Kim and Barteau 1990) results of TPD studies of carboxylic acid decomposition on  $\text{TiO}_2$ . Carboxylic acid adsorptions at room temperature were studied in their work. Two adsorbed phases were observed: molecular carboxylic acid and carboxylate. With elevated temperature in the TPD study, it was found that the molecular carboxylic acid desorbed reversibly intact at 350 K firstly, the surface

carboxylates desorbed in two stages: about 40% of the surface carboxylate recombined with the surface hydroxyl group to form the parent carboxylic acid at 400 K, and at higher temperature (>525K) the leftover of the surface carboxylates gave a bimolecular ketonization to the corresponding ketones and CO<sub>2</sub> as well as a unimolecular dehydration reaction to form CO, ketene, and acrolein from formate, acetate and propionate, respectively. This observation was confirmed by Imanaka et al that the adsorbed acetate and molecular acetic acid were found on the surface when they studied the adsorbed states of acetic acid on metal oxide catalysts such as ZnO, MnO, CaO and MgO (Rajadurai 1994).

Swaminathan and Kuriacose (Kuriacose and Jewur 1977; Swaminathan and Kuriacose 1970) proposed that ketonization of acetic acid and propionic acid on Cr<sub>2</sub>O<sub>3</sub> proceeded via interaction between a acetate ion and an acyl group formed on the surface. The acetate ion was formed by the adsorption of acetic acid following the dehydrogenation mechanism suggested by Volkenstein (Volkenstein 1960), which is similar to the adsorption of an alcohol as RO<sup>-</sup> and H<sup>+</sup>. The acylcarbonium ion was formed by the adsorption of acetic acid following dehydration, which is similar to the adsorption of an alcohol as R<sup>+</sup> and OH.



Parida et al. (Parida and Mishra 1999) suggested that ketonization of acetic acid on the oxide of zirconia followed surface interaction without



suppressed by diminishing the number of  $\alpha$ -hydrogen atoms. They also proposed ketene or a ketene-like specie as an intermediate.

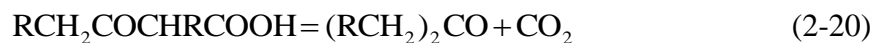
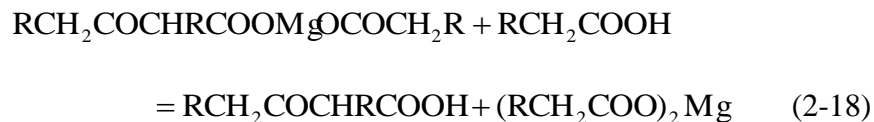
The gas-phase catalytic decarboxylation of models of NA was studied by Guarino(Guarino 2006), who found that formation of butyrate is an intermediate step in the carboxylation reaction to produce ketone.

### 2.1.5 Kinetics of decarboxylation of NA

Although many papers have reported the decarboxylation of carboxylic acids, little work on the rate of ketonic decarboxylation has been published.

Curtis et al. (Curtis et al. 1974) studied the rate at which stearic acid was pyrolyzed to stearone in the presence of magnesium oxide. The most suitable reaction temperature range was 330-360 °C. During the reaction CO<sub>2</sub> was evolved in an amount equal to 94% of that required for complete ketonization. Small amounts of CO and other gases were also formed. The progress of the reaction was followed by measurement of the rate of liberation of CO<sub>2</sub>, and the results were shown to agree with the assumption that a keto-acid was considered as an intermediate in the formation of ketones. The mechanism of the decarboxylation was proposed as:





Interruption of the reaction and estimation of the unchanged acid present, together with knowledge of the amount of CO<sub>2</sub> liberated, allows calculation of the amount of keto-acid present in the reaction mixture, which was found to be constant during the early stages of the reaction, but increased greatly when the reaction became violent. They suggested that formation of the salt of the keto-acid was the rate-determining reaction and that this reaction was catalyzed by the metal oxide used.

More recent studies of carboxylic acids were conducted by Muller-Erlwein (Leung et al. 1995). He compared the effect of reaction time, temperature in the range 269-340 °C, and catalyst composition on the pyrolytic conversions of dodecanoic acid and stearic acid to diundecyl ketone and 18-pentatriacontanone, respectively. For dodecanoic acid, the reaction temperature had a great influence on conversion, while catalyst percentage (5-18% MnO<sub>2</sub>) had only a minor effect. For stearic acid, the catalyst percentage and the reaction temperature both had a strong influence on conversion. For example, at 308 °C, 50% conversion to ketone was achieved in approximately 75 min when 10% MnO<sub>2</sub> catalyst was used, compared to 50 % conversion at approximately 600 min for 5% MnO<sub>2</sub>. The rate of decarboxylation is second order in acid concentration.



$$r = -2\rho_{\text{kat}} kC^2 \quad (2-22)$$

Leicester and Redman (Leicester and Redman 1962) reported that rates of ketonic decarboxylation of nickel and cobalt salts of aliphatic acids were zero order at 280 °C. Galwey determined that decomposition of nickel benzoate obeyed zero-order kinetics. Gerchakov and Schultz (Gerchakov and Schultz 1967) reported that the pyrolysis of lead (II) octanoate proceeded in two sharply differentiated phases. The first phase happened at a pyrolysis temperature in the range of 290-310 °C, and followed zero-order kinetics. The second phase did not commence until the residue from the first decarboxylation phase had been raised to a temperature of at least 360 °C. The order of the second phase failed to be obtained because of erratic and nonreproducible experimental data. The experiments of Palmer et al. (Palmer and Drummond 1986) with acetic acid also indicated that the decarboxylation reaction over silica follows zero order.

However, Bell et al. (Bell 1994) studied the kinetics of decarboxylation of aqueous solutions of acetic acid and sodium acetate over various mineral surfaces, such as quartz, calcite, montmorillonite, pyrite, hematite, and magnetite. Most experimental data demonstrated first order kinetics on the tested mineral surface except quartz.

Through the literature review on decarboxylation of carboxylic acids, we found that most of the previous studies focused on the reactions in a vapor phase or concentrated suspension of fatty acids to achieve complete decarboxylation.

There are not many data reported on the decarboxylation reaction of NA in a dilute liquid hydrocarbon medium. In this study, the experimental study on the kinetics of decarboxylation of NA in a dilute liquid oil medium is reported.

## **2.2 Experimental Materials and Methods**

### **2.2.1 Materials**

Initial experiments considered butyric acid as a model compound of naphthenic acids, with decane as the solvent. These components were too low boiling for liquid-phase reaction at temperatures over 350 °C (See Appendix A for reactions on the mixture of butyric acid and decane). Therefore, a commercial mixture of naphthenic acids (NA-2) was applied, and a highly hydrotreated carrier oil base stock was selected as a carrier.

#### **2.2.1.1 Naphthenic Acid-2 (NA)**

NA was purchased from OMG Americas Inc. Table 2-1 lists its physical properties as provided by the company.

Table 2-1 Physical Properties of NA

Characteristics	Limits	Methods	Typicals
Color	Brown	Visual	Brown
Viscosity, Gardner	A-1	ASTM D 1545	D
Specific Gravity	0.92-0.99	ASTM D 1963	0.97
Weight/Gallon, Lbs	7.7-8.2	ASTM D 1963	8.1
Acid value	200-215	ASTM D 1980	205

### 2.2.1.2 Carrier Oil

Paraflex HT oil was purchased from Petro-Canada. It is a 99.9% pure saturated hydrocarbon mixture that is crystal clear, thus called white oil. In our work, white oil was used as the solvent owing to its high thermal stability. Table 2-2 lists the physical properties of white oil.

Table 2-2 Physical Properties of Carrier Oil

Density, kg/l@15 °C		0.868
Color, ASTM		<0.5
viscosity	cSt@40 °C	103.0
	cSt@100 °C	11.3
	SUV@100 °F	504
	SUV@210 °F	65
Viscosity index		103
Flash point, °C		255
Saturates, wt%		99.9
Aromatics, wt%		0.1

### 2.2.1.3 HVGO

The kinetic reactions were performed on the HVGO to compare with the model compound described in the previous work. The HVGO was supplied by Suncor Energy Inc, and its properties are listed in Table 2-3.

Table 2-3 Properties of HVGO Used in the Experimental Study

Boiling point, °C	Vapor pressure, kPa	Density, g/cm <sup>3</sup>	Specific gravity	Hydrogen sulphide, ppm	Water solubility
215 - 620	1.0-2	0.95-0.98	0.96-0.98	<3	insoluble

### 2.2.1.4 Catalyst Preparation

It has been reported that the catalysts of CaO and CaCO<sub>3</sub> exhibit high activity in the vapor-phase decarboxylation of NA (Guarino 2006). Moreover, Zhang, et al. (Zhang et al. 2004; Zhang et al. 2006) found that MgO and CaO have high reactivity toward NA conversion. Therefore, the catalysts of alkali metal and alkaline earth metal oxides and carbonates were investigated in this work. Some catalysts were prepared in the lab. Calcium carbonate was prepared by precipitation. Soluble salts of sodium and calcium were used as the precursors of the carbonate (Table 2-4).

The procedure employed in the preparation of the carbonate is described as follows:

1. Certain amount of the precursor (Ca(NO<sub>3</sub>)<sub>2</sub> 4H<sub>2</sub>O) was added to de-ionized water and dissolved.

2. The precipitating agent of sodium carbonate was added to the solution of the precursor.
3. The mixture was heated until boiling with continuous stirring.
4. Upon the formation of the precipitate, the mixture was filtered and washed with hot water to collect the solid.
5. The precipitate was dried at 110 °C for overnight.

For the preparation of calcium oxide, the carbonate sample was calcined at 900 °C for 24 hours.

The Li<sub>2</sub>O/TiO<sub>2</sub> catalyst was prepared by impregnation of TiO<sub>2</sub> support with the dropwise addition of LiNO<sub>3</sub>. After impregnation, the sample was dried at 110 °C for 16 hours and then calcined at 500 °C for 1 hour.

The commercial products of CaO (A.C.S. reagent, 99%, Sigma), CaCO<sub>3</sub> (reagent grade, 98%, Sigma), Li<sub>2</sub>O (97%, Sigma), MgO (99+%, Sigma) and BaO (99.99%, Sigma) were purchased for comparison.

Table 2-4 Catalyst Preparation

Catalysts	Preparation
CaCO <sub>3</sub>	Precipitation of salts from the reaction of NaCO <sub>3</sub> and Ca(NO <sub>3</sub> ) <sub>2</sub> 4H <sub>2</sub> O
CaO	Thermal decomposition of CaCO <sub>3</sub> at 900 °C
Li <sub>2</sub> O/TiO <sub>2</sub>	Impregnation of TiO <sub>2</sub> support with LiNO <sub>3</sub> using the incipient-wetness method

### 2.2.2 Experimental Equipment

For catalysts screening, a micro-tubular reactor was used for the study. A diagram of the reactor system is shown in Figure 2-1. A batch microreactor with a capacity of 30 ml consisted of a 3/4 '' stainless steel tube with Swagelok stainless steel fittings on each end.

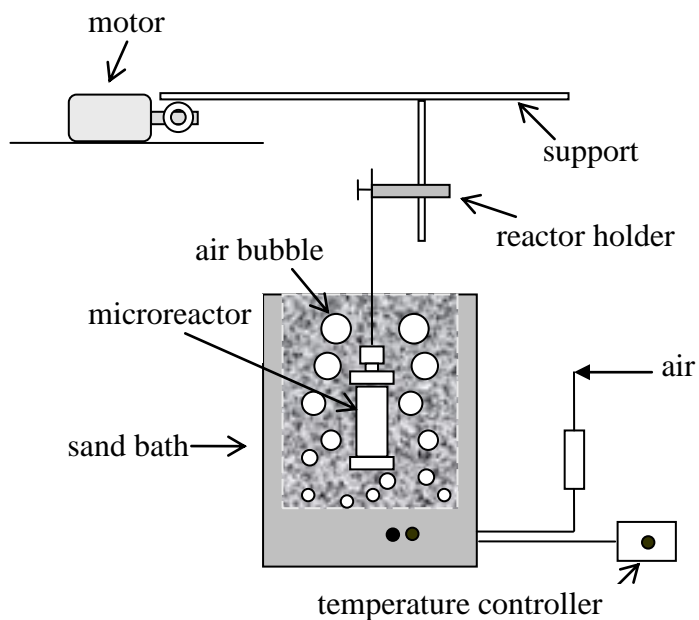


Figure 2-1 Batch Reactor and Fluidized Sand Bath

### 2.2.3 Reaction Procedure

For all of the screening reactions, the mixture of carrier oil and NA with TAN of 3 (mass ratio of NA to oil is 0.0148) was charged to a microreactor, and nitrogen as an inert gas was applied to purge air. Based on the calculation using HYSYS (HYSYS 2004.2), the saturated pressure of the mixture of NA and carrier oil with TAN of 3 at 385 °C is 36.67 kPa (See Appendix B for the simulation of vapor-liquid equilibria of the mixture using HYSYS). Therefore,

when the pressure of the reactor is kept at over 36.67 kPa, the mixture maintains in the liquid phase at 385 °C. In this study, the reactor was pressurized with nitrogen at 400 kPa. Then the reactor was placed in a fluidized sand bath whose temperature was controlled to remain at a reaction temperature. The reactor was agitated within the sand bath so that a good contact between the reactants and the catalyst can be achieved. After a given reaction time, the reactor was taken out of the sand bath and rapidly quenched in a cool water bath. After about 15 minutes, the reaction residues were separated by a centrifuge rotating at 3000 rpm for 30 minutes. The liquid phase was collected and analyzed by Fourier transform infrared spectroscopy (FTIR), and the TAN of the liquid sample was also measured by following ASTM D664. The solid phase was washed with toluene, filtered with a membrane filter, and dried in an oven at 105 °C overnight, then analyzed using FTIR and thermal gravimetric analysis (TGA).

For the kinetic study, three mixtures with TAN of 5.1, 8.5, and 10.8 were prepared for the study. The experiments were carried out at 365, 375, and 385 °C, respectively. For most runs, 20 wt% of CaO on a basis of NA weight was loaded. The tightened reactor was pressurized with N<sub>2</sub> at 400 kPa. Each series of reactions with the same initial TAN underwent for 0, 15, 30, 45, 60, and 90 minutes, respectively. A series of thermal reactions with the initial TAN of 8.48 was performed for comparison. The reaction follows the same procedures as those in catalyst screening. After the reaction, the gas sample was collected with a syringe directly and analyzed by GC(GC, Varian 3400X with the star chromatography workstation). After that, the reactor was unloaded. The

supernatant liquid was taken out of the reactor and titrated to measure TAN immediately by an automatic titration system (Titrand 808 by Metrohm).

## **2.3 Methods of Analysis**

### **2.3.1 Characterization of Naphthenic Acid by Gas Chromatography-Electron Impact Mass Spectrometry (GC-MS)**

NA is a complex mixture of alkyl-substituted acyclic and cycloaliphatic carboxylic acids, with the general chemical formula  $C_nH_{2n-Z}O_2$ , where  $n$  represents the carbon numbers and  $Z$  specifies a homologous family (the value of  $Z$  is two times the number of rings in the molecule). Because the NA mixture is comprised of a number of chemically and physically similar compounds, they are very difficult to be identified individually. Work has been conducted for characterization of NA in crude oil, with techniques such as Fourier Transform Infrared Spectroscopy (FTIR) (Holowenko et al. 2001), Fluoride Ion Chemical Ionization Mass Spectrometry (Dzidic et al. 1988), GC-MS (Holowenko et al. 2002; St. John et al. 1998), and Two-dimensional Gas Chromatography (Beens et al. 1998). Considering the accessibility of the equipment and the complexity of spectra reading, we chose GC-EIMS method to characterize NA.

St. John et. al. (St. John et al. 1998) developed a method to analyze and characterize tert-butyldimethylsilyl derivatives of NA by GC-EIMS. The fragmentation pathways leading to dominant ions in t-BDMS derivatives of NA are shown in Figure 2-2. The derivatives of NA generate a little fragmentation, and lose  $C(CH_3)_3$  to produce the prominent base peak  $[M+57]^+$ , corresponding to

the [naphthenate + dimethylsilyl]<sup>+</sup> ion, whose m/z is 57 mass units greater than that of the underivatized NA, because the Si(CH<sub>3</sub>)<sub>2</sub> is bonded to the parent compound. For NA derivatives, it is assumed that the base peak ions (above m/z~200) represent the large ions for each individual compound. Therefore, by subtraction of 57 (Si(CH<sub>3</sub>)<sub>2</sub>) from [M+57]<sup>+</sup> base peak, the exact molecular mass of each compound can be obtained. From the obtained molecular mass, a reasonable formula can be given based on the general form C<sub>n</sub>H<sub>2n-z</sub>O<sub>2</sub> for monocarboxylic acids.

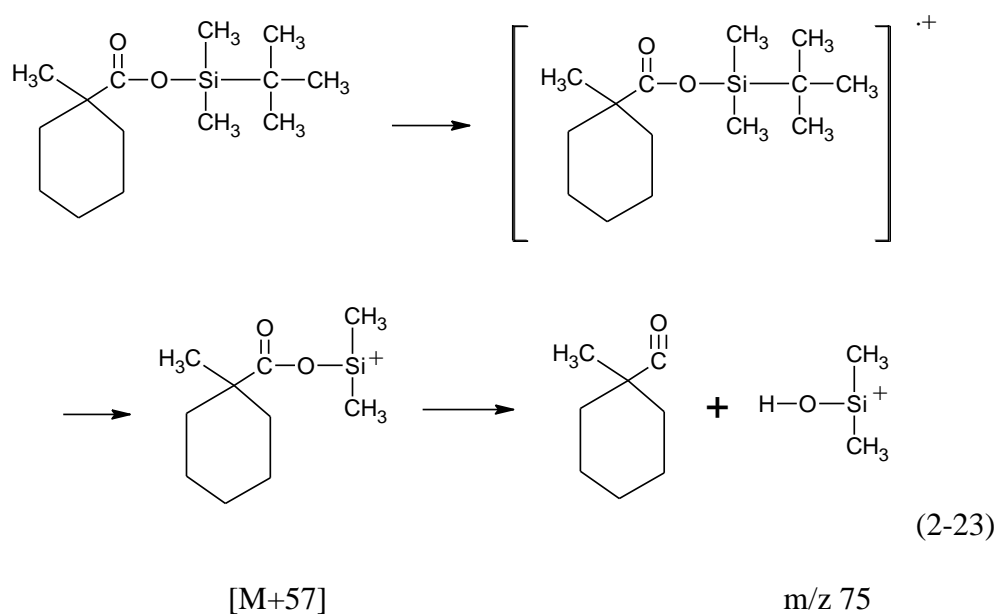


Figure 2-2 Fragmentation Pathways Yielding the Dominant Ions in t-BDMS Derivatives of NA

### **2.3.1.1 Derivatization Procedure**

NA was derivatized by reacting with a derivatizing agent. The procedure is given by Holowenko (Holowenko et al. 2002). A sample of NA was dissolved in dichloromethane to concentration of 20 mg/mL. 100  $\mu$ L of this solution was transferred to a 1.8-mL glass vial and mixed with 100  $\mu$ L of N-methyl-N-(tert-butyl dimethylsilyl) trifluoroacetamide (MTBSTFA, >95% from Sigma) containing 1% tert-butyl dimethylsilyl chloride. The glass vial was sealed with a Teflon lined cap and the sample was heated at 60  $^{\circ}$ C for 20 min.

### **2.3.1.2 GC-MS Analysis**

The derivatized NA samples were analyzed in Mass Spectrometry Laboratory in the Department of Chemistry at the University of Alberta. The GC-MS was operated under the conditions described by Holowenko (Holowenko et al. 2002). After GC-MS scan was completed, the peak intensity values of the desired ions were averaged and processed in a Microsoft Excel spreadsheet (provided by Dr. Phillip M. Fedorak, Department of Biological Sciences at the University of Alberta). The abundances of NA components with a given carbon number in a given Z family are displayed in a normalized matrix, and a 3-D distribution graph is also given.

### 2.3.2 Infrared Spectroscopy (IR)

In infrared spectroscopy, IR radiation is passed through a sample. Some of the infrared radiation is absorbed by the sample and some of it is passed through (transmitted). The resulting spectrum contains absorption peaks which correspond to the frequencies of vibrations between the bonds of the atoms making up the material. Because each different material is a unique combination of atoms, no two compounds produce the same infrared spectrum. Therefore, infrared spectroscopy can result in a positive identification of every different kind of material. In addition, the size of the peaks in the spectrum is a direct indication of the amount of materials present.

After the reaction, the liquid and solid samples was collected and analyzed by FTIR spectroscopy, (Nicolet 8700 FT with OMNIC software by Thermo Electron Corporation). When liquid samples were tested, liquid samples were dripped into the liquid trough directly. IR spectra of solid samples were measured using the KBr wafer technique, the little amount of solid samples were ground with KBr, and then put into the solid trough. All the spectra were recorded in the range of 400-4000  $\text{cm}^{-1}$ .

In the solid or liquid phases, the C=O group of aliphatic carboxylic acids absorbs very strongly in the region of 1725-1700  $\text{cm}^{-1}$  (Randall et al. 1949). The IR spectra of oil samples in the study show that the IR adsorption band of C=O in RC=OOH is around 1710  $\text{cm}^{-1}$ , which was monitored to represent the change of NA in white oil (Figure 2-3). The magnified peak associated with carbonyl group was also plotted and stacked above the spectra of the sample. The peaks at

around 2900, 1700, 1450, and 720  $\text{cm}^{-1}$  correspond to  $\text{CH}_3/\text{CH}_2$  stretching,  $\text{C}=\text{O}$  stretching,  $\text{CH}_3/\text{CH}_2$  bending and  $\text{CH}_2$  rocking, respectively (Szymanski and Alpert 1964).

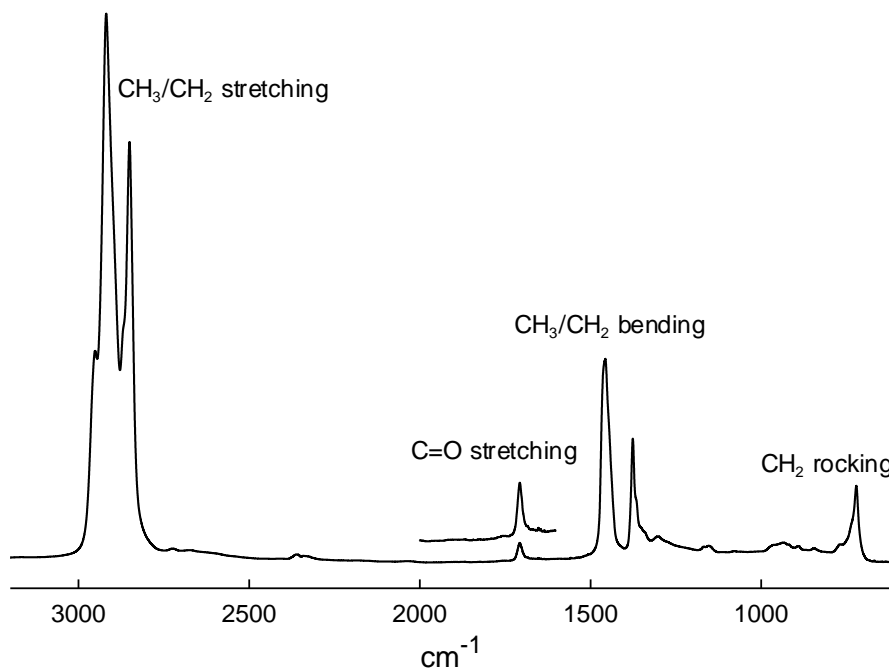


Figure 2-3 IR Spectra of an Oil Sample

In this work, we hypothesises that the formation of a naphthenate salt is an intermediate step in the decarboxylation reaction. If it is true, the naphthenate salt would be found in the solid samples. So in analysis of solid samples, we focus on the detection of the naphthenate salt. The solid catalysts before and after the reaction were analyzed by FTIR to identify the formation of the naphthenate salt. In FTIR analysis, a solid sample was milled with KBr to form a very fine powder for analysis. The reason for the use of KBr is that KBr is transparent in the IR.

As described (Randall et al. 1949), carboxylic acid salts have a very strong, characteristic band in the region of 1610-1550  $\text{cm}^{-1}$  due to the asymmetric

stretching vibration of C=O. The symmetric stretching vibration of this group gives rise to a band in the range of 1420-1335  $\text{cm}^{-1}$  that is broad, and generally has two or three peaks, which is different from C=O in naphthenic acids (around 1700  $\text{cm}^{-1}$ ). In this work, 4% of the commercial calcium naphthenate was employed as a model compound to monitor infrared characteristic group frequencies of C=O of a naphthenate salt (Figure 2-4). The composition of calcium naphthenate is listed in Table 2-5.

Table 2-5 Composition of 4% Calcium Naphthenate

Component		percent
Mineral spirits		45-55
Mixed calcium carboxylates mixture	calcium neodecanoate	40-50
	calcium naphthenate	
Dipropylene glycol monomethyl ether		1-5
Hexylene glycol		1-5

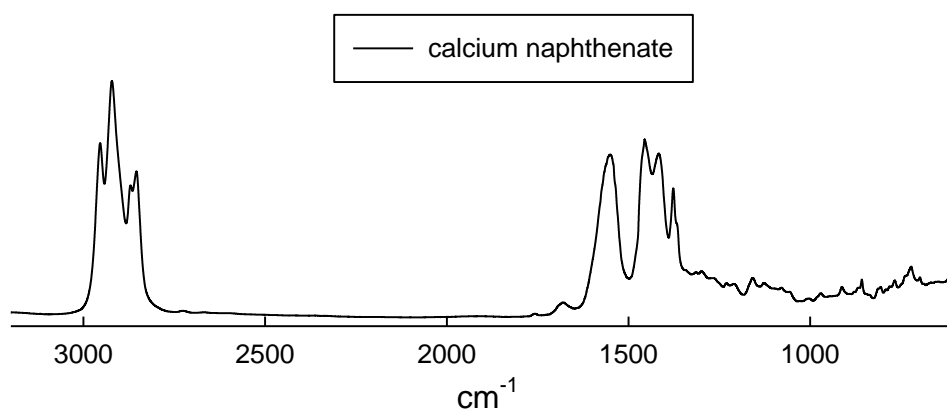


Figure 2-4 IR Spectrum of 4% Calcium Naphthenate

### 2.3.3 TAN Measurement

The TAN of a mixture of NA and carrier oil was measured by following the procedure of ASTM D664 (D664-04 2004). The principle of the method is based on nonaqueous acid-base potentiometric titration determined by a PH/mV meter (Accumet basic AB 15 from Fisher). The major test steps are as follows:

1. Preparation of electrode: replace the electrolyte in the glass electrode with 1-3 M LiCl in ethanol.
2. Preparation of alcoholic potassium hydroxide solution: add 6 g of KOH (GR ACS pellet by EMD) to approximately 1 L of anhydrous iso-propanol (Fisher). Boiling gently for 10 min to increase its solubility. Stand the solution for two days and then filter the supernatant with a fine sintered-glass funnel (made by the glassware workshop in the Chemistry Department, University of Alberta) before standardization with potassium hydrogen phthalate (0.05N, Fisher).
3. Standardization of alcoholic KOH solution: 10ml of 0.05 N standard KHP solution (Fisher) was transferred to a 250 ml beaker, and the prepared alcoholic KOH solution was added slowly until the end point was approached.
4. Preparation of oil sample: dissolve the suitable amount of oil sample in 125 mL titration solvent (495 ml iso-propanol + 5 ml water/ 500 ml toluene) in a 250 ml beaker. The amount of the oil sample depends on acid content in the oil sample (Table 2-6).

Table 2-6 Recommended Size of Test Portion

Acid number	Mass of test portion, g	Accuracy of weighting, g
0.05 ~ < 1.0	20.0 ± 2.0	0.10
1.0 ~ < 5.0	5.0 ± 0.5	0.02

5. Titration of oil sample with alcoholic KOH solution: add suitable amount of KOH solution and wait until a constant potential has been reached, then record the solution added and meter readings. When approaching the end point, reduce the portion of addition and record the meter carefully. For each set of samples, perform a blank titration of 125 ml of the titration solvent.
6. Calculation: Plot the volumes of KOH solution added versus the corresponding potential readings. Mark the end points A and B for oil sample and solvent, which reflect the largest potential changes for a unit KOH, calculate the TANs as the equation (1):

$$\text{Acid number, mg KOH/g oil} = (A - B) * M * 56.1/W \quad (2-24)$$

A: volume of alcoholic KOH solution used to titrate a sample to the end point that occurs at the meter reading corresponding to the PH 11 aqueous buffer, ml

B: volume corresponding to A for a blank titration , ml

M: Molarity of alcoholic KOH solution, mol/L

W: sample weight, g

Three typical titration curves for KOH standardization, solvent (blank), and oil sample are shown in Figures 2-5, 2-6 and 2-7, respectively. In each case, the end point can be clearly obtained.

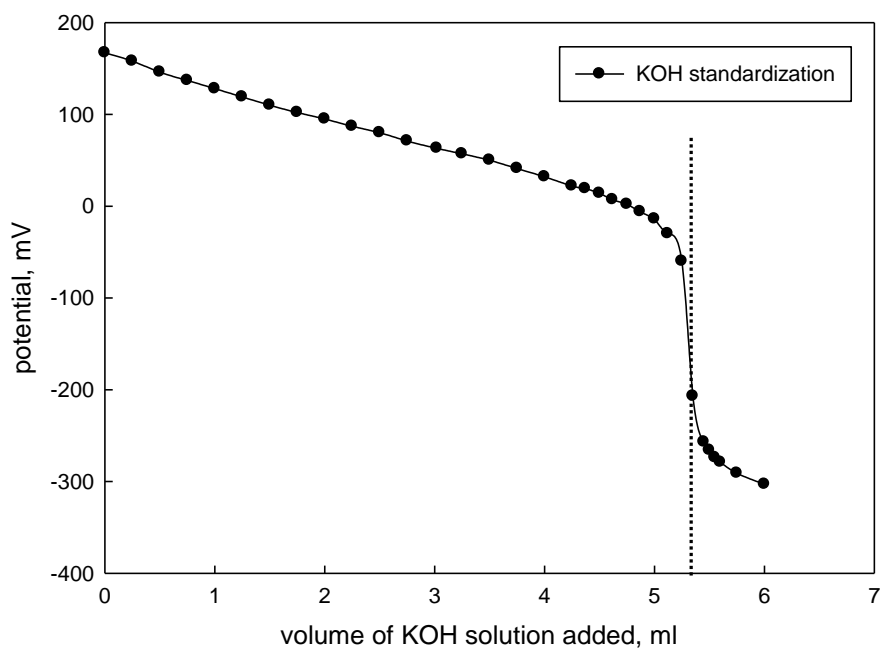


Figure 2-5 Titration Curve of KOH Standardization with Standard KHP Solution

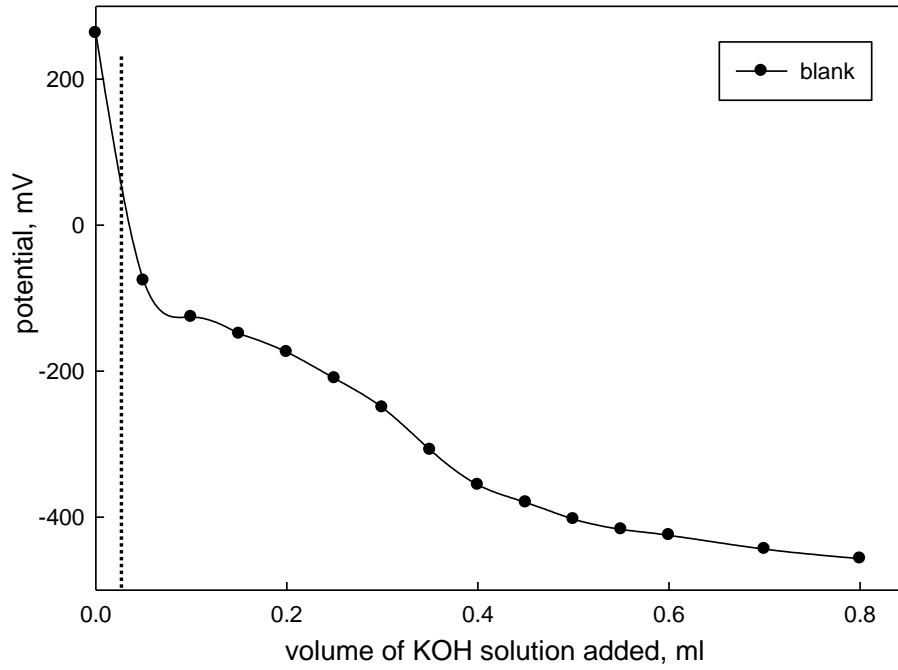


Figure 2-6 Titration Curve of the Titration Solvent Titrated with KOH

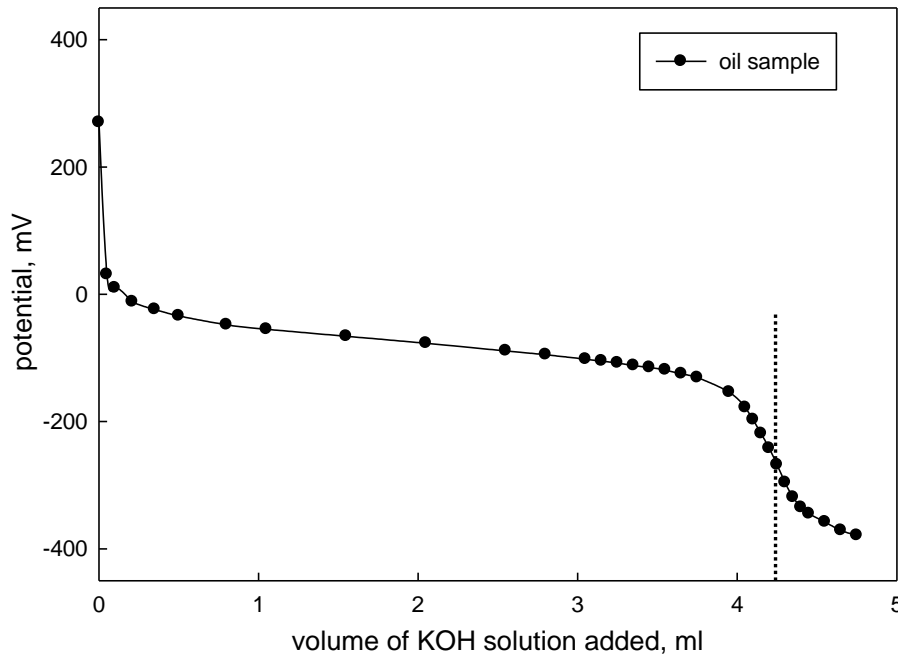


Figure 2-7 Titration Curve of an Oil Sample Titrated with KOH

### 2.3.4 Particle Size Distribution

One of the most common particle size distribution analysis technologies is laser diffraction for sizing particle from submicron to millimeter in size. During the laser diffraction measurement, particles are passed through a focused laser beam. These particles scatter light at an angle that is inversely proportional to their size. The angular intensity of the scattered light is then measure by a series of photosensitive detectors. In our work, the Mastersizer 2000 was used for particle size distribution analysis.

Table 2-7 Parameters Used in the Measurement of the Particle Size Distribution of the Fresh Particles

particles	dispersant	Reflectance index		Obscuration, %
		particle	dispersant	
Li <sub>2</sub> O	acetone	1.644	1.36	14.14
MgO	acetone	1.735	1.36	18.98
CaO	acetone	1.838	1.360	12.48
BaO	acetone	1.98	1.36	14.00
CaCO <sub>3</sub>	acetone	1.572	1.36	13.94

### 2.3.5 Scanning Electron Microscope (SEM)

Scanning electron microscopy (SEM) is one of the best known and most widely-used of the surface analytical techniques. High resolution images of

surface topography with excellent depth of the field are produced by using a highly-focused and scanning (primary) electron beam.

The SEM uses electrons instead of light to form an image. A beam of electrons (called primary electron beam) is produced at the top of the microscope by heating of a metallic filament. The electron beam follows a vertical path through the column of the microscope. It makes its way through electromagnetic lenses which focus and direct the beam down towards the sample. The primary electrons enter a surface with an energy of 0.5 - 30 keV, and generate many low energy secondary electrons. The intensity of these secondary electrons is largely dependent on the surface topography of the sample. When the secondary electrons are ejected from the sample, an image of the sample surface can be created by measuring secondary electron intensity as a function of the position of the scanning primary electron beam. Detectors collect the secondary or backscattered electrons, and convert them to a signal that is sent to a viewing screen similar to the one of an ordinary television, producing an image (<http://www.dynaloy.com/images/TechBrief042006.pdf>).

Because the SEM uses electrons to produce an image, most conventional SEM require that the samples be electrically conductive. All metals are conductive and require no preparation to be viewed using an SEM. In this work, metal oxides and metal carbonates were used as catalysts, which are non-conductive. To view non-conductive samples with SEM, the sample was covered with a thin layer of carbon. The instrument used was a JAMP 9500F by JEOL.

### **2.3.6 Energy Dispersive X-ray Spectroscopy (EDX)/SEM Analysis and Auger Electron Spectroscopy (AES)**

EDX is usually used in combination with SEM, and is not a surface science technique. When an electron beam with energy 3-20keV strikes upon a conducting sample, these electrons cause core electrons from the atoms contained in the sample to be ejected, resulting in a photoelectron and an atom with a core hole. The atom then relaxes through electrons with a lower binding energy moving into the core hole. The released energy can be converted into an X-ray. The energy of the X-rays emitted depends on the tested material. The X-rays are generated from a region about 2 microns in depth, and thus EDX is not a surface science technique. By moving the electron beam across the material, an image of each element in the sample can be acquired. Owing to the low X-ray intensity, images usually take a number of hours to acquire. Elements with low atomic number are difficult to detect by EDX. The SiLi detector is often protected by a Beryllium window. The absorption of the soft X-rays by the Be precludes the detection of elements below an atomic number of 11 (Na). In windowless systems, elements with as low atomic number as 4 (Be) have been detected, but the problems involved get worse as the atomic number is reduced.

As mentioned above, the released energy can be converted into an X-ray, and it can also emit an electron. This electron is called an Auger electron after Pierre Auger who discovered this relaxation process. After the emission of the Auger electron, the atom is left in a doubly ionized state. The energy of the Auger electron is characteristic of the element that emitted it, and can thus be

used to identify the element. Because Auger electrons can only escape from the outer 5-50 Å of a solid surface at their characteristic energy, this effect makes AES an extremely surface sensitive technique.

### **2.3.7 X-ray Diffraction (XRD)**

A crystal lattice is a regular three-dimensional distribution (cubic, rhombic, etc.) of atoms in space. These are arranged so that they form a series of parallel planes separated from one another by a distance  $d$ , which varies according to the nature of the material. For any crystal, plane exists in a number of different orientations, and each with its own specific  $d$ -spacing. When a monochromatic X-ray beam with wavelength  $\lambda$  is projected onto a crystalline material at an angle  $\theta$ , diffraction occurs only when the distance traveled by the rays reflected from successive planes differs by a complete number  $n$  of wavelengths. By varying the angle  $\theta$ , the Bragg's Law conditions are satisfied by different  $d$ -spacings in polycrystalline materials. Plotting the angular positions and intensities of the resultant diffracted peaks of radiation produces a pattern, which is characteristic of the sample. Where a mixture of different phases is present, the resultant diffractogram is formed by addition of the individual patterns (<http://www.panalytical.com/index.cfm?pid=135>).

X-ray powder diffraction pattern was recorded by employing a Philips X'per X-ray diffractometer with a CuK  $\alpha$  radiation source ( $\lambda=0.154056$  nm).

### **2.3.8 Thermal Gravimetric Analysis (TGA)**

TGA is an analytic technique that measures the weight loss (or weight gain) of a material against temperature or time. As materials are heated, they can lose weight from drying, evaporation and decomposition. Some materials can gain weight by reacting with the air. In my work, nitrogen was used for all of TGA tests to carry the produced gas out. The catalysts before and after the reaction were analyzed using TGA (STA409 PC by NETZSCH Thermal Analysis). Moreover, 4% calcium naphthenate was chosen as a model compound to verify whether calcium naphthenate was formed on the post-reacted catalyst. Two sets of temperature programs were employed. In the first temperature program, the material was heated from 30 °C to 800 °C at the rate of 2 °C/min, and then kept at 800 °C for 15 min. If the decarboxylation of naphthenic acids happened, the produced CO<sub>2</sub> might be adsorbed on the surface of CaO to form carbonate salt. To check whether carbonate salt was formed on the surface of the catalyst (decomposition temperature of CaCO<sub>3</sub> is in the range of 600 and 1080 °C (Guarino 2006; Malik and Gupta 1985; Wu and Lin 2005), the higher final temperature was used. In the second temperature program, the material was heated from 30 °C to 1200 °C at the rate of 2.3 °C/min, and then kept it at 1200 °C for 15 min.

### **2.3.9 GC Analysis**

After the reaction, the gas sample was collected with a syringe directly and injected in a GC. The GC used is Varian 3400X with a thermal conductivity

detector (TCD), which was equipped with a 30m×0.53mm Carboxen 1010 plot column. The software employed to calculate the area and determine the retention time of the peaks detected is the software of the star chromatography workstation. Helium was used as both the carrier gas and the reference gas.

The flow rates of the gases to the GC were measured and are shown in Table 2-8. These values were recorded at the temperatures of the GC column and injector of 35 °C and the temperature of the detector of 150 °C. The flow rate was checked frequently to ensure GC accuracy and reliability. The operation conditions of GC are shown in Table 2-8.

Table 2-8 GC Gas Flow Rates

Gas	Carrier gas	Make-up gas	Reference gas	Split gas
Flow rate, ml/min	24	6	30	0

Table 2-9 Operation Conditions of GC

GC method	status
Initial column temperature	35 °C
Initial column hold time	1 minute
Program 1 final column temperature	100 °C
Program 1 column rate	2 °C/min
Program 1 column hold time	5 minutes
Add next column program	no
Injector temperature	35 °C
Initial auxiliary temperature	20 °C
Initial auxiliary hold time	0 minute
Temperature program auxiliary	no
Detector temperature	150 °C
Detector A or B	A
TCD A initial attenuate	1
TCD A initial range	0.05
TCD A autozero on	yes
TCD A filament temperature	150 °C
TCD a polarity positive	no
Time program TCD	no
Initial relays	no
Time program relays	no
Add intergration section	no
Add time events section	no
Add peak table section	no

## 2.4 Results

The experimental results are summarized in this subsection. The results of the characterization of NA used in the study are presented first, which provides the information about what components of NA, used in the study, contains. Then,

the experimental error was analyzed based on measurements of TAN and CO<sub>2</sub> from different batches to demonstrate the reproducibility and reliability of reactions and measurements. In the subsection of the catalyst screening, the results are presented by showing IR spectra and TAN measurements of different liquid samples before and after the reaction with addition different catalysts. The results from analysis of the solid samples using different techniques are covered subsequently, to explore the mechanism of NA conversion. Following that, the kinetic data regarding NA decarboxylation reaction are given.

#### **2.4.1 Characterization of Commercial Naphthenic Acid**

The abundances of NA components with a given carbon number in a given Z family are displayed in a normalized matrix, and a 3-D distribution graph is also given. Table 2-10 shows the normalized matrix of the NA sample within the carbon number range of 5-20, with 0-6 rings (Z=0 to 12), and the 3-D distribution of carbon number and Z family in NA is shown in Figure 2-8.

Table 2-10 Distribution of Carbon Numbers and Z Families of the NA Sample

C number	z number							% carbon no
	0	2	4	6	8	10	12	
5	0	0	0	0	0	0	0	0
6	1	0	0	0	0	0	0	1
7	0	0	0	0	0	0	0	1
8	1	0	0	0	0	0	0	1
9	2	1	0	0	0	0	0	3
10	2	8	1	0	0	0	0	11
11	2	17	5	0	0	0	0	25
12	2	13	4	0	0	0	0	20
13	2	4	5	1	0	0	0	11
14	1	3	5	1	1	0	0	10
15	1	1	2	1	1	0	0	6
16	0	1	2	2	0	0	0	6
17	0	0	1	1	0	0	0	2
18	0	1	1	0	0	0	0	2
19	0	0	0	0	0	0	0	1
20	0	0	0	0	0	0	0	0
% by z No	15	50	26	6	2	1	0	100

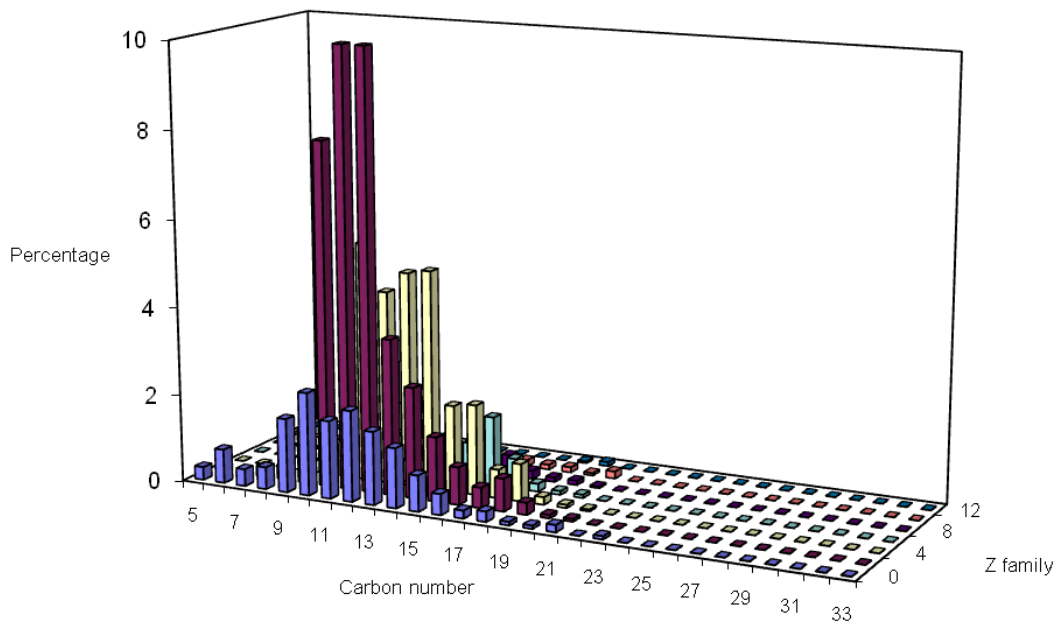


Figure 2-8 3-D Distribution of Carbon Numbers and Z Families of the NA Sample.

In Figure 2-8, the bars represent the percentage (by number of ions) of NA that account for a given carbon number of a given Z family. The sum of all the bars equals 100%.

As shown in Table 2-10, the most abundant components in the NA were in the Z family of 2, and have carbon numbers of 10, 11, and 12, with the percentages of 8, 17 and 13, respectively.

Through the characterization of NA, the percentage of components with the same carbon numbers in the same Z family in NA were known, and the molar weight of NA can be calculated to be 188.35 g/mol.

### 2.4.2 Error Analysis

To determine the reproducibility of the experimental measurements, nine reactions were performed under the same conditions in which oil mixtures with the initial TAN of 8.48 were tested, and the temperature was maintained at 365 °C, and the reactions lasted for 60 minutes. After the reaction, the gas samples were firstly collected and injected into a GC to measure CO<sub>2</sub> quantitatively, and then the TAN of the oil mixtures were measured using an automatic titrator. For TAN measurement, each sample was titrated in duplicate (Table 2-11), and the average was applied for the analysis of the reproducibility of the measurements of TAN and CO<sub>2</sub> from different batches.

Table 2-11 Results of TAN Measurement of the Liquid Samples

Reaction #	1 <sup>st</sup> analysis	2 <sup>nd</sup> analysis	average	Difference%*
1	6.39	6.37	6.38	0.31
2	6.62	6.60	6.61	0.30
3	6.45	6.51	6.48	0.92
4	6.60	6.59	6.60	0.15
5	6.47	6.49	6.48	0.31
6	6.69	6.78	6.74	1.34
7	6.52	6.50	6.51	0.31
8	6.52	6.52	6.52	0
9	6.26	6.20	6.23	0.96

$$* \text{ difference \%} = \left| \frac{1st - 2nd}{average} \right| * 100 \quad (2-27)$$

Table 2-12 Errors in Measurements of TAN and CO<sub>2</sub> from Different Batches

Run#	Average TAN, mg KOH/g oil	Concentration of CO <sub>2</sub> , mol/L
1	6.38	0.0157
2	6.61	0.0231
3	6.48	0.0256
4	6.60	0.0218
5	6.48	0.0181
6	6.74	0.0209
7	6.51	0.0291
8	6.52	0.0172
9	6.23	0.0124
Average	6.51	0.0204
Standard deviation	0.145	0.0052

### 2.4.3 Catalyst Screening

A low temperature of 300 °C was initially employed for the study of the decarboxylation of NA using the prepared catalysts. Based on the results of IR analysis, it was found that the conversion of NA reduction was very low, and Li<sub>2</sub>O/TiO<sub>2</sub> showed the highest activity among the tested catalysts, with a conversion of only 29 %. Therefore, a higher temperature of 385 °C was chosen for further catalyst screening.

A thermal reaction was run first to observe whether NA was removed without catalysts addition under the experimental conditions. The Figure 2-9 shows IR spectra of the oil sample before and after the thermal reaction, and the

peak corresponding to carbonyl group was magnified and stacked over the normal one.

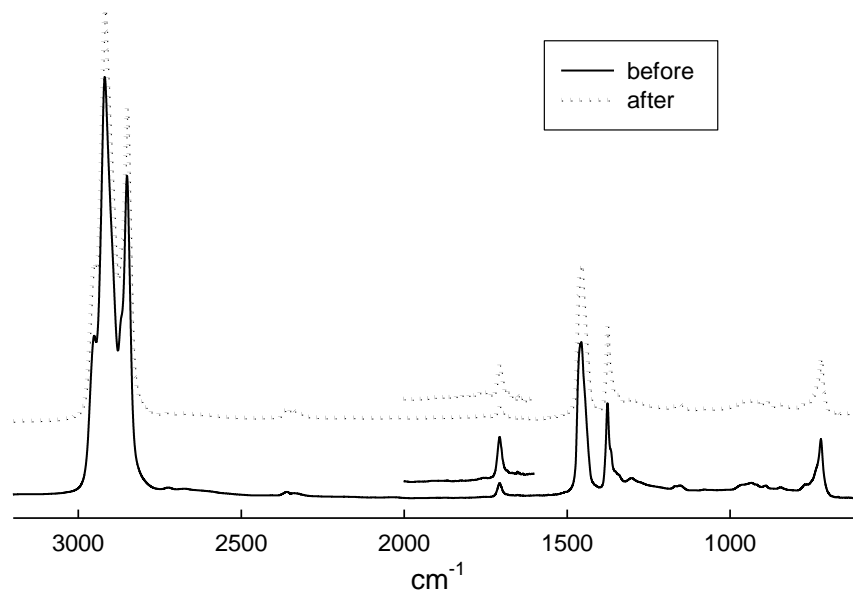


Figure 2-9 IR Spectra of Oil Samples from the Thermal Reaction

In Figure 2-9, no significant differences can be found between the two spectra. The area of the peak after the reaction corresponding to carbonyl group decreased by 17% compared to that of the peak before the reaction, which demonstrates that 17% of NA was removed at 385 °C without catalyst addition.

The two reactions were run at 385 °C for 3 h in the presence of the prepared and commercial CaO. IR spectra of the samples before and after reaction are shown in Figure 2-10. The comparison between the prepared and commercial CaO were made.

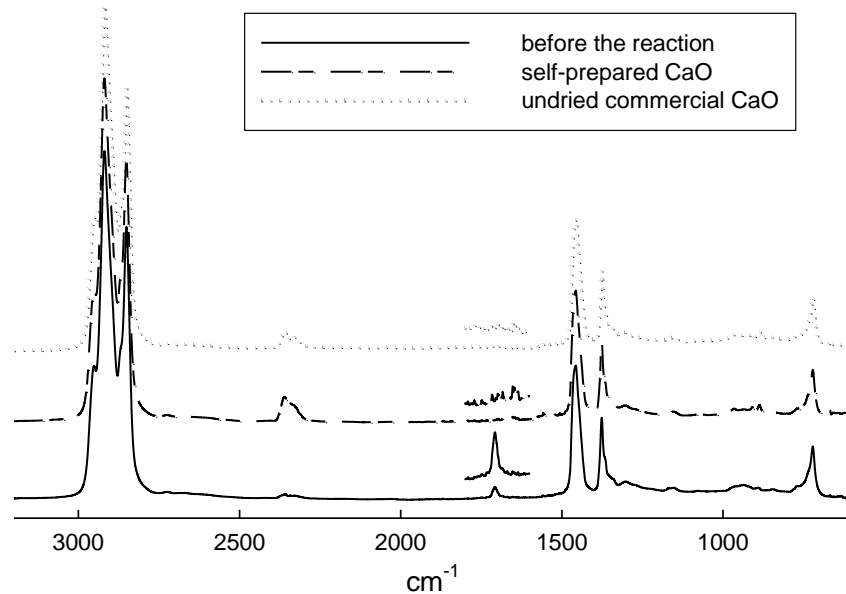


Figure 2-10 IR Spectra of Oil Mixtures before and after the Reaction in Presence of Prepared and Commercial CaO

As spectra shown in Figure 2-10, it is found that the areas of the peaks corresponding to carbonyl group decrease by the same extent for both post-reacted samples, indicating that both CaO are active in removing NA from the oil, and have the same activity. Considering the cost of catalyst preparation, the commercial CaO was used as catalyst in further studies.

The powders of CaO and CaCO<sub>3</sub> purchased from Sigma were dried at 105 °C overnight. Two reactions were run at 385 °C for 3 hours in the presence of the fresh and dried CaO. IR spectra of the samples before and after reaction are shown in the Figure 2-11. TAN of each sample measured by titration is also listed at the right side of the Figure 2-11.

The data in Figure 2-11 show that the peaks of the carbonyl group at  $1710\text{ cm}^{-1}$  decreased by the same extent after the reaction with addition of different catalysts. The results of TAN measurements show that TAN values of oil samples were reduced from 3.00 to 0.58 with the fresh CaO addition. Similarly, TAN values of the oil sample were decreased from 3.00 to 0.60 in the presence of the dried CaO. Therefore, NA was removed in the presence of the catalysts of either fresh or dried CaO, and both catalysts have a similar activity for acid removal. The fresh CaO was employed directly thereafter.

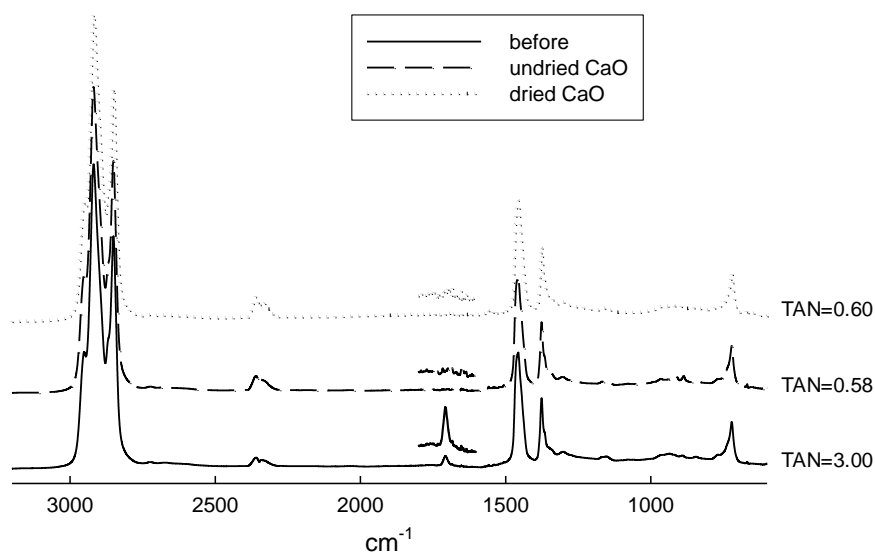


Figure 2-11 IR Spectra of Oil Mixtures before and after the Reaction in Presence of Non-dried and Dried CaO at  $385\text{ }^{\circ}\text{C}$  for 3 hours

To compare the reactivity of CaO and  $\text{CaCO}_3$  on the acid removal, the equivalent amount of  $\text{CaCO}_3$  and CaO (molar ratios of metal to NA loaded are the same) were loaded into two reactors individually. The reactions last for 3 h at

385 °C. Figure 2-12 shows the spectra of the mixtures before and after the reactions. The single peak of carbonyl group was enlarged and stacked over the normal one. The TAN of oil mixtures are also shown at the right side of the figure.

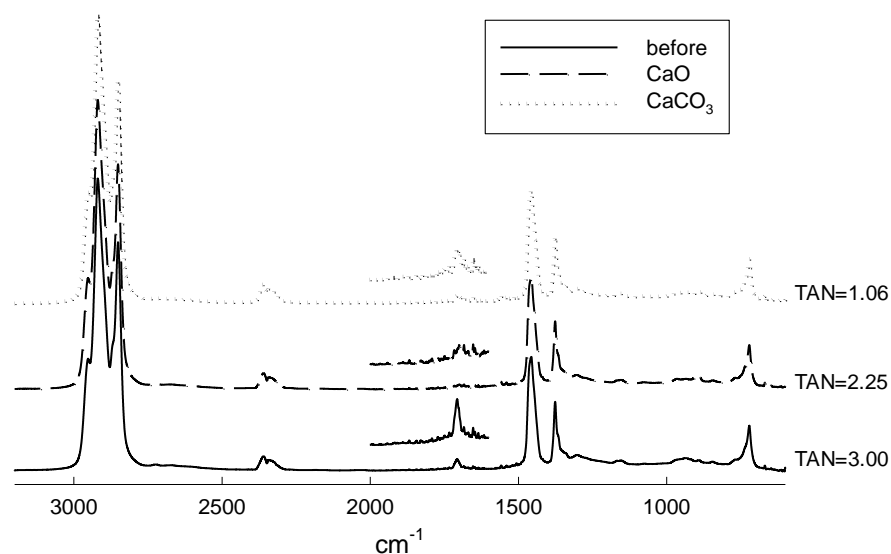


Figure 2- 12 IR Spectra of Oil Mixtures before and after the Reaction in Presence of CaO and CaCO<sub>3</sub> at 385 °C for 3 hours

IR spectra in Figure 2-12 show that for the post-reacted sample, the peaks corresponding to the carbonyl group was reduced significantly in the presence of the catalyst of CaO compared with the un-reacted sample. However, the peak area of carbonyl group did not decrease very much with CaCO<sub>3</sub> addition. This trend is in agreement with the TAN measurement. With the addition of CaCO<sub>3</sub>, the TAN values of the oil mixtures before and after the reaction decreased from

3.04 to 2.25. The acid conversion, based on TAN reduction, was 26.0%. For an equivalent amount of CaO addition, TAN reduction was 65.2%. CaO exhibited higher activity for acid removal than CaCO<sub>3</sub> under the same experimental conditions.

The commercial reagents Li<sub>2</sub>O, MgO and BaO were also employed as catalyst under the same reaction conditions as reagents of CaO and CaCO<sub>3</sub> shown previously. The liquid samples were also analyzed by FTIR analysis and TAN measurement. The results are shown in Figure 2-13.

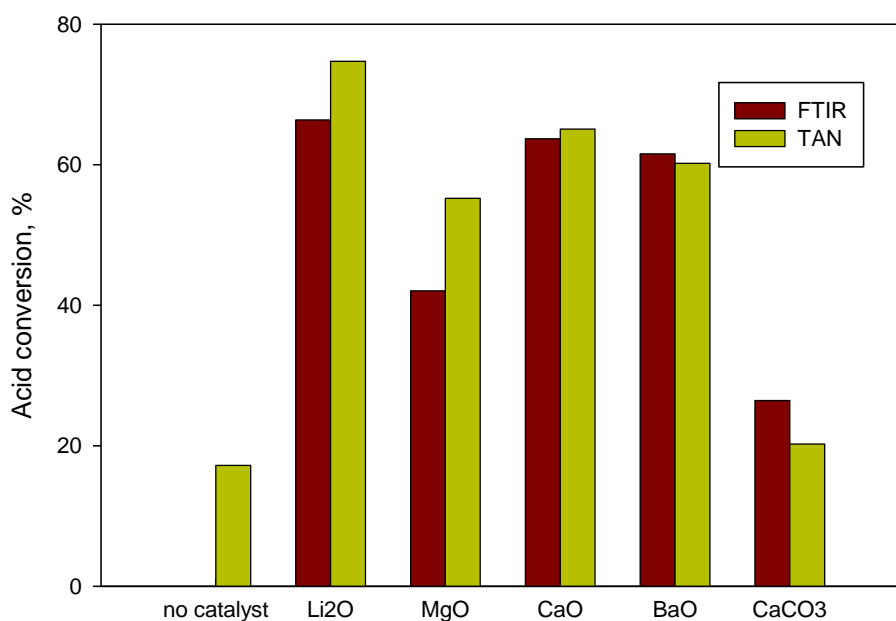


Figure 2-13 Results from TAN Measurement and FTIR Analysis for the Tested Catalysts

As shown in Figure 2-13, the NA content in the mixture decreased by 17% without addition of the catalyst, which was similar to 26% in presence of

CaCO<sub>3</sub>. However, with addition of the tested metal oxides, NA in the mixture decreased significantly, about 70% of acid was removed in the presence of Li<sub>2</sub>O. Among the tested metal oxides, MgO shows the least activity in NA removal; the NA concentration decreased by 42%. TAN measurement and FTIR analysis showed the same trend in decrease of acids with addition of different catalysts. The effectiveness of the tested catalysts decreased in the order: Li<sub>2</sub>O>CaO>BaO>MgO>CaCO<sub>3</sub>. Li<sub>2</sub>O was the most active for removal of NA, and CaCO<sub>3</sub> was the least effective, which is different from the observations of Guarino (Guarino 2006) that the catalyst of CaCO<sub>3</sub> was highly active in the gas-phase decarboxylation reaction under the experimental conditions. Considering the prices of the reagents and their activities shown in Figure 2-14, CaO was chosen as catalyst for the further study.

#### **2.4.4 Analysis of Solids and Catalysts from Screening Experiments**

To explore what drive the difference in activities of catalysts in removing NA from oil, and what intermediate products were formed during the reaction processes, the solid samples before and after the reaction were analyzed by using different analytical techniques, the results were summarized as follows:

##### **2.4.4.1 Particle Size Distribution**

Through the particle size distribution analysis by using the Mastersizer, the results were reported by the quantity  $d(z)$ , which is defined as the fraction  $z$  of the particles are of size  $d(z)$  or small when the particles are arranged from

smallest to largest diameter. For example,  $d(0.5)=10$  represented 50% of the particle in the sample are of a size 10  $\mu\text{m}$  or less. The particle size distribution of the tested samples are recorded in Table 2-13.

Table 2-13 Particle Size Distribution of the Tested Catalysts

particles	d(0.1), $\mu\text{m}$	d(0.5), $\mu\text{m}$	d(0.9), $\mu\text{m}$	Specific surface area, $\text{m}^2/\text{g}$	dispersant
Fresh $\text{Li}_2\text{O}$	4.353	15.566	36.472	0.308	acetone
Spent $\text{Li}_2\text{O}$	7.749	63.443	79.682	0.153	acetone
Fresh $\text{MgO}$	1.414	2.631	5.203	0.704	acetone
Spent $\text{MgO}$	1.413	3.183	13.180	0.602	acetone
Fresh $\text{CaO}$	2.113	4.49	9.627	0.476	acetone
Spent $\text{CaO}$	1.948	5.058	14.221	0.459	acetone
$\text{BaO}$	4.249	15.367	35.104	0.125	acetone
Spent $\text{BaO}$	2.676	14.985	43.759	0.151	acetone
$\text{CaCO}_3$	19.8	37.817	66.733	0.201	acetone
Spent $\text{CaCO}_3$	16.829	33.327	59.987	0.080	acetone

#### 2.4.4.2 SEM

The morphology of the powder  $\text{CaO}$  before and after the reaction was examined by observing the SEM images (Figures 2-14, 15, and 16).

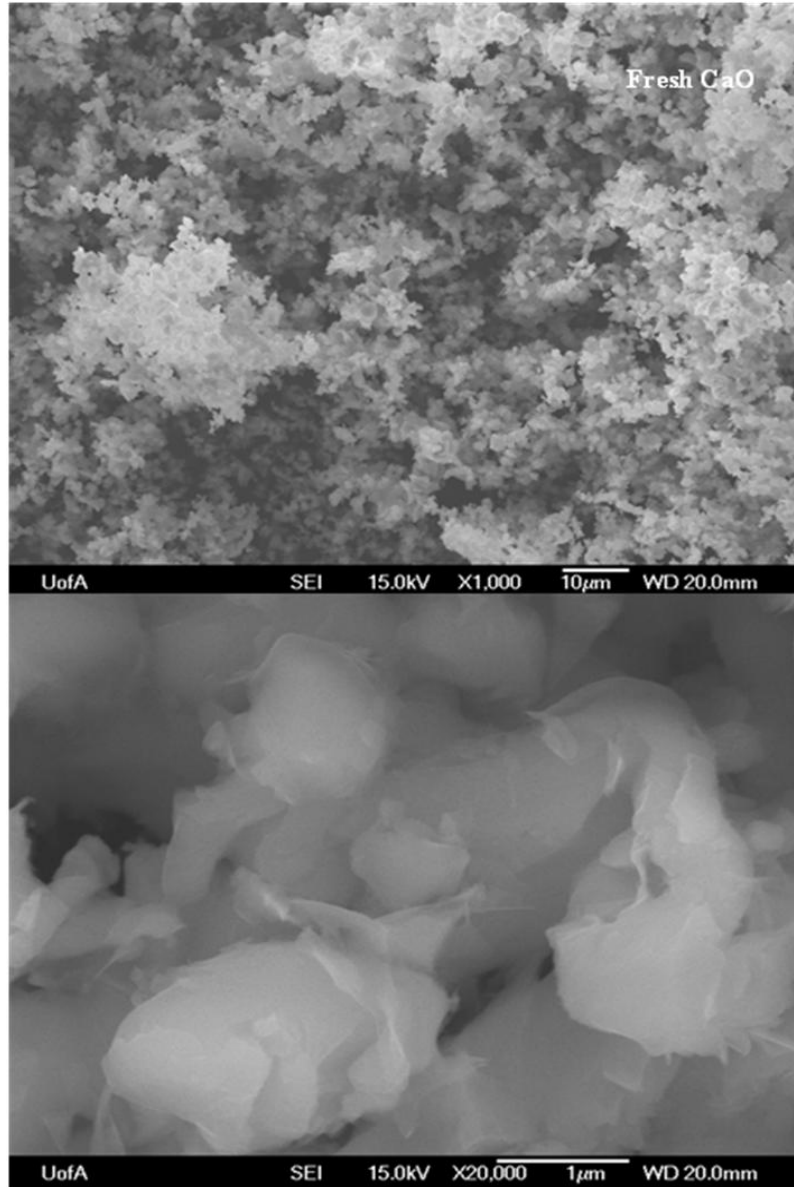


Figure 2-14 SEM Micrograph of the Fresh CaO

Figure 2-15 shows the low and high magnification SEM images of the fresh CaO. The high magnification SEM image showed that the fresh CaO had a fluffy appearance, like cotton wrapped by petals.

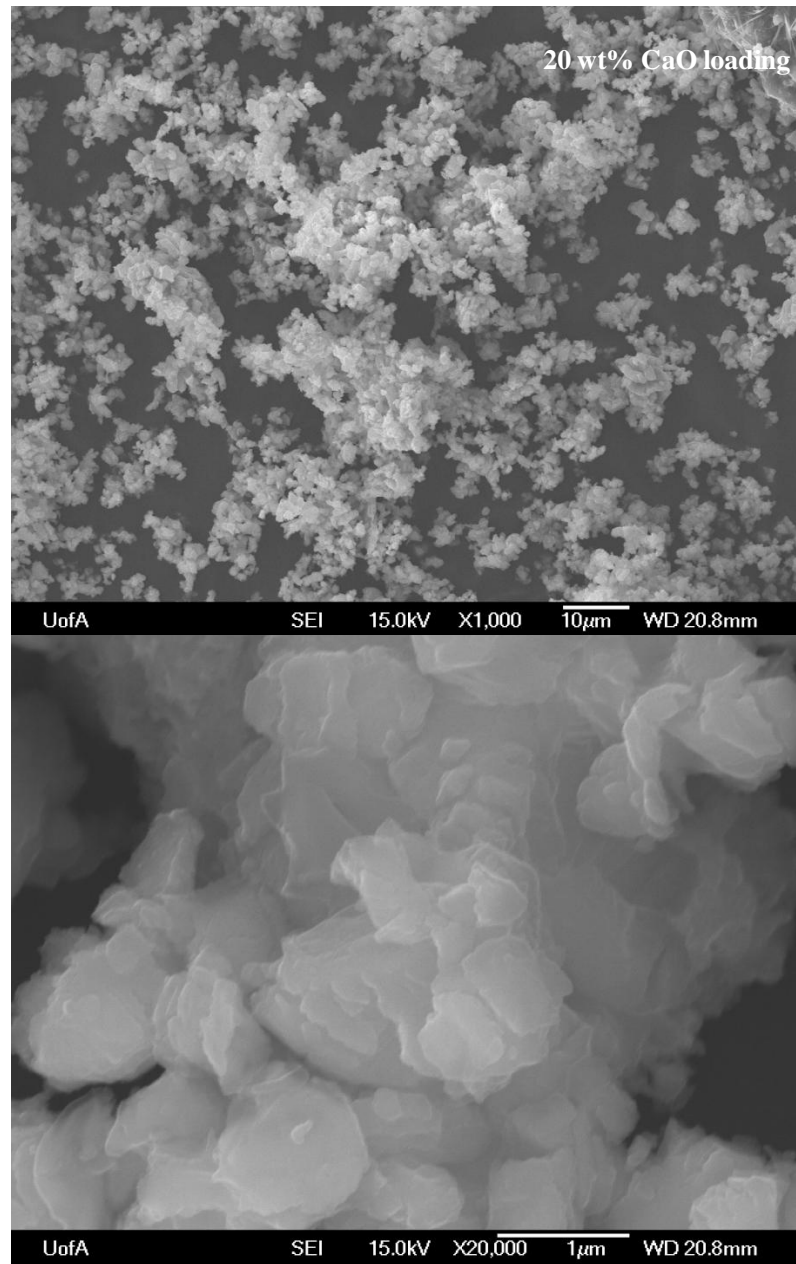


Figure 2-15 SEM Micrographs of the Solids after the Reaction with 20 wt% of CaO Loading

Figure 2-15 shows the low and high magnification SEM images of the CaO after reaction. SEM images reveal that the texture of the CaO became tighter than that of the fresh CaO, and the crystalline phase underwent an obvious

change. The difference in the fresh and post-reacted CaO suggests that there might have a new compound or reaction intermediate with different crystalline structure formed during the reaction process.

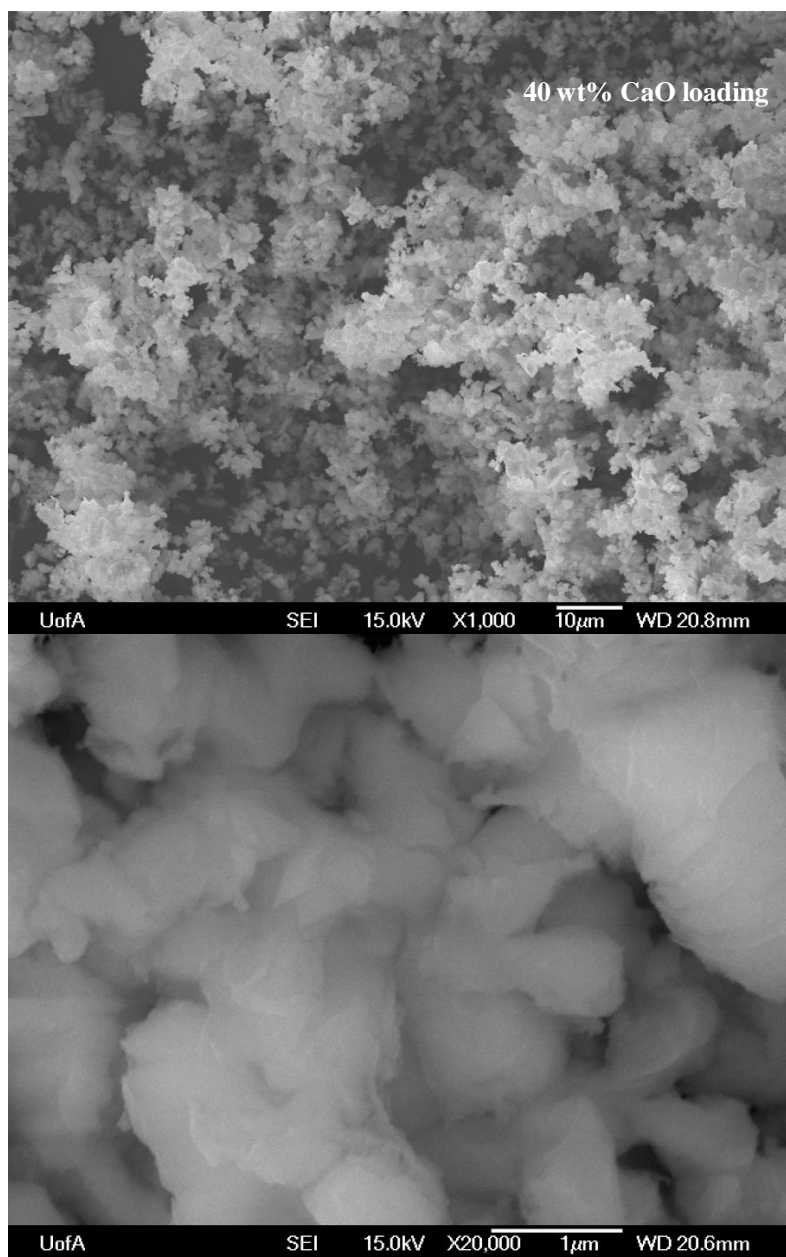


Figure 2-16 SEM Micrographs of the Solid Sample after the Reaction with 40 wt% of CaO Loading

The reaction was rerun at the same conditions except the catalyst loading was doubled, then after the reaction the morphology of the post-reacted CaO was also examined by SEM (Figure 2-16). The low magnification SEM image is similar to that of the fresh CaO, but the high magnification image shows that the texture of the crystal became a little bit tighter than that of the fresh, and much looser than that of the post-reacted CaO with low loading. The reason for the observation is that there was some unreacted CaO with the loose structure left in the solid sample although the new compound with the tight crystalline structure was formed during the reaction process because of the more fresh CaO loaded in the reactor.

#### 2.4.4.3 XRD

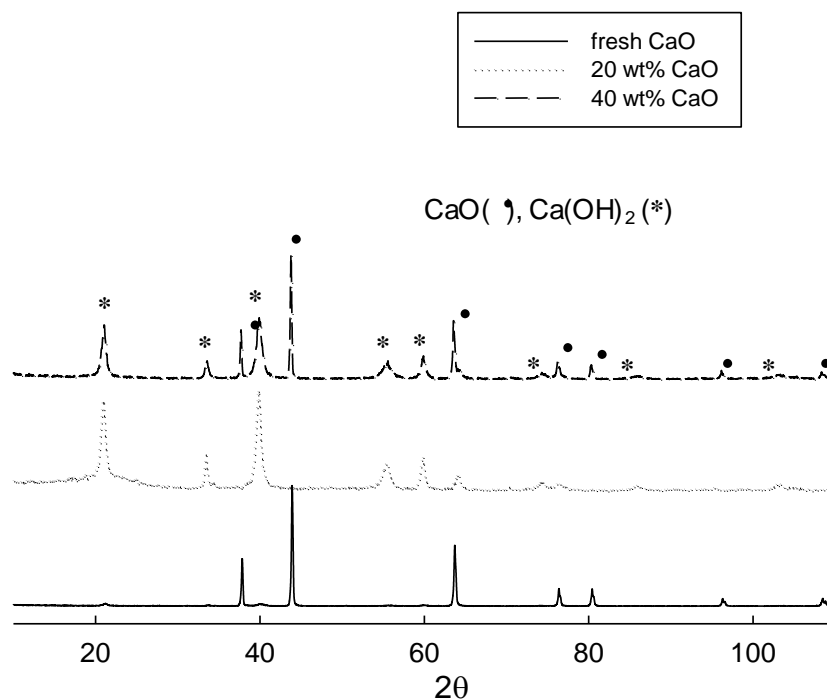


Figure 2-17 XRD Profile of CaO before and after the Reaction

Figure 2-17 shows XRD patterns of CaO before and after the reaction. In Figure 2-17, the solid line denotes the XRD pattern of the fresh CaO, and the dotted line denotes the XRD pattern of the post-reacted CaO in which 20 wt% of CaO was loaded in the reactor, and the medium dash line denotes the XRD pattern of the post-reacted CaO in which 40 wt% of CaO was introduced in the reactor. All recognizable diffraction peaks in the patterns can be indexed to cubic lime CaO structure and hexagonal portlandite  $\text{Ca(OH)}_2$  structure with lattice parameters of 4.8049 Å, and  $a=3.5853$  Å and  $c=4.895$  Å, respectively. As XRD patterns shown, the diffraction peak of the cubic crystal at  $2\theta=43.793^\circ$  in the sample with 20 wt% of CaO loading completely disappeared, and the diffraction peaks of CaO crystals at other positions became smaller comparing with those of the fresh CaO. However, the diffraction peaks of CaO in sample with 40 wt% of CaO loading appeared the similarity to those of the fresh CaO. In addition, the diffraction peaks of the  $\text{Ca(OH)}_2$  crystals were found in both of the post-reacted catalysts.  $\text{Ca(OH)}_2$  is due to the hydration of CaO in which water comes from the decarboxylation reaction of NA.

To verify the hypothesis that the formation of the calcium naphthenate was an intermediate step of the decarboxylation of the NA, the reaction was run at 375 °C for 60 minutes in which only 4% of the commercial calcium naphthenate and the CaO were loaded in the reactor. After the reaction, the morphology of the solid CaO was examined by XRD, as shown in Figure 2-18.

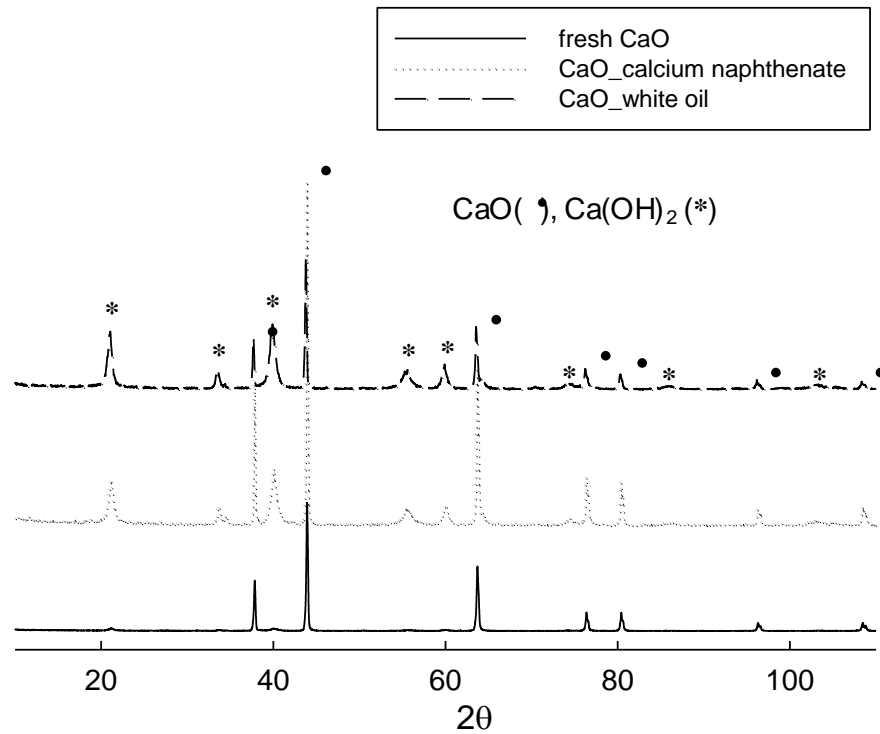


Figure 2-18 XRD Profile of CaO before and after the Reaction

Figure 2-18 shows the XRD patterns of the fresh CaO (named as S1), the post-reacted CaO from the reaction in which CaO and calcium naphthenate were introduced in the reactor (S2), and the other post-reacted CaO from the reaction in which CaO and the mixture of NA and white oil were charged in the reactor (S3). As XRD pattern shown in Figure 2-18, all recognizable diffraction peaks in the patterns can be indexed to cubic lime CaO structure and hexagonal portlandite Ca(OH)<sub>2</sub> structure with lattice parameters of 4.8049 Å, and a=3.5853 Å and c=4.895 Å, respectively. The post-reacted samples of S2 and S3 presented the similar X-ray diffraction patterns of the crystals. Moreover, diffraction peaks of the Ca(OH)<sub>2</sub> crystal were only found in the post-reacted samples of S2 and S3 comparing with the diffraction pattern of the fresh CaO (S1). Therefore, the XRD

patterns of the solid samples before and after the reaction proved that calcium naphthenate is an intermediate product in the decarboxylation reaction of NA.

#### 2.4.4.4 IR Spectra

The catalysts of CaO before and after the reaction were analyzed using FTIR to detect the existence of calcium naphthenate in solid samples shown in Figure 2-19. The typical IR adsorption of C=O in naphthenate has a very strong and characteristic band in the region  $1610\text{-}1550\text{ cm}^{-1}$  due to the asymmetric stretching vibration of  $\text{CO}_2^-$ , which is different from C=O in naphthenic acids (around  $1700\text{ cm}^{-1}$ ).

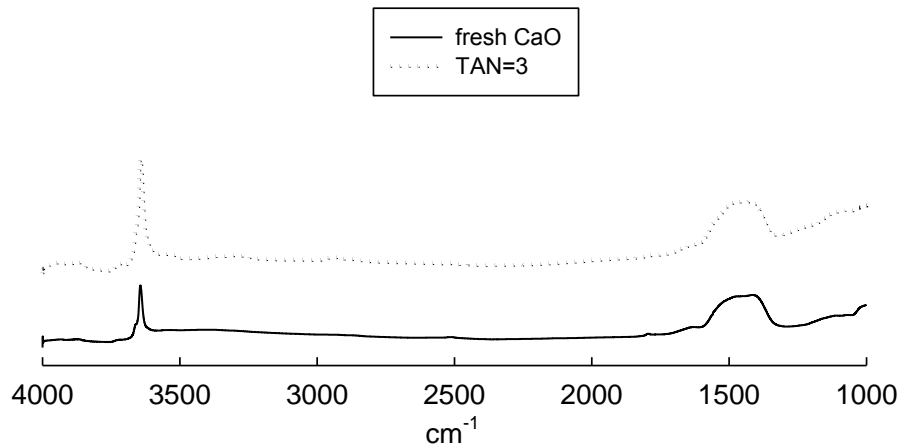


Figure 2-19 IR Spectra of Solid Samples before and after the Reaction with the Low Initial TAN of 3

As shown in Figure 2-19, the IR spectra of CaO before and after the reaction were similar, and the separated peak corresponding to C=O in calcium

naphthenate was not found in the spectra. There were two possibilities for this behavior. One is that no calcium naphthenate is indeed formed in the reaction, and the other is that the produced calcium naphthenate can not be detected because of its low concentration. Therefore, the other reaction was run in which the initial TAN of the reactant mixture was increased from 3 to 45, and 4 wt% of CaO was charged in the reactor. The post-reacted CaO was analyzed by FTIR shown in Figure 2-20. The commercial calcium naphthenate solution was also analyzed for comparison.

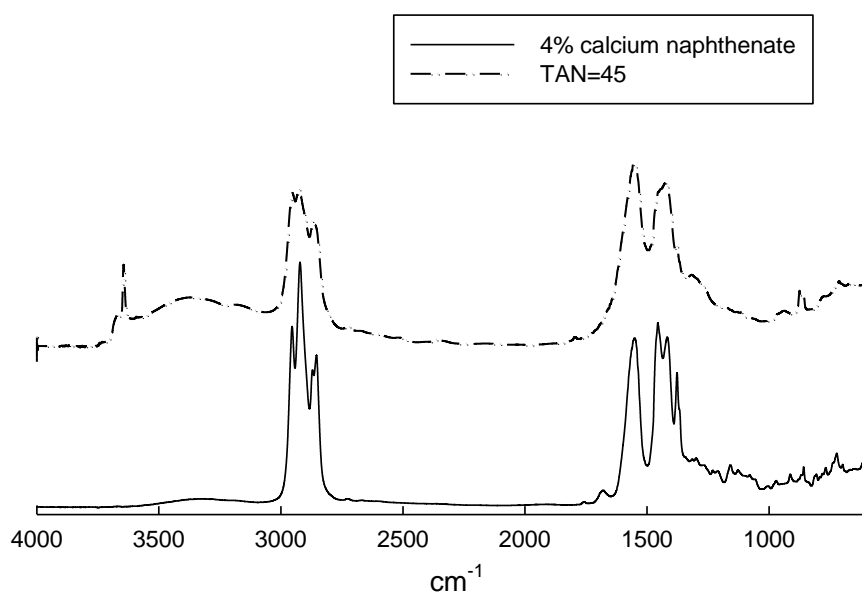


Figure 2-20 IR Spectra of 4% Calcium Naphthenate and the Solid Sample after the Reaction with the high Initial TAN of 45

It can be seen in Figure 2-20 that both IR spectra show the peaks at around  $1560\text{ cm}^{-1}$ . As described previously,  $\text{CO}_2^-$  in calcium naphthenate exhibits a sharp peak in the range  $1610\text{-}1550\text{ cm}^{-1}$ . Therefore, the peak at around  $1560$

$\text{cm}^{-1}$  was attributed to IR adsorption of  $\text{CO}_2^-$  in calcium naphthenate. The conclusion was drawn that the post-reacted CaO contained calcium naphthenate, in other words, calcium naphthenate was formed in the reaction. At the same time, the second possibility was verified that the produced calcium naphthenate could not be detected previously because of its low concentration.

#### **2.4.4.5 TGA**

Figure 2-21 shows the TGA results of the commercial calcium naphthenate. It is evident from the TGA curve that the first big weight loss below 200 °C was due to evaporations of solvents in calcium naphthenate sample, such as mineral spirits, dipropylene glycol monomethyl ether as well as hexylene glycol, whose boiling points are lower than 200 °C. The second mass loss between 400 and 500 °C in the curve is due to the decomposition of calcium naphthenate and calcium neodecanoate. The source of the third mass loss is not ascertained.

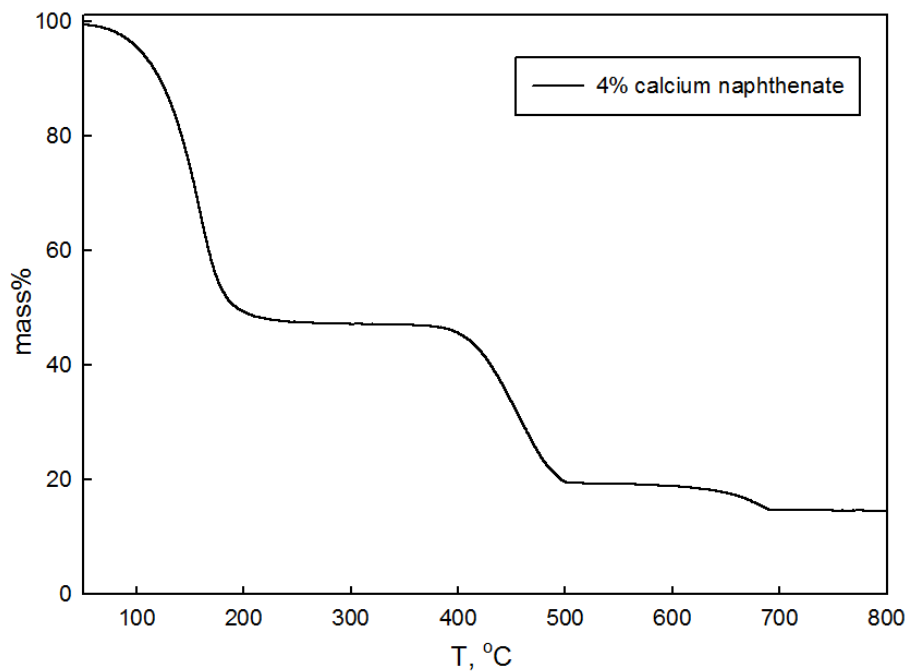


Figure 2-21 TGA Results Showing Mass Loss of 4% Calcium Naphthenate

The fresh and post-reacted CaO were analyzed by TGA to trace the formation of calcium naphthenate, and the thermal decomposition of the solid samples before and after the reaction were compared and shown in Figure 2-22.

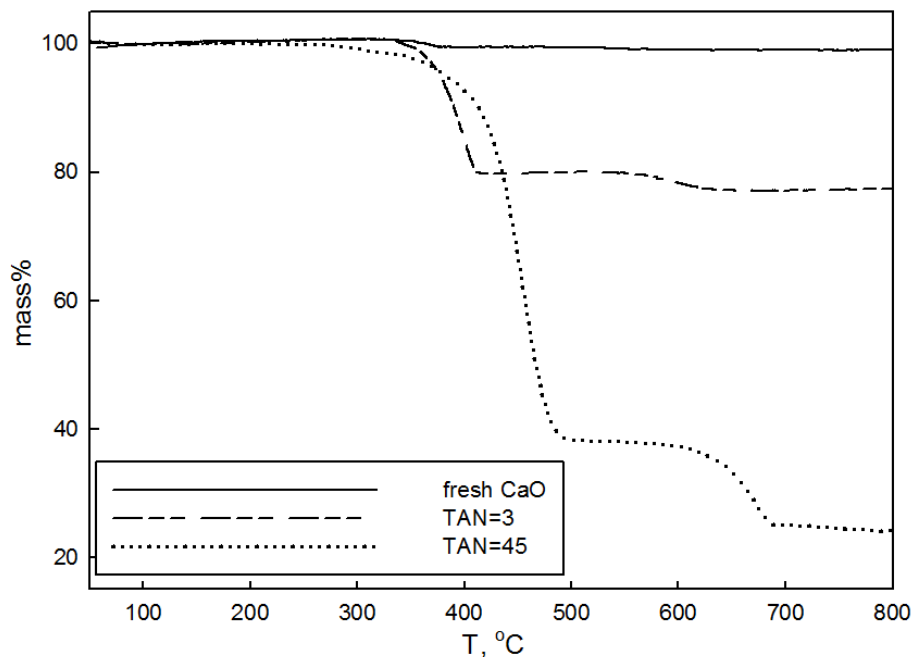


Figure 2-22 TGA Results of Post-Reaction Solid Samples and 4% Calcium Naphthenate

The data of Figure 2-22 show that the fresh CaO sample had a slight mass loss between 350 and 380 °C which comes from the decomposition of  $\text{Ca}(\text{OH})_2$ . The presence of a small amount of the  $\text{Ca}(\text{OH})_2$  in the fresh CaO sample is due to CaO hydration. The mass loss in both post-reacted samples are due to the decomposition of  $\text{Ca}(\text{OH})_2$  below 400 °C, followed by the decomposition of calcium naphthenate between 380 and 500 °C. Since the decomposition temperature of  $\text{Ca}(\text{OH})_2$  and calcium naphthenate overlap each other, the weights of the post-reacted samples decreased smoothly although the decomposition of two compounds happened. TGA results also show that the calcium naphthenate was formed during the reaction process.

#### **2.4.5 Solubility of Calcium Naphthenate in the Oil**

As observed in the analysis of IR and TGA, it is found that calcium naphthenate is formed during the reaction process, but there are no evidences to demonstrate what phase status calcium naphthenate is when it is formed, although it was found in the post-reacted solid samples. In order to test the solubility of calcium naphthenate in the oil at the reaction conditions, a new reaction system was deliberated. A second solid of kaolin clay was added in the reaction system at a ratio of about 1 part kaolin clay to 4 parts CaO, the initial TAN of the oil mixture is 8.5, the reaction undergoes at 385 °C for 30 minutes. If calcium naphthenate is dissoluble in the oil at the reaction condition, it will precipitate and deposit on the surface of the solid particles when the reactor is quenched in a water bath, then the kaolin clay will exhibit Ca with the suitable analytic technique.

The post-reacted solid sample was collected and washed with toluene, after dryness, the sample was analyzed by using EDX/SEM and AES, respectively. The fresh solid sample was also analyzed for comparison.

In EDX/SEM analysis, due to strong absorption from the X-ray detector window, oxygen results are lower than the actual value, and change over time as oil from the vacuum system accumulates on the window. Therefore, results have been provided without oxygen included in the analysis. In addition, these results can only be regarded as semi-quantitative due to the roughness of the sample surfaces (the X-ray take-off angle is not a constant).

Table 2-14 Results of EDX Analysis of the Fresh Mixture of CaO and Kaolin Clay

element	ZAF	Norm Wt%	Atomic%
Al	1.7	2.72	3.9
Si	1.4	6.15	8.45
Ca	1.0	91.13	87.67

Table 2-15 Results of EDX Analysis of the Post-reacted Mixture of CaO and Kaolin Clay

element	ZAF	Norm Wt%	Atomic %
Mg	2.1	0.5	0.8
Al	1.7	2.7	3.9
Si	1.4	6.5	8.9
Ca	1.0	90.3	86.4

The solid sample before and after the reaction were analyzed by using AES. For analysis, the little amount of the solid sample was dispersed on a stainless steel disc, the particles were chosen arbitrarily by SEM monitoring, and scanned by AES. Figures 2-23 and 24 show the AES results, showing the elemental compositions in the post-reacted solid particles.

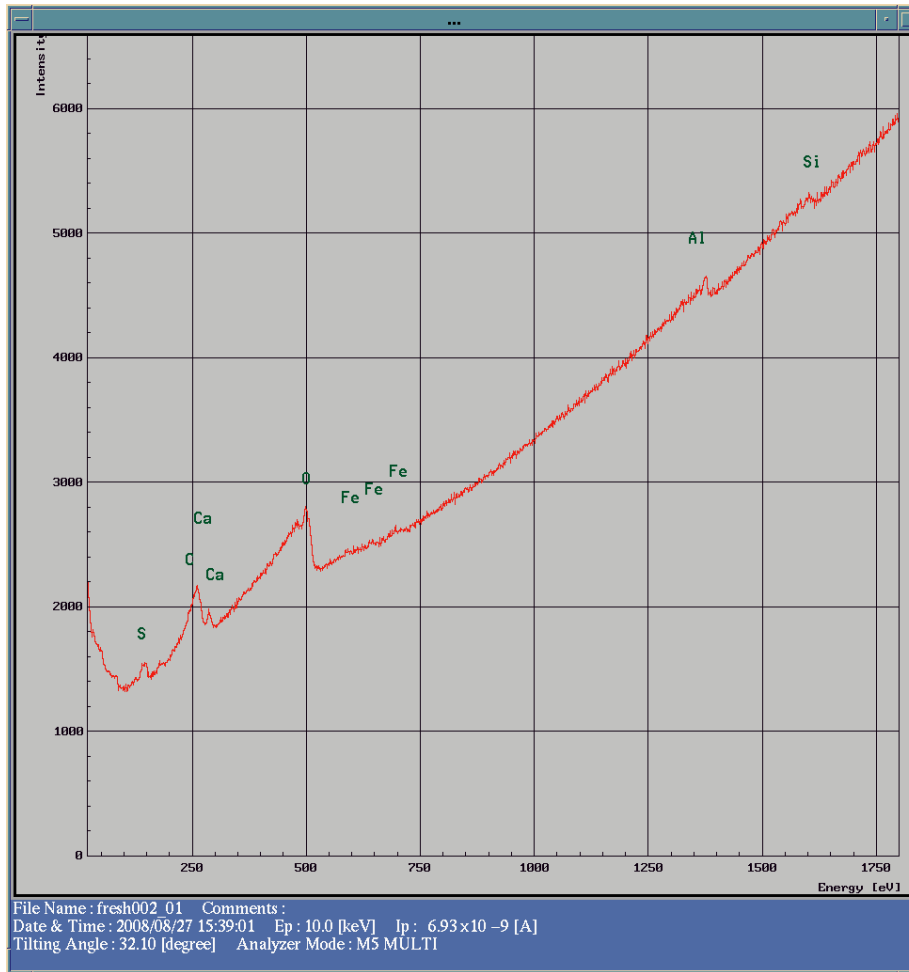


Figure 2-23 Elemental Composition of the Fresh Mixture of CaO and Kaolin Clay by AES Analysis

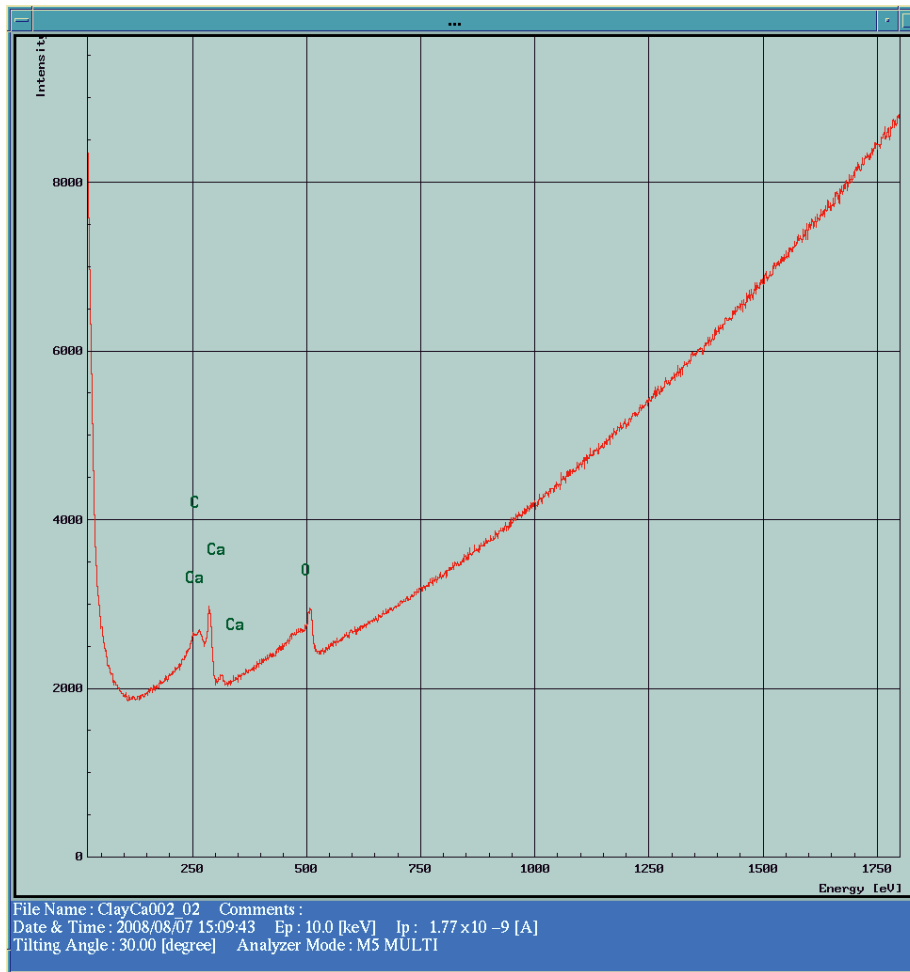


Figure 2-24 Elemental Composition of the Post-reacted Mixture of CaO and Kaolin Clay by ASE Analysis

As shown in Figure 2-23, elements of Ca, O, C, S, Al, Si, and Fe are found in the AES spectrum of the fresh mixture of CaO and kaolin clay. For the post-reacted mixture of CaO and kaolin clay, elements of Ca, C, and O are found in its AES spectrum (Figure 2-24).

#### 2.4.6 Kinetics of Catalytic Decarboxylation of NA in Oil

The kinetics of decarboxylation was also studied experimentally using a microbatch reactor. Three mixtures with TAN of 5.1, 8.5, and 10.8 were prepared for the study. The experiments were carried out at 365, 375, and 385 °C, respectively. For most runs, 20 wt% of CaO on a basis of NA weight was loaded. The tightened reactor was pressurized with N<sub>2</sub> at 400 kPa. Each series of reactions with the same initial TAN lasted for 5, 15, 30, 45, 60, and 90 minutes, respectively. A series of thermal reactions with the initial TAN of 8.48 was run at 365 °C for comparison (Figure 2-25).

To determine the temperature of the reactor when it was immersed in the sand bath, Kanda (Kanda 2003) tested the interior temperature of the reactor when the temperature of the sand bath was maintained at 385 °C by using a special reactor with a thermocouple mounted inside of the reactor. The measurement showed that it took 3 minutes to heat up the reactor to 95% of the final steady state temperature of 385 °C, in addition, a similar oscillatory temperature cycle was noted with a period of 3 minutes and a span of 1.2 °C. The actual steady state average temperature inside the reactor would be 2-3 °C lower than the temperature setpoint of the sand bath. Considering the liquid loading in our work was more than 3.4g used for the tested in Kanda's work, it was estimated that the reactor takes 5 minutes to reach the reaction temperature. After 5 minutes, the isothermal reaction takes place. In the following kinetic plots, all the regression lines are only for the isothermal period after 5 minutes heating-up.

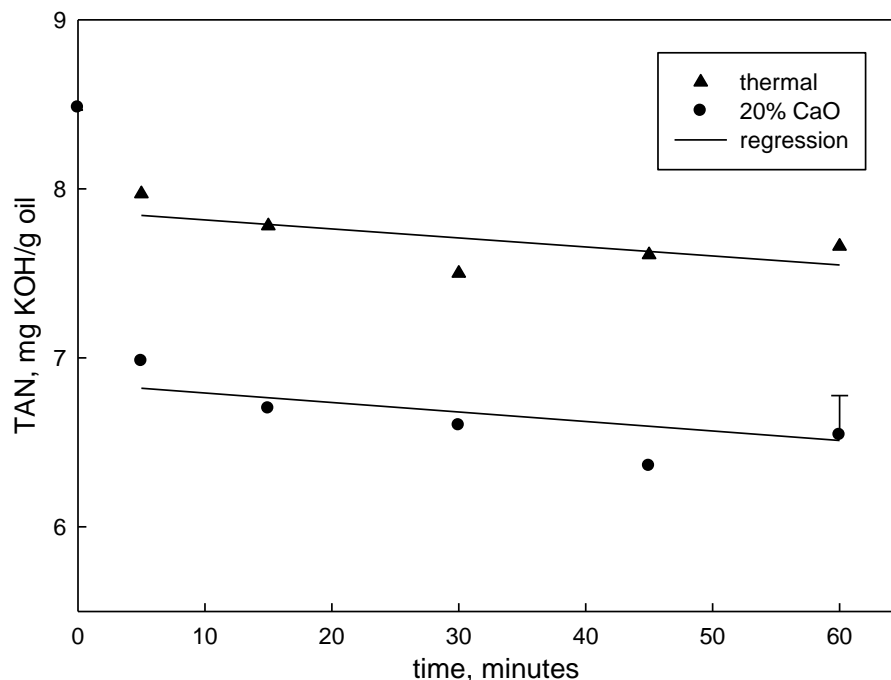


Figure 2-25 Reduction of TAN at 365 °C against time for the carrier oil mixtures with initial TAN of 8.5 without and with addition of 20 wt% of CaO. Error bars show 2 times the standard deviation of experiments.

The data shown in Figure 2-25 demonstrate that the TAN of oil mixtures decreased at 365 °C against the reaction time for the carrier oil mixtures with initial TAN of 8.5 with and without addition of CaO, respectively. It was found that the NA removal was much more effective in the presence of CaO than that in the thermal reactions. During the thermal reaction, about 6% of TAN was removed in the stage of heating-up, and the TAN of the oil mixture decreased slightly by 4% during the isothermal reaction process. The TAN of the oil mixture in the catalytic reaction decreased from 6.98 to 6.38 during the isothermal period, and 17.7% of TAN was removed during the heating-up. The reason for the big difference in TAN reduction during the heating-up could be

that the NA in the oil mixture was absorbed on the surface of the solid spontaneously when the catalyst was loaded in the reactor, but the formed calcium naphthenate could not decompose quickly because the reaction temperature was too low to facilitate the decomposition of calcium naphthenate, which is the reason for the low removal of NA during the reaction process although TAN of the oil mixture decreased significantly in the heating-up. This observation is consistent, therefore, with a two-step reaction process.

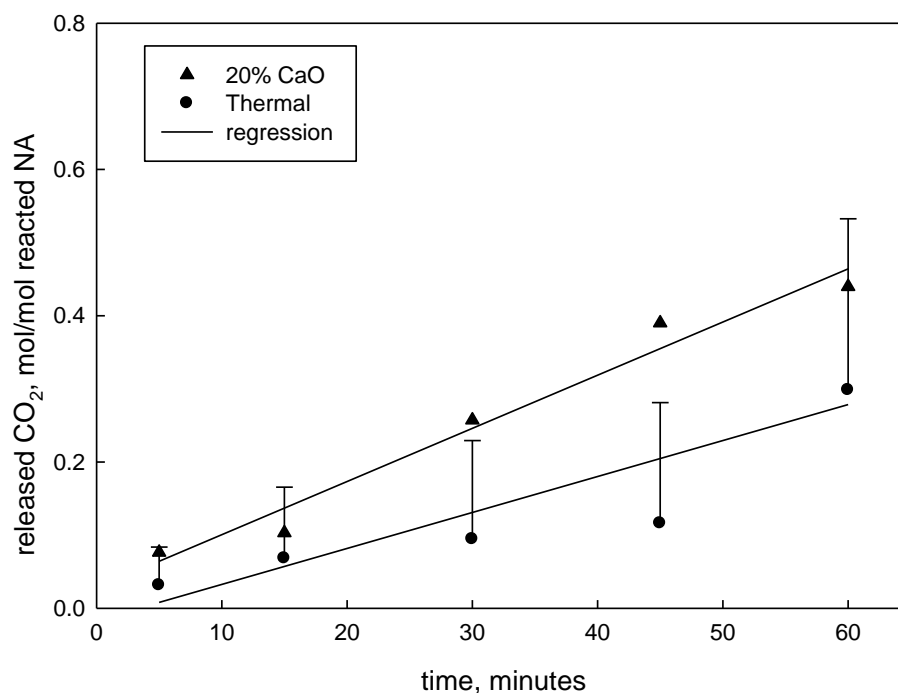


Figure 2-26 CO<sub>2</sub> Production at 365 °C against time for the carrier oil mixtures with initial TAN of 8.5 without and with addition of 20 wt% of CaO. Error bars show 2 times the standard deviation of experiments.

The data shown in Figure 2-26 represent CO<sub>2</sub> production at 365 °C against the reaction time for the carrier oil mixtures with initial TAN of 8.5 with and without addition of CaO, respectively. The CO<sub>2</sub> production was represented by the molar ratio of the released CO<sub>2</sub> to the reacted NA. The regression lines are only for the isothermal period after 5 minutes heating-up. The more NA was removed, the more CO<sub>2</sub> was produced. It is evident that the slope of the regression line shown in Figure 2-26 for the catalytic reaction is steeper than that of the thermal reaction, which means the production rate of CO<sub>2</sub> in the catalytic reaction is much higher than that in the thermal reaction.

#### **2.4.6.1 Influence of Initial TAN**

To study the influence of the TAN of oil mixtures on the TAN reduction rate, oil mixtures with three different initial TAN were tested in the reactions. Figure 2-27 and 28 show TAN reduction and CO<sub>2</sub> production at 365 °C against time for three mixtures with different initial TAN in presence of 20 wt% of CaO, respectively. The regression lines in Figures are only for the isothermal period after 5 minutes heating-up.

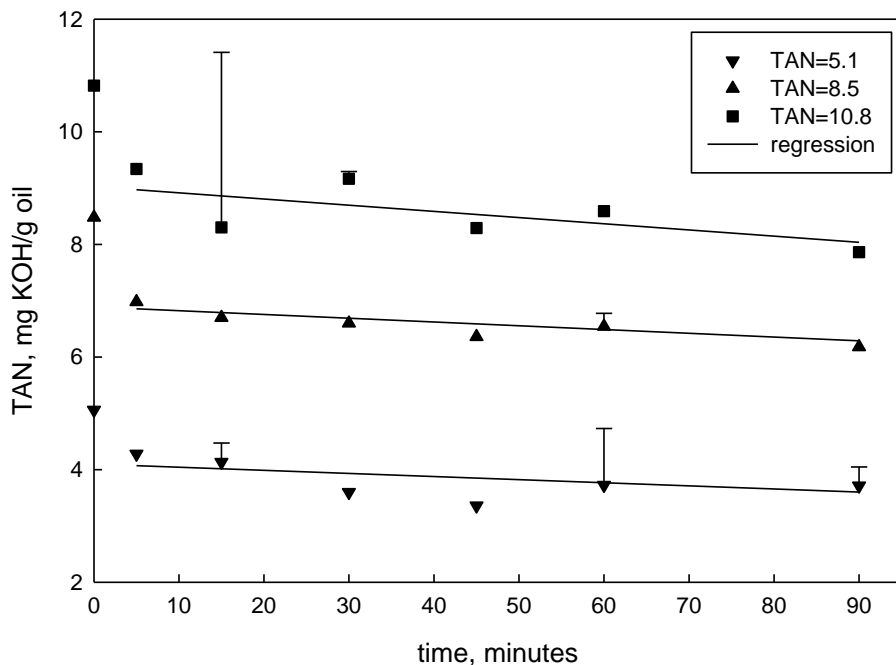


Figure 2-27 Reduction of TAN at 365 °C against time for three carrier oil mixtures with different initial TAN in presence of 20 wt% of CaO. Error bars show 2 times the standard deviation of experiments

As shown in Figure 2-27, the TAN of the oil mixture decreased linearly against the reaction time, and the regression lines of three series of data points with different initial TAN were parallel, indicating that the slopes of the lines are similar, which provided the evidence that the TAN of oil mixtures with different initial TANs decreased in the same trend with time, and the concentration of NA had no influence on the removal rate of NA. Therefore, the TAN reduction followed zero-order kinetics in the concentration of naphthenic acid in carrier oil. For the value of the rate constant at 365 °C, the slopes of three regression lines shown in Figure 2-27 were averaged because the rate constant is only the function of the reaction temperature.

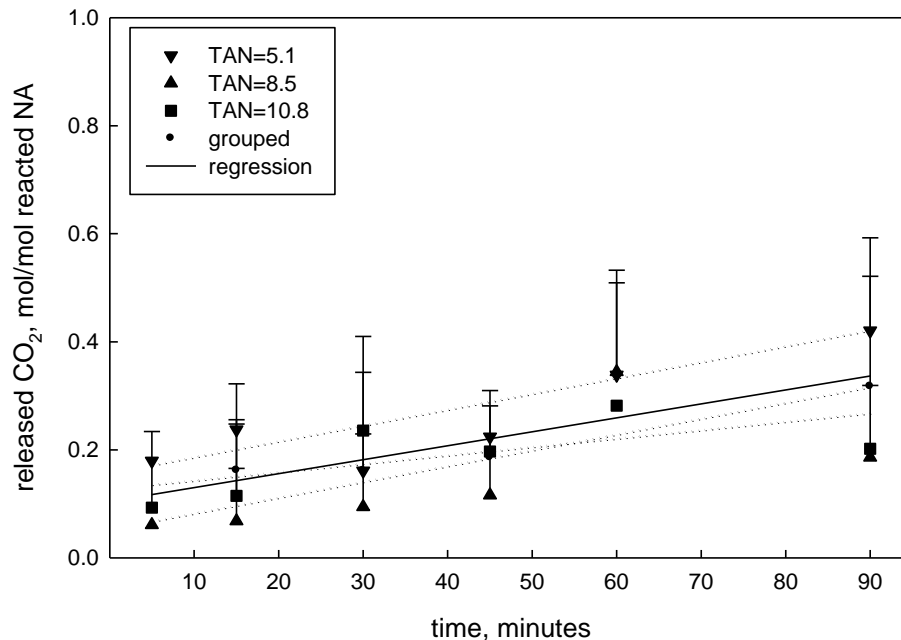


Figure 2-28 CO<sub>2</sub> production at 365 °C against time for three carrier oil mixtures with different initial TAN in presence of 20 wt% of CaO. Error bars show 2 times the standard deviation of experiments

The dotted lines in Figure 2-28 shows CO<sub>2</sub> production at 365 °C against time for three carrier oil mixtures with different initial TAN in presence of 20 wt% of CaO. It was found that CO<sub>2</sub> production increased linearly against the reaction time for all the carrier oil mixtures with different initial TAN, which demonstrates the production rate of CO<sub>2</sub> is also independent of the concentration of NA in carrier oil. The three dotted lines are not strictly parallel because of experimental errors. The three sets of experimental data corresponding to three carrier oil mixtures with different initial TAN were grouped together and replotted (the solid line in Figure 2-28). The slope of the solid line is the rate constant  $k$  which is only the function of the temperature.

The same trends as the previous were observed that the TAN of oil mixtures have no influence on the CO<sub>2</sub> production rate. Because the CO<sub>2</sub> production is an indication of the decarboxylation reaction, the conclusion can be drawn that the decarboxylation of NA is zero order in the concentration of NA in oil.

#### **2.4.6.2 Influence of Catalyst Loading**

To Study the influence of the catalyst loading on the TAN reduction and CO<sub>2</sub> production, the series of reactions with the double CaO loading were run with the initial TAN of 8.5 at three temperatures at 365, 375, and 385 °C. The only two points at 5 and 60 minutes were studied (Figures 2-29 and 30).

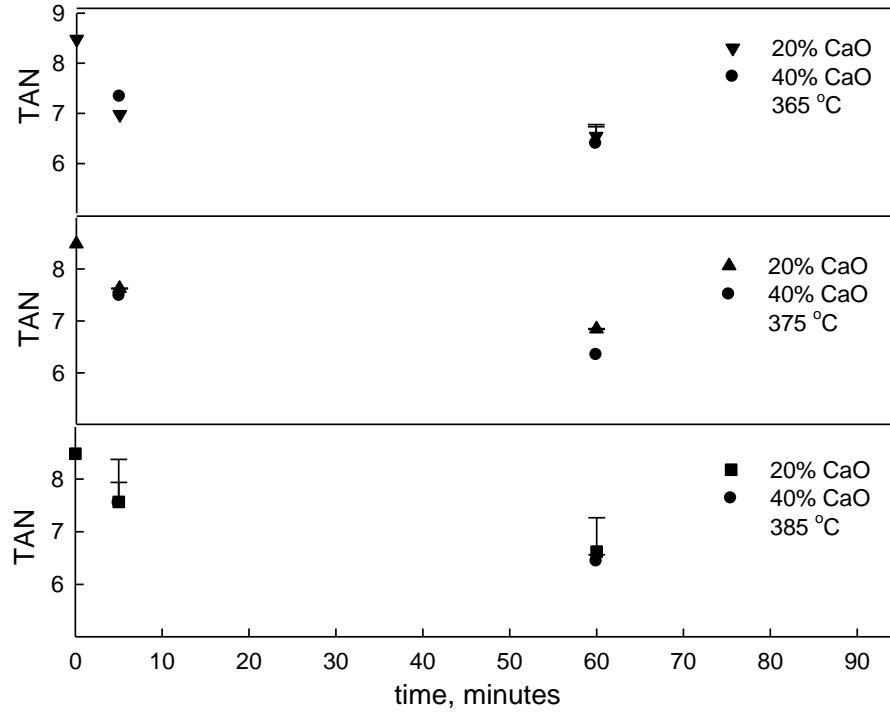


Figure 2-29 Reduction of TAN against time for three carrier oil mixtures with the same initial tan and different CaO loading at three different temperatures. Error bars show standard deviation of experiments

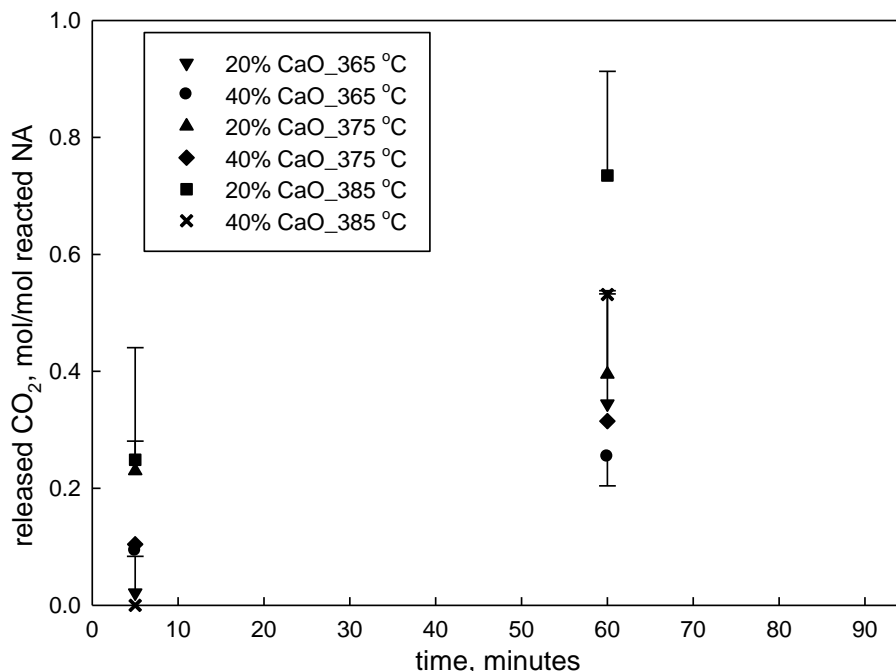


Figure 2-30 CO<sub>2</sub> Production against time for three carrier oil mixtures with the same initial TAN and different CaO loading at three different temperatures. Error bars show standard deviation of experiments

As data shown in Figure 2-29, TAN of the carrier oil mixture with double CaO loading decrease a little more than that with 20 wt% CaO loading, but the reduced amount is not twice, as was the catalyst loading. As shown in Figure 2-30, the more CaO was loaded, the less CO<sub>2</sub> was released.

### 2.4.6.3 Influence of Temperature

To study the influence of the temperature on the TAN reduction and CO<sub>2</sub> production rate, oil mixtures with the initial TAN of 8.5 were tested in the reactions at three different temperatures. Figure 2-31 and 32 show TAN

reduction and CO<sub>2</sub> production against time at different temperatures in presence of 20 wt% of CaO, respectively. The regression lines in Figures are only for the isothermal period after 5 minutes heating-up.

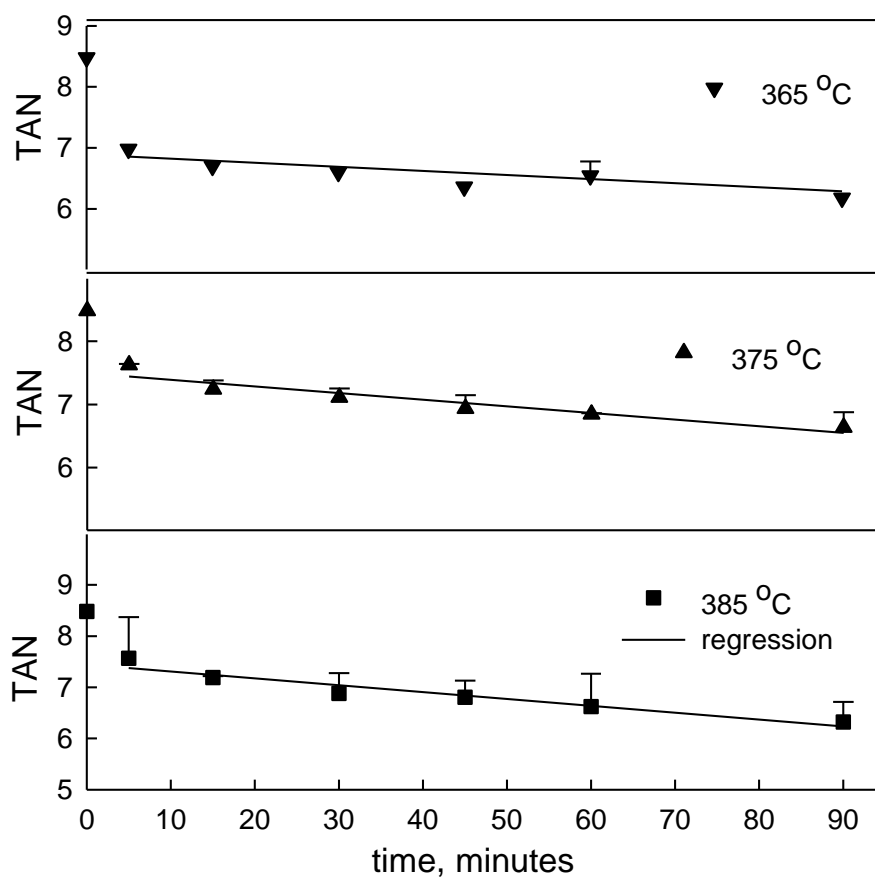


Figure 2-31 Reduction of TAN versus reaction time at different temperatures for three carrier oil mixtures with the same initial TAN in presence of 20 wt% of CaO. Error bars show standard deviation of experiments

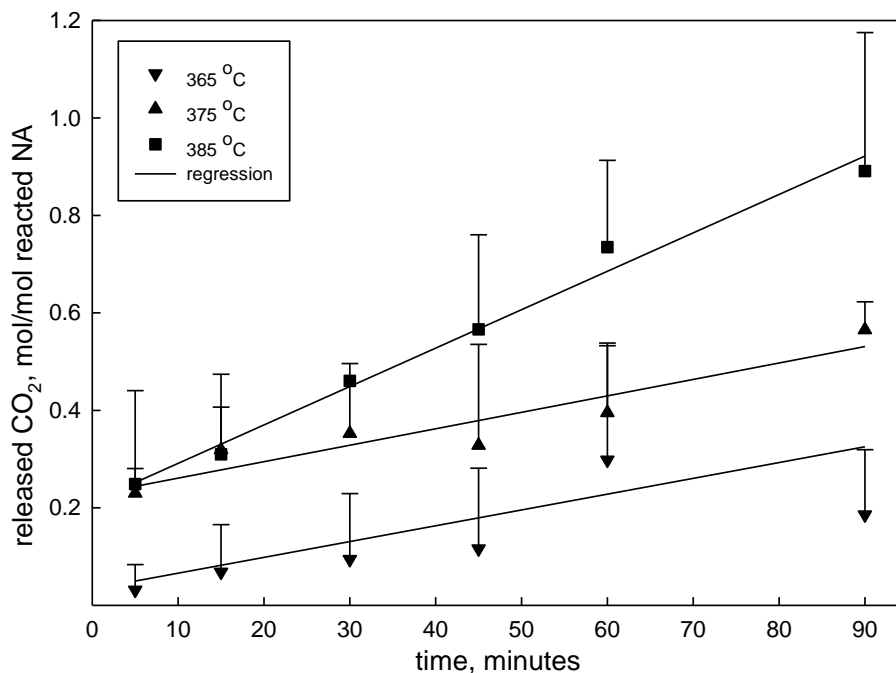


Figure 2- 32 CO<sub>2</sub> production versus reaction time at different temperature for three carrier oil mixtures with the same initial TAN in presence of 20 wt% of CaO. Error bars show 2 times the standard deviation of experiments

As shown in Figure 2-31 and 32, the higher the temperature was maintained, the slightly faster the TAN of the oil mixture decreased, and the faster the CO<sub>2</sub> was released. But it is also noted that TAN of the oil mixture at 365 °C was lower than those of the other two temperatures during most of the reaction. The reasons for such behavior were likely that the initial reaction of NA on the surface of catalyst was retarded when the temperature increased because of an exothermic adsorption. As the temperature of the system increases, adsorption equilibrium moves to the reactant side. But higher temperature was favorable for the decomposition of naphthenate to produce CO<sub>2</sub>, therefore, more CO<sub>2</sub> was released when the temperature increased from 365 to 385 °C. It was also

observed that temperature had a minor effect on the removal rate of NA, but had a great influence on the production rate of CO<sub>2</sub>.

#### 2.4.6.4 Activation Energy

According to the Arrhenius equation, the rate constant  $k$  conforms to the following equation:

$$k = Ae^{-E_a/RT} \quad (2-26)$$

where  $E_a$  is the overall activation energy, and  $T$  is the absolute temperature.

Taking natural logs of both sides,

$$\ln k = \ln A - \frac{E_a}{RT} \quad (2-27)$$

Plotting  $\ln k$  versus  $(1/T)$ , if straight line is obtained based on experimental data, the slope of the regression line equals to  $-E_a/R$ .

The rate constants of the TAN reduction and the CO<sub>2</sub> production rates can be obtained from the plotting of the molar concentration of naphthenic acid and CO<sub>2</sub> as a function of time, respectively. Since Figures 2-31 and 32 show the TAN (mg KOH/g oil) and CO<sub>2</sub> production in moles as a function of time, respectively, the unit conversion has to be performed to obtain the rate constants of the TAN reduction and the CO<sub>2</sub> production rates. It was assumed that the stoichiometry of potassium hydroxide and naphthenic acid is 1:1. Therefore, the TAN as a function of time can be used to represent the concentration change of naphthenic acid against the time. The calculation results were listed in Tables 2-16. Figures 2-33 and 34 show rate constant as a function of the reciprocal of the temperature.

Table 2-16 Calculation of Rate Constant of rates of TAN Reduction and CO<sub>2</sub> Production

T, °C	Slopes in Figure 2-33, mg KOH/g oil/minute	Rate constant, M s <sup>-1</sup>	Slopes in Figure 2-34, mol/minute	Rate constant, M s <sup>-1</sup>
365	-6.69E-3	3.40E-06	3.24E-03	1.54E-06
375	-0.0105	5.32E-06	3.34E-03	1.99E-06
385	-0.0134	6.83E-06	7.88E-03	5.84E-06

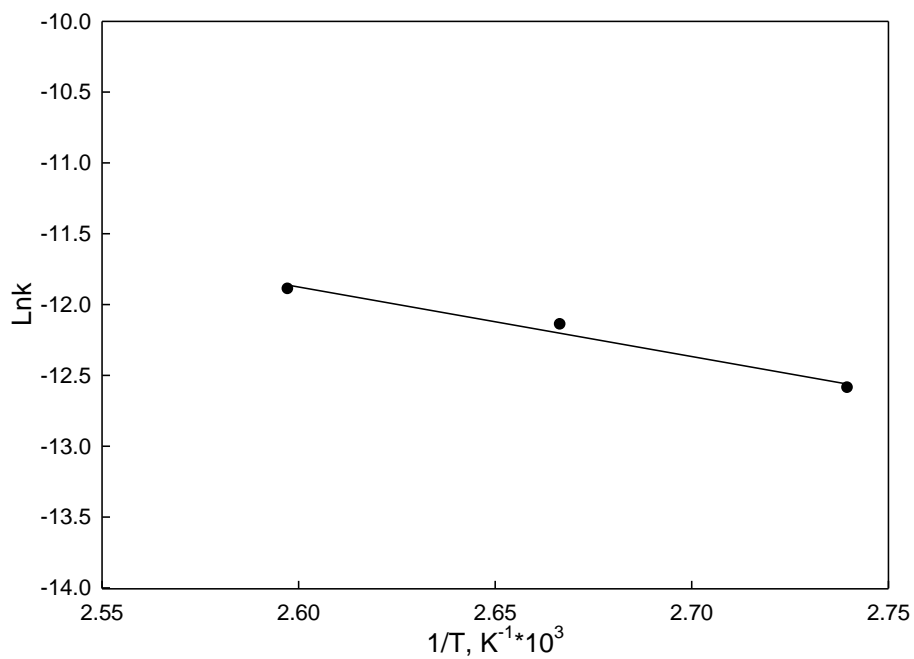


Figure 2-33 An Arrhenius Plot for the TAN Reduction Reaction

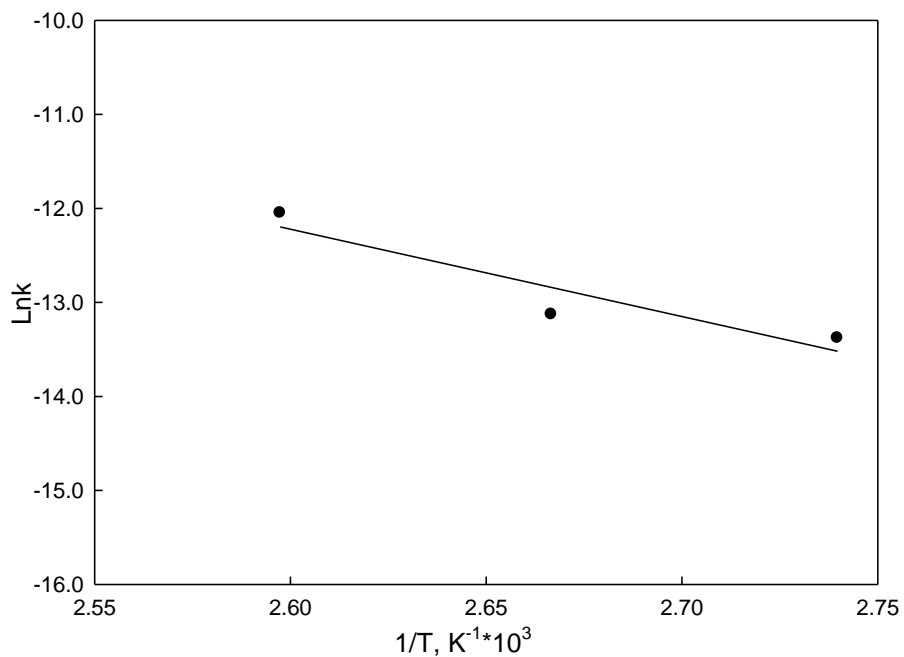


Figure 2-34 An Arrhenius Plot for the CO<sub>2</sub> Production Reaction

As shown in Figures 2-33 and 34, for the TAN reduction and CO<sub>2</sub> production, the same trends were found that natural log of rate constant is linear with the reciprocal of temperature. The activation energy can be obtained by calculating the slope of straight lines (Table 2-17)

Table 2-17 Overall Activation Energies of the Reactions of TAN Reduction and Decarboxylation of NA

	TAN reduction	CO <sub>2</sub> production
slope	-4912.9	-9295.5
Correlation coefficient, R <sup>2</sup>	0.98	0.88
Activation energy, kJ/mol	40.8	77.3
frequency factor, M s <sup>-1</sup>	2.45	1.54*10 <sup>5</sup>

#### **2.4.6.5 Kinetic reactions on Heavy Vacuum Gas Oil (HVGO)**

The kinetic reactions were performed on the HVGO to compare with the model compound described in the previous work. TAN of the HVGO is 5.2 mg KOH/g oil, which is quite similar to the lowest one tested in the previous study. In the experimental study on HVGO, the temperature of 365 °C was selected. The time series was still the same as before, 5, 15, 30, 45, 60, and 90 minutes. Two series of reactions were performed. One is for the thermal reaction (Figures 2-35 and 36), and the other is for the reaction with the addition of 20 wt% CaO (Figures 2-37 and 38). The kinetic data of carrier oil mixtures are also included for comparisons.

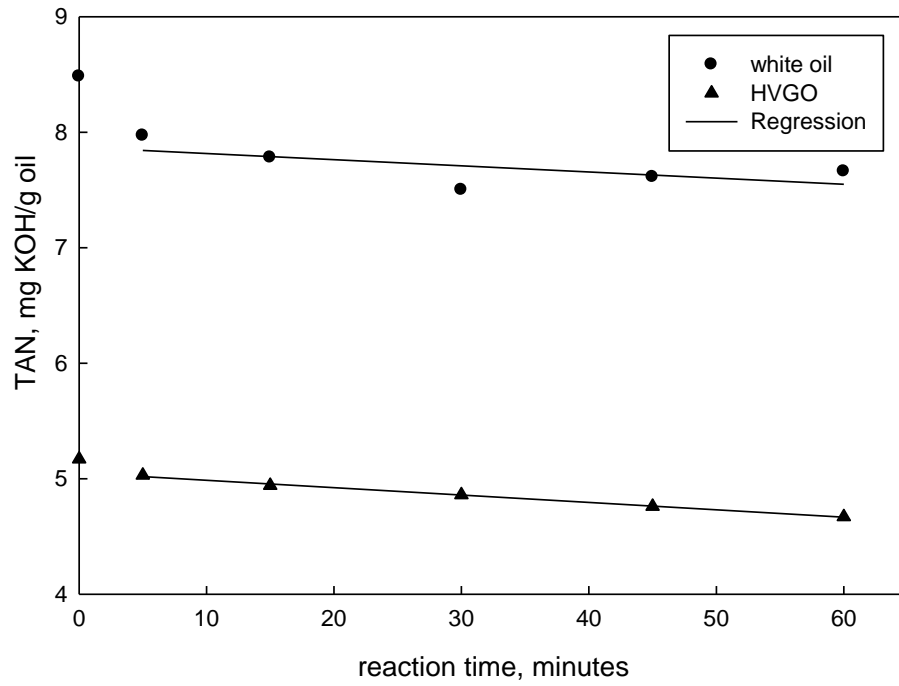


Figure 2-35 TAN reduction versus time for two oil samples with similar initial TAN in thermal reactions. The regression lines are only for the isothermal period after 5 minutes heating-up.

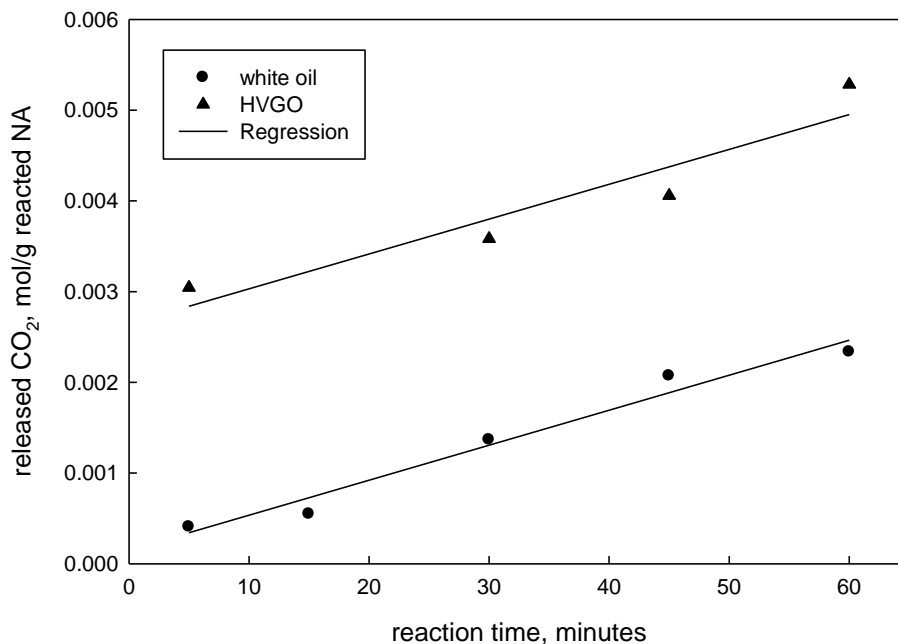


Figure 2-36 CO<sub>2</sub> production versus time for two oil samples with similar initial TAN in thermal reactions. The regression lines are only for the isothermal period after 5 minutes heating-up.

As data shown in Figure 2-35 and 36, two oil samples, carrier oil and HVGO, demonstrate similarity in the disappearance of TAN; the level in both oil samples decreased linearly at the same rate during the reaction process, and the released CO<sub>2</sub> in the vapor phase increased linearly against time in the reactions on both samples of the carrier oil and HVGO. TAN of the HVGO sample was reduced by about 17% during the reaction process.

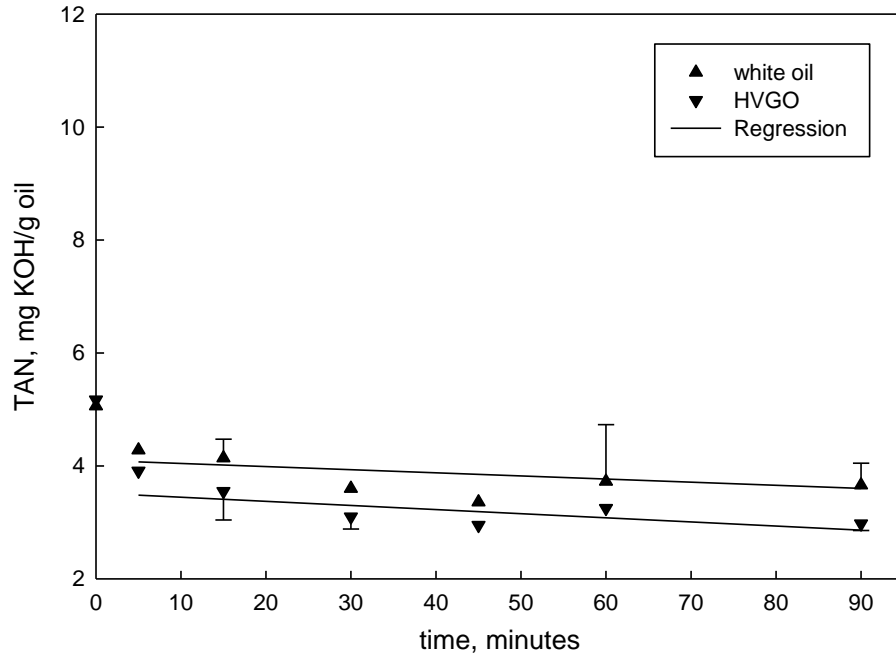


Figure 2-37 TAN reduction versus time for two oil samples with similar initial TAN in the presence of 20 wt% CaO. Error bars show 2 times the standard deviation of experiments

As shown in Figure 2-37, the regression lines of two series of reactions with different oil samples are in parallel, indicating the slopes of the lines are the same, which provided the evidence that TAN of two different oil mixtures decreased in the same trend with time, and the oil system had no influence on the removal rate of NA. The regression lines in the figure are only for the isothermal period after 5 minutes heating-up. Therefore, the actual gas oil, HVGO, exhibits the same trend as the model mixture, the removal rate of NA is the zero order in the concentration of NA. The rate constant can also be obtained by the slope of the regression lines.

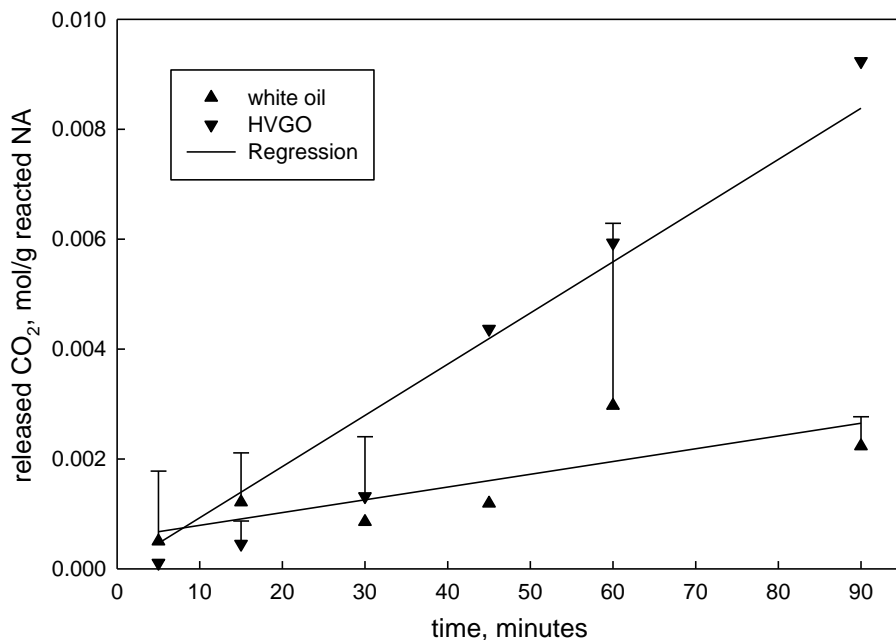


Figure 2-38 CO<sub>2</sub> production versus time for two oil samples with similar initial TAN in the presence of 20 wt% CaO. Error bars show 2 times the standard deviation of experiments

The same trends were observed that CO<sub>2</sub> in the vapor phase was accumulated linearly against time for both of the carrier oil and HVGO samples. However, it was found as well that CO<sub>2</sub> production in the HVGO is much faster than that in the carrier oil. The more NA was removed, the more CO<sub>2</sub> was produced. Therefore, the TAN of the HVGO has no influence on the CO<sub>2</sub> production rate, and the decarboxylation of NA in HVGO is a zero reaction in NA as well. The regression lines in Figure 2-38 are only for the isothermal period after 5 minutes heating-up.

#### 2.4.6.6 Analysis of Solid Samples after the Reaction

In previously sections, we elucidated TAN of carrier oil mixtures and CO<sub>2</sub> production in the gas phase as the function of time, and found that calcium naphthenate was formed on the surface of the catalyst. But it is still not clear how calcium naphthenate was formed and decomposed during the reaction process. To find the solution for this question, the spent catalysts after each reaction were collected and washed. Toluene and pentane were chosen as the washing solvents. To identify whether calcium naphthenate was washed out by the solvent, the washing residues were analyzed using FTIR (Figures 2-39 and 40). The IR spectra of pure solvent of toluene and pentane were also included for comparison.

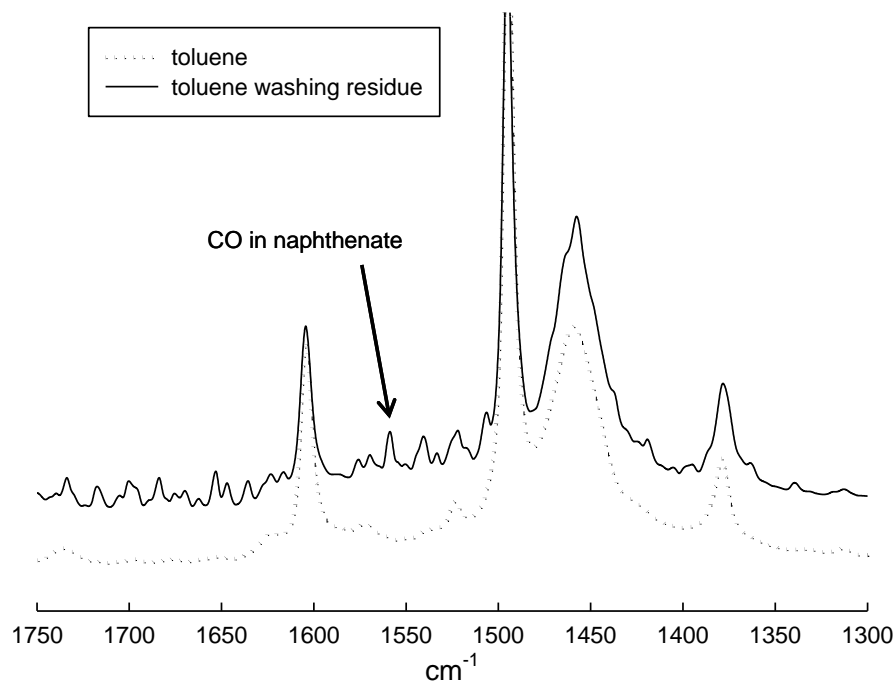


Figure 2-39 IR Spectra of Toluene Washing Residue

As spectra shown in Figure 2-39, the peak corresponding to carbonyl group around  $1560\text{ cm}^{-1}$  in calcium naphthenate was found in IR spectra of the toluene washing residue of the post-reacted CaO (the initial TAN=8.5,  $T=365\text{ }^{\circ}\text{C}$ , and  $t=60$  minutes), which demonstrates that calcium naphthenate is soluble in toluene. Therefore, toluene cannot be used as the washing solvent to prepare the solid sample for quantitative analysis.

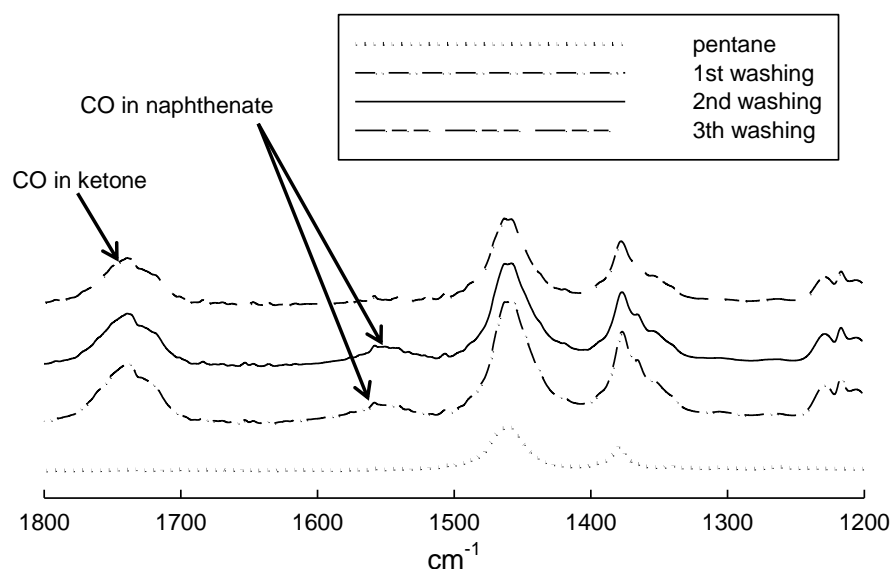


Figure 2-40 IR Spectra of Pentane Washing Residue

When pentane was used as a washing solvent, the post-reacted CaO (the initial TAN=10.8,  $T=365\text{ }^{\circ}\text{C}$ , and  $t=60$  minutes) was washed three times, the washing residues were analyzed by using FTIR. As shown in Figure 2-40, peaks corresponding to carbonyl group of calcium naphthenate were found in IR spectra of the first and second washing residues. There is no obvious IR adsorption of the carbonyl group found in the third washing residue. Therefore,

the calcium naphthenate is weakly soluble in pentane. Figure 2-41 shows IR spectra of the post-reacted CaO after the toluene or pentane washings.

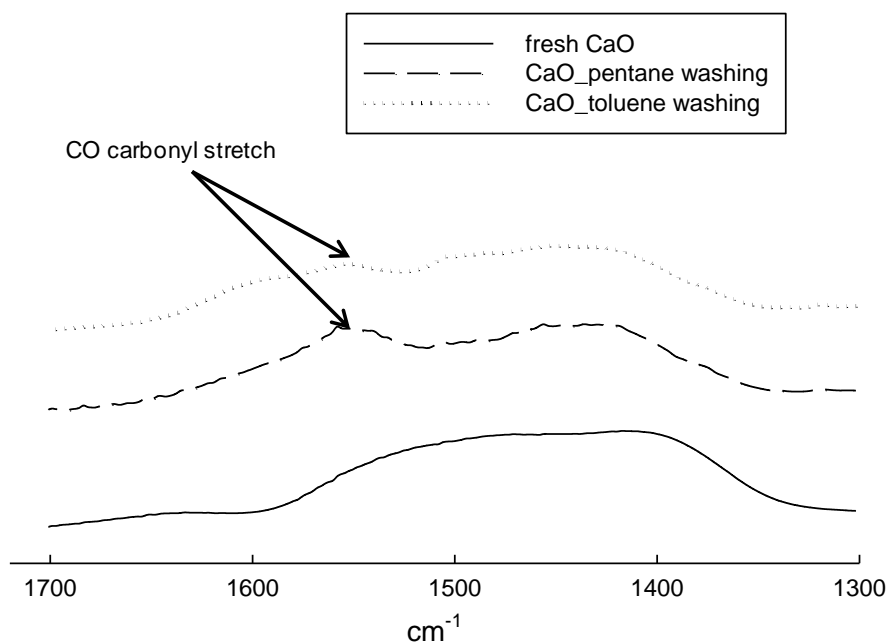


Figure 2-41 IR Spectra of CaO after Toluene/Pentane Washing

As shown in Figure 2-41, peaks associating with carbonyl group in calcium naphthenate were found in IR spectra of both post-reacted catalyst after the solvent washing. The peak of carbonyl in the pentane washed sample is much better separated than that of the toluene washed sample, and the peak area of the former is also bigger than the latter, nevertheless the peak area cannot be determined quantitatively.

#### **2.4.6.7 Reaction in an impeller-mixed batch reactor**

The data of Figure 2-27 and 2-31 show an initial very rapid rate of reaction, followed by low rates of reaction of the acids. The solid particles of calcium oxide had little internal porosity, therefore, the diffusion of the acids to the particle surfaces from the bulk liquid phase would not be rate limiting. The penetration of reactants through a layer of calcium naphthenate intermediate could, however, be a very significant rate limitation.

Given the evidence that the calcium reaction intermediates were at least partly soluble at the reaction conditions, we tested the role of agitation to determine the benefits of significant agitation in removing calcium naphthenate from the calcium particles. A Parr autoclave was used with an agitator operating at about 60 rpm (See Appendix C for the reaction of the model system in a Parr reactor). In comparison, the agitation of the batch reactors at circa 1 Hz would give more gentle mixing of solids and liquids. Figure 2-42 shows the TAN reduction against time in the stirred reactor.

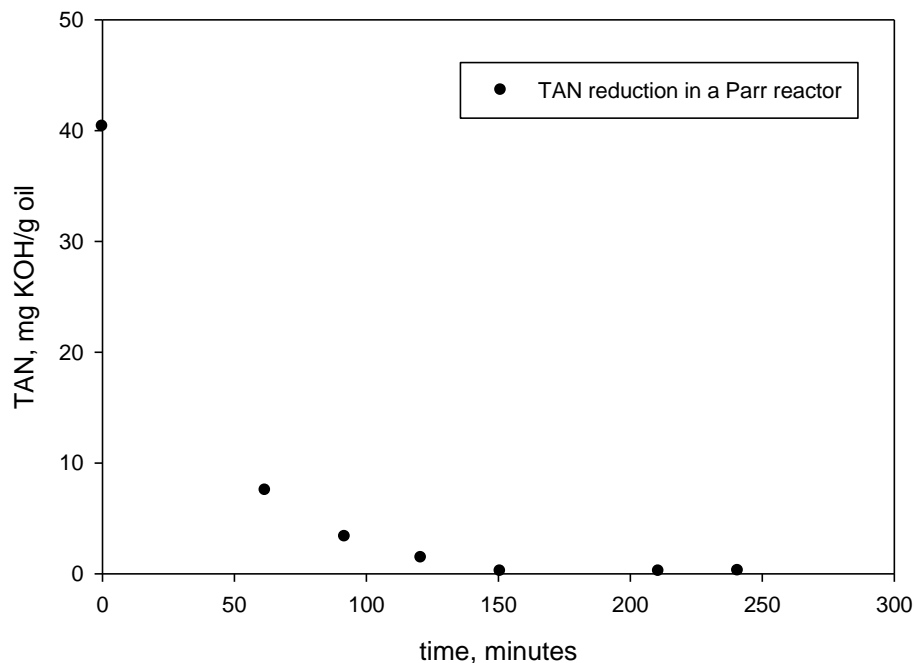


Figure 2- 42 Reduction of TAN versus reaction time at 385 °C in the Parr reactor for a carrier oil mixture with initial TAN of 40.4 in presence of 30 wt% of CaO (the reactor took one hour to reach 385 °C from the ambient temperature)

As shown in Figure 2-42, the TAN of the mixture of NA and carrier decreased from 40.4 to 3.3 over a heating-up period of 90 minutes in the stirred reactor, and 96.4% of NA was removed within 120 minutes. The heating rate of this reactor is slow, so that in the 60 minutes required to reach reaction temperature, the conversion was circa 80%. These data confirmed that agitation could drive the reaction to completion, but even under these conditions the reaction was relatively slow.

## 2.5 Discussion

### 2.5.1 Error Analysis

As data shown in Table 2-11, the mean is 6.51 mg KOH/g oil, the standard deviation is  $\pm 0.14$ , 95% confidence intervals is [4.54, 6.60]. The average error in TAN measurements was 0.51%, and the maximum error was 1.34%. Therefore, our 9 TAN measurements gave us the evidence to claim that the data of TAN measured by using the automatic titrator are reliable to within [6.23, 6.60].

To detect whether some data above are spurious and need to be discarded, the interquartile range method (Scheaffer and McClave 1995), or IQR, was used for detecting an outlier, which depends on the quartiles and the difference between the quartiles. The analysis results show that the value of 6.23 for TAN measurement is out of the IQR of 6.30 to 6.78, and no data point for CO<sub>2</sub> concentration is out of the IQR. Because 6.23 is not much less than the lower limit of the IQR of TAN measures, and CO<sub>2</sub> concentration at the same run is still acceptable, the data point of 6.23 was not rejected. The average and standard deviation were calculated based on all data points (Table 2-12). As data shown in Table 2-12, for the data set of CO<sub>2</sub> concentration, the standard deviation of the mean was much higher than the TAN determinations. The reason for this behavior is that little of CO<sub>2</sub> was produced and released during the reaction process due to the low reaction temperature. Therefore, it is very difficult to more accurately quantify CO<sub>2</sub> in the vapor phase by using GC.

### 2.5.2 Characterization of Naphthenic Acid

For NA characterization, the GC-MS analysis and subsequent data handling yields a large amount of numerical information about the NA composition, such as the carbon number and Z families (see Table 2-10). The results of the GC-MS analysis show that the most abundant components in the NA sample used in this work has carbon numbers of 10, 11, and 12, and are in the Z family of 2, with the percentages of 8, 17 and 13, respectively. The average molecular weight based on MS-GC analysis was calculated to be 188.34 g/mol.

Although carbon number  $n$  and Z can be obtained through GC-MS analysis, isomeric compounds are still unable to be individually determined in each isomer class because of the limitation of GC-EIMS regarding the isomeric compound identification. Moreover, there is no an effective method to extract NA completely from the oil mixture. Therefore, it is impossible to identify individual compounds of NA in oil mixture and trace their concentration change individually before and after the reaction only with analysis of GC-MS. In other words, it is unlikely to verify whether the conversion of NA is selective for individual components. Given our interest in conversion of naphthenic acids in dilute solution, as in crude oils, we did not attempt further studies by GC-MS of the selective conversion of different components in the complex mixture of naphthenic acids.

### 2.5.3 Catalyst Screening Based on IR Analysis and TAN Measurement

Through analyses of liquid samples before and after the reaction without and with addition of catalysts using IR and TAN measurement, the effect of the catalyst on the NA removal was studied. As data shown in Figure 2-13, compared with the thermal reaction, all the tested catalysts demonstrated the activity on the NA removal. Among the tested catalysts, the catalyst  $\text{CaCO}_3$  is the least active in converting NA into other neutral compounds, and IR analysis showed that only 20% of NA in the oil mixture was removed, a little lower than 26% obtained by TAN measures. The catalyst  $\text{Li}_2\text{O}$  reveals the highest activity. The IR analysis and TAN measurement showed 66% and 74% of NA were removed from the oil mixture, respectively. The catalyst  $\text{CaO}$  also exhibited the high reactivity, 65% of NA was removed from the oil mixture during the reaction process in presence of  $\text{CaO}$ . Although IR analysis and TAN measurement gave the different value for the acid conversion as shown in Figure 2-13 on account of the different techniques applied in each analytic method, the same trends were found in decreases of NA of oil mixtures with addition of different catalysts. The trend in decrease of NA was  $\text{Li}_2\text{O} > \text{CaO} > \text{BaO} > \text{MgO} > \text{CaCO}_3$ .

Based on the analyses of the particle sizes of the solid materials, it was found that the specific surface areas of the tested materials decreases in the order of  $\text{MgO} > \text{CaO} > \text{Li}_2\text{O} > \text{CaCO}_3 > \text{BaO}$ , which is not synchronous to the activities of the corresponding tested catalysts. Therefore, the surface area of the material was not the only dominant factor of the activity of the catalyst. Considering the hypothesis that the metal salt was an intermediate product during the reaction

process, the basicity of the catalyst may play an important role in the reaction of decarboxylation.

For the metals in the same group, for example IIA group, the metal hydroxides become more basic down the group with increasing metal character of the element ( $\text{Ba}(\text{OH})_2 > \text{Ca}(\text{OH})_2 > \text{Mg}(\text{OH})_2$ ) (Atkins et al. 2006). Based on the evidence that the member of IA group is more basic than that of the IIA group at the same period, and the atomic radii of the two elements are similar, it is deduced that the basicity of  $\text{LiOH}$  is higher than that of  $\text{Mg}(\text{OH})_2$  but less than that of  $\text{Ca}(\text{OH})_2$ . Therefore, the basicities of the tested catalysts decreases in the order of  $\text{Ba}(\text{OH})_2 > \text{Ca}(\text{OH})_2 > \text{LiOH} > \text{Mg}(\text{OH})_2 > \text{CaCO}_3$  which is different from the order of the activity of the tested catalysts as well. Therefore, the activities of the tested catalysts can not be explained only by the basicity of the corresponding materials.

In the reaction of decarboxylation of NA, water is one of the main products which will react with a metal oxide to form a hydroxide, and the hydroxide will then react with NA to form an intermediate product, naphthenate salt. Therefore, the faster the intermediate decomposes, the faster the catalyst is recovered, and the more NA can be removed. The ease of the decomposition is dependent of the thermal stability of the salt. Because there are not too many data reported on the decomposition temperature of naphthenate of alkali and alkaline metals, we collected the decomposition data of the corresponding metal carbonates to analyze the stability of the naphthenate salts. We assume that both carbonates and naphthenates of alkali and alkaline metals possess the similar

trend on the stability (Kim and Lee 2001). Table 2-19 lists the decomposition temperatures of IIA group metal carbonates (Shriver et al. 1994).

Table 2-18 Decomposition Data on Carbonates

	Mg	Ca	Ba
$\Delta G^\circ / (\text{kJ mol}^{-1})$	48.3	130.4	218.1
$\Delta H^\circ / (\text{kJ mol}^{-1})$	100.6	178.3	269.3
$\Delta S^\circ / (\text{J K}^{-1} \text{ mol}^{-1})$	175.0	160.6	172.1
T/ °C	300	840	1300

Note: T is the temperature required to reach 1 bar of CO<sub>2</sub>, and has been estimated from the 298 K reaction enthalpy and entropy.

As data shown in Table 2-19, when going down the IIA group, the carbonates become more thermally stable, hence, higher temperature is needed to make BaCO<sub>3</sub> decompose than MgCO<sub>3</sub>. In general, there is the relationship between the reaction enthalpy and the decomposition temperature that the higher the reaction enthalpy is, the higher the decomposition temperature is. The enthalpy of decomposition is partly dependent on the difference between the lattice energies of the decomposition product (MO) and the reactant (MCO<sub>3</sub>). The overall reaction enthalpy is positive because decomposition is endothermic, and the enthalpy value is less strongly positive if the lattice energy of the decomposition product MO is higher than that of the parent MCO<sub>3</sub>. Therefore, the decomposition temperature will be low for the product of oxide whose lattice energy is remarkable higher than that of carbonate. For example, for decompositions of CaCO<sub>3</sub> and BaCO<sub>3</sub>, the lattice energies of the products (CaO

and BaO) are 3489 and 3088 kJ/mol, respectively and the lattice energies of the corresponding carbonates are 2921 and 2431 kJ/mol, respectively (Croix et al. 1998), CaO has higher lattice energy than that of BaO, and the decomposition temperature is lower than that of BaO. The difference in lattice energy between MO and MCO<sub>3</sub> becomes significant by a large charge number of the cation; as a result, the decomposition of the carbonate takes place at the low temperature if it contains a highly charged cation. Therefore, the decomposition temperatures of alkaline earth metal carbonates are lower than that of alkali metal carbonates at the same period. Kim et al. reported that Li<sub>2</sub>CO<sub>3</sub> starts to decompose when the temperature reaches 760 °C. In summary, the decomposition temperatures of the carbonates increase in the order of MgCO<sub>3</sub><Li<sub>2</sub>CO<sub>3</sub><CaCO<sub>3</sub><BaCO<sub>3</sub>.. Therefore, we believe that magnesium naphthenate decompose at the lowest temperature, while barium naphthenate needs to be heated at very high temperature to decompose.

Among all these factors discussed above, there is not any single factor that correlates with the activity of the catalyst. Each factor may play a part in the reactivity of the catalyst. For example, for MgO, its activity ranks the fourth among all of the tested materials although it has the lowest decomposition temperature; its activity is counteracted by the lower surface area and the lowest basicity. Therefore, the reactivity of a catalyst is likely determined by the overall effect of surface area, basicity, and thermal stability of the naphthenate intermediate.

#### **2.5.4 Evidences of the Formation of Naphthenate Salts in Solid Samples**

Guarino (Guarino 2006) observed that the percentage of butyric acid consumed appeared to be steady after a certain period of time, while the production of 4-heptanone and acetone was observed to increase continuously with time. The reason of such observation is butyric acid reacted with the test catalyst to form a carboxylate salt, which then decomposed to generate the ketone as products. Based on her observation, the solid samples in our work were analyzed by FTIR and TGA to detect naphthenate salt formed during the reaction process.

The reaction was run initially in which oil mixtures contained very low TAN of 3 and 10 wt% of CaO was introduced in the reactor. The spent solid sample was analyzed by FTIR, and the fresh CaO was also analyzed for comparison. As data shown in Figures 2-19, no peak corresponding to carbonyl group in calcium naphthenate was found. Two explanations for the lack of a carbonyl peak were possible. One is that no calcium naphthenate was indeed formed in the reaction, and the other is that the produced calcium naphthenate could not be detected because of its low concentration. A new reaction was rerun to verify the explanations in which TAN of the oil mixture was increased from 3 to 45, and the catalyst loading was cut down from 10 to 4 wt%. The spectra exhibited the sharp peak associated with carbonyl group in the carboxylate salt (see Figure 2-20). The different behaviors between two analyses can be explained by reasons that the initial TAN of the oil mixture was low in the first reaction, thus the total amount of naphthenate salt was much little in the loaded

solid. As a consequence, the concentration of naphthenate was so low that the carbonyl group could not be identified by IR. By contrast, carbonyl group in the solid sample with high initial TAN loading was found by using IR analysis because of the higher initial TAN of the oil mixture and lower amount of catalyst loaded. The TGA results in Figure 2-22 demonstrate the presence of calcium naphthenate in both of the solid samples from the reactions with the different initial TAN and catalyst loadings.

### **2.5.5 Evidence of Decarboxylation of NA in the Liquid Phase**

In the decarboxylation reaction of NA, CO<sub>2</sub> and H<sub>2</sub>O are two major products. If CO<sub>2</sub> can be found in the gas phase in the reactor, and H<sub>2</sub>O is found in oil mixtures or post-reacted catalysts, then NA removal of the oil mixture can be attributed to the catalytic decarboxylation.

As described previously, gas samples after the reaction were collected and injected in the GC. CO<sub>2</sub> were detected in all of the tested gas samples, which proved the occurrence of decarboxylation of NA in the liquid phase. Moreover, SEM images and XRD patterns of post-reacted catalysts provide the further evidence of the decarboxylation of NA. As SEM images shown in Figures 2-14, 15, and 16, the significant differences in the morphology of the solid samples before and after the reaction were observed. The post-reacted catalyst made a complete change in the morphology. The plate-like and irregular sheet-shape particles became the dominant in the post-reacted material by contrast with the thin petal-like thin films in the starting material. The comparison between SEM

images before and after the reaction revealed that new compounds with the different structures were formed during the reaction. XRD tests shown in Figure 2-17 further confirmed the formation of the new compounds, calcium hydroxide, which also proved indirectly the formation of water during the reaction process. The formed water likely reacted with calcium oxide to produce calcium hydroxide.

Therefore, all the evidence from GC, SEM, and XRD substantiated the occurrence of decarboxylation of NA in oil mixtures.

#### **2.5.6 Solubility of Calcium Naphthenate in the Oil**

As data shown in Tables 2-14 and 2-15, elements of Al, Ca, and Si are found in both solid mixtures of CaO and kaolin clay before and after the reaction, and the element of Mg is only found in the post-reacted sample. Because the reactants are free of the element of magnesium, the element of Mg might come from the impurity on the wall of the reactor. The AES spectra of the solid samples before and after the reaction show that both samples contain elements Ca, C, and O, moreover, elements of Al, Si, and Fe are only found in the fresh mixture of CaO and kaolin clay. Although kaolin clay might contain all of these three elements, the iron was not observed by using EDX. Therefore, iron is not the actual element of the solid sample, and it comes from the sampling disc as a stainless steel disc was used as the sample container during AES analysis. What happened with elements of Al and Si? Why they are only found in the fresh mixture of CaO and kaolin clay but not found in the post-reacted sample with the

same analytical technique? The reason for this observation is that the post-reacted particles were coated by other materials without the elements of Al and Si. The intermediate product calcium naphthenate is likely at least partly soluble in the oil at the reaction temperature, and its solubility in oil would decrease as the temperature decreased. Therefore, when the reaction system cools down, the soluble calcium naphthenate in oil precipitates and deposits on the solid particles, and creates a thin coating on each solid particle which consists of elements of Ca, C, H, and O. Because EDX can measure the region of about 2 microns deep from the surface, the elements under the thin coating are observable. For AES technique, Auger electrons can only escape from the outer 5-50 Å of a solid surface at their characteristic energy, therefore, the AES spectra of the post-reacted solid sample show the elemental compositions of calcium naphthenate coating rather than that of the actual mixture of CaO and kaolin clay.

### **2.5.7 Kinetics of Catalytic Decarboxylation of NA in Oil**

Although a great number of studies have been conducted on the catalytic decarboxylation of carboxylic acid, there is lack of data relevant to reactions of acids in dilute solutions of hydrocarbon. Therefore, the decarboxylation reaction of NA in a dilute oil medium was studied experimentally in our work. A series of the thermal reactions were performed firstly to study the thermal decarboxylation reaction of NA. The data in Figures 2-24 and 25 demonstrate the occurrence of the thermal decarboxylation as CO<sub>2</sub> was detected in all the gas samples collected at different reaction times, even only heating-up for 5 minutes. TAN of the oil

mixtures decreased by 11.1% after 60 minutes. Fuson (Fuson 1966) proposed the mechanism of the thermal decarboxylation reaction without the addition of the catalyst, in which it was believed that ketones are formed from acids by way of anhydrides, then the anhydride is rearranged to the  $\beta$ -keto acid, the next is followed by decarboxylation of the  $\beta$ -keto acid. The mechanism seems likely because the  $\alpha$ -hydrogen atoms are less stable in anhydrides than in acids, the rearrangement of the anhydride to the  $\beta$ -keto acid would be plausible. Under the same reaction conditions, the catalyst of CaO was introduced in the reactor, the series of reactions were performed for comparison, the results indicate that TAN of oil mixtures were reduced by 25.7% in the presence of the catalyst, which is more than that of no catalyst loaded. The reason for the higher reduction of TAN with addition of CaO is that NA in oil mixtures was converted to the naphthenate salt.

Kinetic information on the decarboxylation of NA was obtained by varying the initial TAN of oil mixtures during one of the reaction series, and then varying the reaction temperatures during the other of the reaction series. The effects of TAN and temperature on the decarboxylation reaction of NA were elucidated in detail as follows:

#### **2.5.7.1 Influence of TAN of oil mixtures**

Three series of reactions were run to study the effect of TAN of the oil mixtures on the reactions of NA removal and decarboxylation. It is important to note that the NA removed from the oil mixture was not totally decarboxylated to

release CO<sub>2</sub>, some NA was converted to the naphthenate and presented partially in the solid phase and partially dissolved in oil. Therefore, the reactions of NA conversion and decarboxylation were discussed separately. Figure 2-27 shows TAN of oil mixtures as a function of the reaction time at 365 °C. As the data show, TAN of oil mixtures decreased in the same trend with time for all three series of reactions no matter how different the initial TAN of the oil mixtures were. Within the range of the reaction time, TAN of three oil mixtures with different TAN decreased linearly at the same rate.

According to law of mass action,

$$-\frac{dC_A}{dt} = kC_A^a \quad (2-28)$$

Where  $a$  is the reaction order in  $C_A$ . Only when  $a=0$ , the reaction rate is independent of the concentration of the component A, and only the function of the rate constant. If plotting the concentration of the component A against the time, a straight line will be obtained, and the slope of the linear line is the negative value of the rate constant. Hence, the conclusion can be drawn that the overall rate of the NA removal is zero order in NA based on the observation of the experiments. Concerning the value of the rate constant at 365 °C, the slopes of three regression lines shown in Figure 2-27 were averaged because the rate constant is a constant at the certain temperature, which is also the reason for the parallel regression lines observed.

Since the quantitatively measurable CO<sub>2</sub> is one of products of the decarboxylation reaction, the production rate of CO<sub>2</sub> was selected to represent the rate of decarboxylation reaction of NA. As data shown in Figure 2-28, the

moles of the released CO<sub>2</sub> increased linearly against time for all three series of reactions with different initial TAN of oil mixtures. Therefore, CO<sub>2</sub> production was independent of the NA concentration, and the production rate of CO<sub>2</sub> was zero order in the NA concentration as well. The rate constant was calculated by averaging slopes of three linear regression lines because the slopes were not significantly different.

#### **2.5.7.2 Influence of Temperature**

Three series of reactions were run at the three temperatures of 365, 375, and 385 °C, respectively. Figure 2-31 shows TAN of oil mixtures as a function of the reaction time at different temperatures. As data shown, TAN of oil mixtures decreased in the same trend with time for all three series of reactions. Within the range of the reaction time, TAN of three oil mixtures with the same initial TAN decreased linearly. The higher the temperature applied, the faster the TAN of the oil mixture decreased. The same behaviors were observed for the CO<sub>2</sub> production at the different temperatures that the moles of the released CO<sub>2</sub> increased linearly against time, and the production rate of CO<sub>2</sub> became faster with the temperature increasing.

It is noted that the most NA was removed and the least CO<sub>2</sub> was released at 365 °C during the most reaction period comparing with those at 375 and 385 °C. The reason for such reverse behaviors was likely that the initial reaction of NA on the surface of catalyst was retarded when the temperature increased because of an exothermic adsorption, but higher temperature was favorable for

the decomposition of naphthenate to produce CO<sub>2</sub>, therefore, more CO<sub>2</sub> was released when the temperature increased from 365 to 385 °C.

The overall activation energies of the NA removal and CO<sub>2</sub> production were obtained based on the Arrhenius equation. The high overall activation energy of the CO<sub>2</sub> production reaction provides evidence to support the hypothesis that the decomposition of the intermediate product, naphthenate salt, is a rate-controlling step.

### **2.5.7.3 Kinetic Reactions of HVGO**

The actual gas oil, HVGO, was also tested to compare with the model mixture used in the previous work (Figures 2-37 and 2-38). Based on the experimental data, HVGO exhibited the similarity to the model mixture regarding the kinetics of the NA decarboxylation reaction. The kinetics of the TAN reduction reaction and NA decarboxylation reaction followed the zero-order with respect to the concentration of NA in oil mixtures. As data shown in Figure 2-37, the concentration of NA in HVGO became lower than that in carrier oil once the reaction started although the initial TANs of two solutions were the same. The reason could be that calcium naphthenates formed was more soluble in HVGO than in carrier oil. The slopes of the regressions are listed in Table 2-20.

Table 2-19 the Slope of the Regression Lines of TAN Reduction and CO<sub>2</sub> Production rate

365 °C	Slope of TAN reduction, mg KOH/g oil/minute	CO <sub>2</sub> Production, mol /minute
Carrier oil	-5.53e-3	2.32e-5
HVGO	-7.29e-3	9.31e-5

Reactions of TAN reduction and NA decarboxylation are zero order in the concentration of NA in oil mixtures, and the rate constant of each reaction equals to the absolute value of the regression line slope. Therefore, the rate constants of the TAN reduction reaction in carrier oil and HVGO are similar because of two parallel lines, indicating the reaction rate is independent of the diluents. For CO<sub>2</sub> production, the rate constant in HVGO is much higher than that in carrier oil (9.31e-5 for HVGO and 2.32e-5 for carrier oil). The reason for this behavior could be that the molecular weight of the HVGO acids should be higher than that of the model NA, this would not change the intrinsic behavior of the carboxylic acid group, but it would facilitate the decomposition of the formed carboxylate salt.

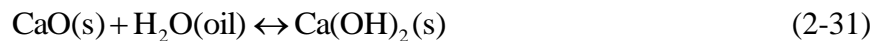
#### 2.5.7.4 Transport Resistance

To test the transport resistance of the reaction of NA conversion, the reaction was performed in a Parr reactor with an agitator. The data (Figure 2-41) show TAN of the oil mixture had the much higher reduction in the stirred reactor

than that in the batch reactor over a period of 90 minutes, even with the much lower heating rate in the Parr reactor. The transport resistance of the calcium naphthenate intermediates may play a significant role in the reduction of NA in oil. No matter which reactor was used for the reaction, the NA conversion reaction would happen only NA was transported to the surface of the calcium oxide. At the initial time of the reaction, NA experienced the diffusion resistance in the bulk oil phase and in the limited pores of CaO particles, with the formation of calcium naphthenate, NA had to penetrate through a layer of calcium naphthenate to reach the surface of CaO. The Parr autoclave was used in the study with an agitator operating at circa 60 rpm, which contributed to the good dispersion and mixing of solid particles in the carrier oil. More important, the agitation facilitated the calcium naphthenate intermediates to dissolve in the oil at the reaction temperature, which thinned the layer of the calcium naphthenate on the surface of CaO, and reduced the NA transport resistance to the surface of CaO significantly. Compared with the Parr reactor, the agitation in a microreactor was much milder, which likely resulted in an incomplete dissolution of the naphthenate and less effective contact between the calcium oxide and the acid. Therefore, a suitable reactor with a stirrer should be used for studies of the oil system in this work, moreover, a fast heating is the other criteria for the reactor selection. When the transport resistance is likely a reaction intermediate at the solid surface, then the classic approaches of changing particle size and agitation are unlikely to completely overcome the transport resistance.

### 2.5.7.5 Proposed mechanism of Liquid-Phase Catalytic Decarboxylation of NA in Oil and Implications for Process Design

Although a great deal of the research work has been conducted to explore the mechanism of ketonization of carboxylic acids by decarboxylation, the mechanism of this reaction remains under debate. Based on the experimental observations in our work, a hypothetical mechanism of decarboxylation was proposed. Guarino (Guarino 2006) pointed out that the reaction between butyric acid and carbonate or oxide does not seem to be occurring just on the surface but in the whole bulk of the powder, which was substantiated by the low specific surface area of the powder of CaO used in our work. As results shown in Table 2-13, the specific surface area of the fresh CaO is only as low as 0.476 m<sup>2</sup>/g. Therefore, four reactions may take place simultaneously to produce calcium naphthenate, the equations are expressed as:



Naphthenate, as an intermediate of the reaction, was then decomposed to produce CO<sub>2</sub>. Finally CO<sub>2</sub> was released in the gas phase.



Among the above five steps, the decomposition of the naphthenate on the surface was much slower than the others, which is the rate-controlling step,

which is consistent with what we observed based on CO<sub>2</sub> production from both solutions of carrier oil and HVGO. Reaction temperatures had a strong impact on CO<sub>2</sub> production rate because the decomposition of the formed naphthenate was much dependent on temperatures. Higher temperature was favorable for the decomposition.

The mobility of carboxylate between the liquid and the solid may cause fouling problem in the reaction process, if the resulting calcium naphthenate could not be deposited completely as the reaction temperature went down, it should conceive a desalting unit in the process design. Base on the experimental study, alkaline earth metal oxides are active to remove NA from oil by decarboxylation, , but the decomposition of the intermediate is a rate-determining step in the decarboxylation reaction, and this step was slow at the temperature of 365 °C, and a higher temperature was preferable to the decomposition reaction. Thus, it would bring about a challenge for a process design. If designing a continuous reactor, the residence time and temperature should be key factors to be taken into account. A long residence time and high temperature are necessary.

## **2.6 Conclusions**

As mentioned previously, Ding et al. and Zhang et al. (Ding et al. 2008; Zhang et al. 2004; Zhang et al. 2006) conducted their studied on NA conversion in crude oil as well, they put their efforts toward investigating the activity and deactivation of catalysts on NA conversion, no detailed kinetic information was reported in their work. In our work, kinetics of NA conversion in a dilute

hydrocarbon medium was studied experimentally in the presence of alkali metal and alkaline earth metal oxides and carbonates. In addition, the analytic work has been conducted to explore the reaction intermediates. Two reaction mixtures, carrier oil plus commercial NA and HVGO from Athabasca bitumen were applied in the study. The reagent powders of  $\text{Li}_2\text{O}$ ,  $\text{CaO}$ ,  $\text{CaCO}_3$ ,  $\text{BaO}$  and  $\text{MgO}$  were tested. Based on the results obtained, the following conclusions were reached:

1. Among the tested catalysts,  $\text{Li}_2\text{O}$  exhibits the highest reactivity, followed by  $\text{CaO}$ ,  $\text{BaO}$ ,  $\text{MgO}$ , and  $\text{CaCO}_3$ . The reactivity of these materials did not correlate simply with surface area, basicity, or the stability of reaction intermediates.

2. IR and TGA studies performed on the solid samples before and after the reaction led to the conclusion that the naphthenate salt was an intermediate product in the decarboxylation reaction. And IR studies of the washing residues of toluene and pentane further confirmed this observation.

3. SEM images and XRD patterns of the solid samples before and after the reaction revealed the formation of metal hydroxide, which indicated the production of water during the reaction process.

4. EDX/SEM and AES analysis of the solid samples before and after the reactions demonstrate the mobility of the carboxylate between the liquid and the solid.

5. Kinetic studies showed that the removal rate of TAN and the decarboxylation of NA were both independent of the concentration of NA over

the range studied. Therefore, the conclusion was drawn that the TAN removal and the decarboxylation of NA are all the zero order reaction in the NA. The overall activation energies were obtained, 38.25 kJ/mol for the TAN removal, and 52.37 kJ/mol for decarboxylation of NA.

6. The actual gas oil, HVGO, exhibits the similarity to the model oil mixture that the decarboxylation reaction follows the zero-order kinetics in the concentration of NA in oil. Comparing with carrier oil, the decarboxylation rate in HVGO is much higher, which attributes to the heavier HVGO acids than that of the model NA. The bigger the anion of the formed naphthenate is, the easier it decomposes.

## **2.7 Recommendations**

Although the catalyst screening and kinetics of the decarboxylation of NA on the best catalyst have been completed in this work, which were quantified to meet the objectives for this study, the following recommendations are suggested for further studies:

1. Naphthenate salt was found as an intermediate product in the decarboxylation reaction of NA, but its yield was not measured quantitatively because no solvent was found to be used as a washing solvent which did not flush away the formed naphthenate salt from the solid samples. Therefore, further efforts should be put on searching for an effective washing solvent, or to recover the naphthenate products more completely.

2. Phenomena such as solubility of the formed carboxylate salt in the bitumen should be considered in the study of potential commercial processes to remove NA from bitumen.

## References

- Al-Sammerrai, D., and Abdul-Razaak, F. S. (1984). "Study of the thermal stabilities of alkali-metal naphthenates." *Thermochimica Acta*, 77, 185-190.
- Atkins, P., Overton, T., Rourke, J., Weller, M., and Armstrong, F. (2006). "Inorganic Chemistry, 4th Edition." *Oxford University Press*.
- Bamberger, E. (1910). "The behaviour of Essig acidic hydrate at higher temperatures." *Berichte*, 43, 3517-3520.
- Bearden, R., Blum, S. C., Olmstead, W. N., and Robbins, W. (1999). "Process for reducing total acid number of crude oil." US 5,891,325.
- Beens, J., Jijssen, R., and Blomberg, J. (1998). "Prediction of comprehensive two-dimensional gas chromatographic separations: A theoretical and practical exercise." *Journal of Chromatography A*, 822, 233-251.
- Bell, J., and Reed, R. I. (1952). "Isotopic tracer studies of pyrolytic reactions, Part I. The formation of acetaldehyde." *Journal of the Chemistry Society*, 1383-1389.
- Bell, J. L. (1994). "Thermal decomposition of acetate: III Catalysis by mineral surfaces." *Geochimica et Cosmochimica Acta*, 58(19), 4155-4177.
- Bienstock, M. G., Matragrano, J. G., Patel, R. D., and Bearden, R. (2000). "Thermal process for reducing total acid number of crude oil." US 6,086,751.
- Blum, S. C., Olmstead, W. N., and Bearden, R. (1998). "Thermal decomposition of naphthenic acids." *US 5,820,750*.

- Bowker, M., and Madix, R. J. (1981). "The adsorption and oxidation of acetic acid and acetaldehyde on Cu(110)." *Applied Surface Science*, 8(3), 299-317.
- Chamberlain, P. R. O. (2004). "Process for reducing naphthenic acidity of petroleum oils field of the Invention." W/O04/005434.
- Croix, A. d. L., English, R. B., and Brown, M. E. (1998). "Modeling the thermal decomposition of solids on the basis of lattice energy changes." *Journal of Solid State Chemistry* 137, 332-345.
- Curtis, R. G., Dobson, A. G., and Hatt, H. H. (1974). "The ketonization of higher fatty acids with some observations on the mechanism of the reaction Part I: Studies on waxes." *J. S. C. I.*, 66, 402-407.
- D664-04. (2004). "Standard test method for acid number of petroleum products by potentiometric titration " *2004 Annual Book of ASTM Standards, Section 5, Petroleum Product, Lubricants, and Fossil Fuels* 275-281.
- Ding, L., Yang, H., Rahimi, P., NG, S., Omotoso, O., Chen, J., and Ring, Z. (2008). "Naphthenic acid removal by catalytic decarboxylation on alkaline earth oxide catalysts." *the Proceedings for the World Heavy Oil Congress, Edmonton, Alberta, Canada*, 304.
- Dzidic, I., Somerville, A. C., Raia, J. C., and Hart, H. V. (1988). "Determination of naphthenic acids in California crudes and refinery wastewaters by fluoride ion chemical ionization mass spectrometry." *Analytical Chemistry*, 60(13), 1318-1323.
- Edmondson, J. G. (1987). "Method of inhibiting propionic acid corrosion in distillation units." US 4,647,366.

- Ferguson, S., and Reese, D. D. (1986). "Upgrading heavy gas oils." US 4,589,979.
- Fuson, R. C. (1966). "Chapter 4 Formation of aldehydes and ketones from carboxylic acids and their derivatives." *The Chemistry of the Carbonyl Group*, London; New York, Interscience publishers.
- Gerchakov, S., and Schultz, H. P. (1967). "Decarboxylation studies: III Rate of ketonic decarboxylation of lead (II) octanoate." *Journal of Organic Chemistry*, 32(5), 1656-1658.
- Glinski, M., and Kaszubski, M. (2000). "Catalytic ketonization over oxide catalysts, Part IV. Cycloketonization of diethyl hexanodiate." *React. Kinet. Catal. Lett.*, 70(2), 271-274.
- Glinski, M., and Kijenski, J. (2000). "Decarboxylative coupling of heptanoic acid, manganese, cerium and zirconium oxides as catalysts." *Applied Catalysis A: General*, 190, 87-91.
- Glinski, M., Kijenski, J., and Jakubowski, A. (1995). "Ketones from monocarboxylic acids: Catalytic ketonization over oxide systems." *Applied Catalysis A: General*, 128, 209-217.
- Groff, R. P., and Manogue, W. H. (1983). "An Infrared study of formate formation and reactivity on TiO<sub>2</sub> surface." *Journal of Catalysis*, 79, 462-465.
- Grootendors, E. J. (1994). "Selective reduction of acetic acid to acetaldehyde on iron oxide." *Journal of Catalysis*, 148, 261-269.
- Guarino, C. (2006). "Removal of naphthenic acids from bitumen through vapour-phase decarboxylation." *Master Thesis at University of Alberta*.

- Hites, R. A., and Biemann, K. (1972). "On the mechanism of ketonic decarboxylation: Pyrolysis of calcium decanoate." *Journal of the American Chemical Society*, 94(16), 5772-5777.
- Holowenko, F. M., MacKinnon, M. D., and Fedorak, P. M. (2001). "Naphthenic acids and surrogate naphthenic acids in methanogenic microcosms." *Water Research*, 35, 2595-2606.
- Holowenko, F. M., MacKinnon, M. D., and Fedorak, P. M. (2002). "Characterization of naphthenic acid sin oil sands wastewaters by gas chromatography-mass spectrometry." *Water Research*, 36, 2843-2855.
- <http://www.dynaloy.com/images/TechBrief042006.pdf>. "Spotlight on dynaloy LLC's analytical capabilities."
- <http://www.panalytical.com/index.cfm?pid=135>. "X-ray Diffraction."
- Kanda, W. S. (2003). "Quinoline conversion in the presence of Athabasca derived heavy gas oil fractions." *Thesis of Master*.
- Kim, J.-W., and Lee, H.-G. (2001). "Thermal and carbothermic decomposition of  $\text{Na}_2\text{CO}_3$  and  $\text{Li}_2\text{CO}_3$ ." *Metallurgical and Materials Transactions B*, 32B, 17-24.
- Kim, K. S., and Barteau, M. A. (1990). "Structure and composition requirements for deoxygenation, dehydration, and ketonization reactions of carboxylic acids on  $\text{TiO}_2$  (001) single-crystal surfaces." *Journal of Catalysis*, 125, 353-375.

- Kishi, K., and Ikeda, S. (1980). "X-ray photoelectron spectroscopic study for the adsorption of acetic acid and ethylenediamine on iron and nickel." *Applied Surface Science*, 5(1), 7.
- Kuriacose, J. C., and Jewur, S. S. (1977). "Studies on the surface interaction of acetic acid on iron oxide." *Journal of Catalysis*, 50, 330-341.
- Kwart, H., and King, K. (1969). "The chemistry of carboxylic acids and esters." *London; New York, Interscience publisher*, 362.
- Lee, C. C., and Spinks, J. W. T. (1953). "The pyrolysis of calcium salts of carboxylic acids." *Canadian Journal of Chemistry*, 31, 103-106.
- Leicester, J., and Redman, M. J. (1962). "Thermal decomposition of the nickel and cobalt salts of aliphatic acids." *Journal of Applied Chemistry*, 12, 357.
- Leung, A., Boocock, D. G. B., and Konar, S. K. (1995). "Pathway for the catalytic conversion of carboxylic acids to hydrocarbons over activated alumina." *Energy & Fuels*, 9, 913-920.
- Lorenzelli, V., Busca, G., and Sheppard, N. (1980). "Infrared study of the surface reactivity of hematite." *Journal of Catalysis*, 66(1), 28-35.
- Malik, W. U., and Gupta, D. R. (1985). "Kinetic study of thermal decomposition of calcium carbonate in the presence of  $K_2CO_3$  and  $BaCO_3$ ." *Journal of Materials Science Letters*, 4, 532-536.
- Miller, A., Cook, N. C., and Whitmore, F. C. (1950). "The ketonic decarboxylation reaction: The ketonic decarboxylation of trimethylacetic acids and isobutyric acid." *Journal of the American Chemical Society*, 72(6), 2732-2735.

- Moser, F. R. (1940). "Process for removing naphthenic acids from hydrocarbon oils." US 2,186,425.
- Palmer, D. A., and Drummond, S. E. (1986). "Thermal decarboxylation of acetate. Part I. The kinetics and mechanism of reaction in aqueous solution." *Geochimica et Cosmochimica Acta*, 50, 813-823.
- Parida, K., and Mishra, H. K. (1999). "Catalytic ketonisation of acetic acid over modified zirconia 1 Effect of alkali-metal cations as promoter." *Journal of Molecular Catalysis A: Chemical*, 139, 73-80.
- Parrott, S. L., Rogers, J. W., and White, J. (1978). "The decomposition of ethanol, propanol, and acetic acid chemisorbed on magnesium oxide." *Applied Surface Science*, 1(4), 443-454.
- Pestman, R., Duijine, A. V., Pieterse, J. A. Z., and Ponec, V. (1995). "The formation of ketones and aldehydes from carboxylic acids, structure-activity relationship for two competitive reactions." *Journal of Molecular Catalysis A: Chemical*, 103, 175-180.
- Pestman, R., Koster, R. M., Duijine, A. V., Pieterse, J. A. Z., and Ponec, V. (1997a). "Reactions of carboxylic acids on oxides 2. Bimolecular reaction of aliphatic acids to ketones." *Journal of Catalysis* 168, 265-272.
- Pestman, R., Koster, R. M., Pieterse, J. A. Z., and Ponec, V. (1997b). "Reactions of carboxylic acids on oxides 1. Selective hydrogenation of acetic acid to acetaldehyde." *Journal of Catalysis*, 168, 255-264.
- Petersen, P. R., Robbins, F. P., and Winston, W. G. (1993). "Naphthenic acid corrosion inhibitors." US 5,183,013.

- Rajadurai, S. (1994). "Pathways for carboxylic acid decomposition on transition metal oxides." *Cataly. Rev. -Sci. Eng.*, 36(3), 385-403.
- Randall, H. W., Fowler, R. G., Fuson, N., and Dangel, J. R. (1949). "Infrared determination of organic structures." *D. Van Nostrand Company, Inc. , New Jersey*.
- Sartori, G., Savage, D. W., Ballinger, B. H., and Dalrymple, D. C. (2001). "Process for extraction of naphthenic acids from crudes." US 6,281,328 B1.
- Scheaffer, R. L., and McClave, J. T. (1995). "Probability and statistics for engineers." *Duxbury Press*.
- Schommer, C., Ebel, K., Dockner, T., Irgang, M., Hoelderich, W., and R., H. (1990). "Preparation of ketones." US 4,950,763.
- Shriver, D. F., Atkins, P., and Langford, C. H. (1994). "Inorganic Chemistry, 2nd Edition." *W. H. Freeman and Company, New York*.
- Silva, J. P. (2007). "Characterization of commercial ceramic adsorbents and its application on naphthenic acids removal of petroleum distillates." *Materials Research*, 10(2), 219-225.
- Siskin, M., Manalastas, P. V., and Sartori, G. (2001). "Process for treatment of petroleum acids." US 6,190,541 B1.
- Spitz, R. N., Barton, J. E., Barteau, M. A., Staley, R. H., and Sleight, A. W. (1986). "Characterization of the surface acid-base properties of metal oxides by titration/displacement reactions." *Journal of Physical Chemistry*, 90, 4067.
- St. John, W. P., Rughani, J., Green, S. A., and McGinnis, G. D. (1998). "Analysis and characterization of naphthenic acids by gas chromatography-electron

- impact mass spectrometry of tert-butyldimethylsilyl derivatives." *Journal of Chromatography A*, 807, 241-251.
- Swaminathan, R., and Kuriacose, J. C. (1970). "Studies on the ketonization of acetic acid on chromia : II. The surface reaction." *Journal of Catalysis*, 16, 357-362.
- Szymanski, H. A., and Alpert, N. L. (1964). "IR theory a practice of infrared spectroscopy." *Plenum Press, New York*, 205.
- Varadaraj, R. (2002). "Removal of acids from oil." US 6,454,936.
- Varadaraj, R., Savage, D. W., and Wales, W. E. (1999). "Removal of naphthenic acids in crude oils and distillates." US 5,961,821.
- Verachtert, T. A. (1980). "Trace acid removal in the pretreatment of petroleum distillate." US 4,199,440.
- Volkenstein, T. (1960). "Advances in catalysis and related subjects." 219.
- Wu, C., and Lin, C. (2005). "Decomposition of calcium carbonate in the temperature range 1180-1353 K " *Journal of Chemical Engineering of Japan*, 38, 734-736.
- Zhang, A., Ma, Q., and Tang, Y. (2004). "Catalytic decarboxylation for naphthenic acid removal from crude oils - A theoretical and experimental study." *Am. Chem. Soc., Div. Pet. Chem.*, 49(2), 21-221.
- Zhang, A., Ma, Q., Wang, K., Goddard, W. A., and Tang, Y. (2005). "Improved processes to remove naphthenic acids." *Annual Technical Progress Report DOE Award No. DE-FC26-02NT15383*.

Zhang, A., Ma, Q., Wang, K., Liu, X., Shuler, P., and Tang, Y. (2006).  
"Naphthenic acid removal from crude oil through catalytic decarboxylation  
on Magnesium oxide." *Applied Catalysis A: General*, 303, 103-109.

## **SECTION 3 MODEL OF KRAFT PULPING KINETICS<sup>1</sup>**

Kraft pulping is a process in which lignin is removed in the presence of sodium hydroxide and sodium sulfide, and it still plays an important role in the pulping process worldwide today. Therefore, modeling the Kraft pulping process is essential and significant for the optimization of the process conditions. In this section, the development of a kinetic model of Kraft pulping was summarized.

### **3.1 Literature Review**

In this subsection, the brief introduction was given on the wood chemistry and structure first, and then two subjects pertinent to the delignification were reviewed. The one focuses on the kinetic models developed by the previous work, the other is on the effect of mass transfer on the delignification reactions.

#### **3.1.1 Wood Chemistry and Structure**

There are four main constituents comprising wood: cellulose, hemicellulose, lignin, and extractives. The chemical formula for cellulose is  $(C_6H_{10}O_5)_n$ , where  $n$  is the number of repeating sugar units or the degree of polymerization. In plant fibres, cellulose determines the character of the fiber. The hemicelluloses are composed of five different sugars: Glucose, mannose, galactose, xylose, and arabinose. Cellulose and hemicellulose are called holocellulose. Lignin is an amorphous, highly-polymerized substance, and it

---

<sup>1</sup> A version of this section has been published, "Kinetic mode for Kraft pulping process, Ind. Eng. Chem. Res., 2005, 44, 7078-7085"

glues the wood tracheids together. The chemistry of lignin is complex. The structure consists primarily of a three dimensional polymer of phenolic groups linked with a variety of ether and carbon-carbon bonds. The extractives include resin acids, fatty acids, terpenoid compounds, alcohol, and so on. Most of these substances are soluble in water or organic solvents. The content percentage of individual substance in wood is illustrated in Figure 3-1.

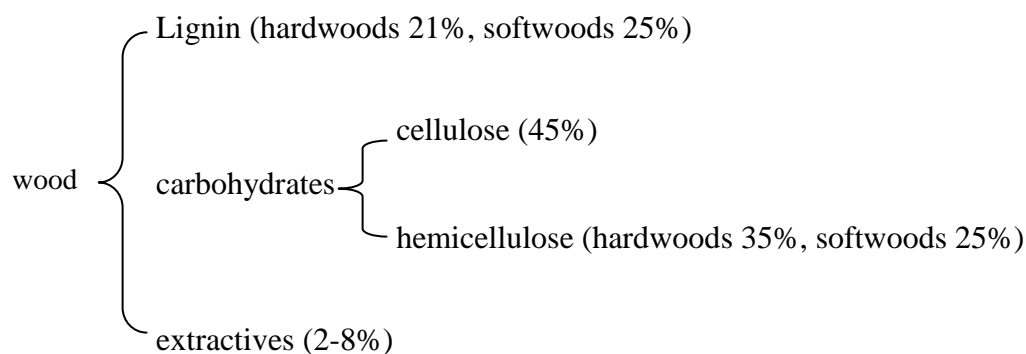


Figure 3-2 Chemical Components of Wood

The fibers, called tracheids in softwoods, have a primary wall P and three secondary wall layers S1, S2, and S3. The inner layer S1 and outer layer S3 are very thin compared to the middle layer S2 which contains 80-90% of the fiber-wall material. All three secondary layers are composed of cellulosic microfibrils embedded in an amorphous matrix of hemicelluloses and lignin. The middle lamella consists mainly of lignin, and glues the wood tracheids together. The object of Kraft pulping is to remove enough lignin from the middle lamella of the wood to release fibers. The structured layers of softwood tracheids are illustrated in Figure 3-2 (Smook 2002).

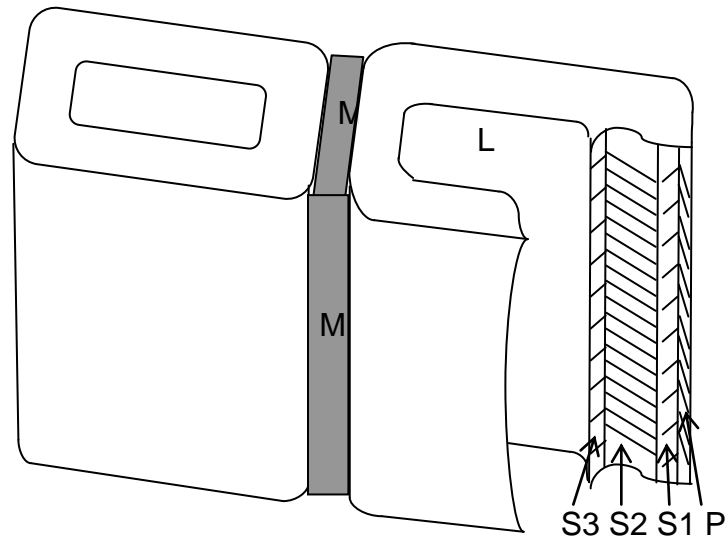


Figure 3-3 the Structure Features of Softwood Tracheids (L: Lumen; P: primary wall; S<sub>1</sub>: inner layer; S<sub>2</sub>: middle layer; S<sub>3</sub>: outer layer; M: middle lamella)

### 3.1.2 The Kraft Pulping Process

The Kraft pulping is the process in which wood chips are heated in an aqueous solution of sodium hydroxide and sodium sulfide from approximately 70 °C to a cooking temperature of about 170 °C, followed by a 1-2 hours cooking period. Meanwhile lignin is removed by sodium hydroxide and sodium sulfide under high temperature. The cooking process can be either batch or continuous. In the batch process, a cooking cycle includes loading, cooking, and dumping. In the continuous process, the chips and liquor are fed at a constant rate into the top of the digester and the chips move downward in a continuous manner for discharge from the bottom. Liquor is extracted, circulated through heat exchangers, and reintroduced into the moving chip column to provide the heat necessary for cooking. The total cooking time is determined by the rate of

downward movement of the chip column. In both the batch and continuous processes, the cooked chips are discharged from the digester under pressure. As the chips are blown from the digester, the mechanical force of the ejection breaks up the wood chips into individual fibers, and the wood pulp is produced. A general flow diagram of a batch process is shown in Figure 3-3.

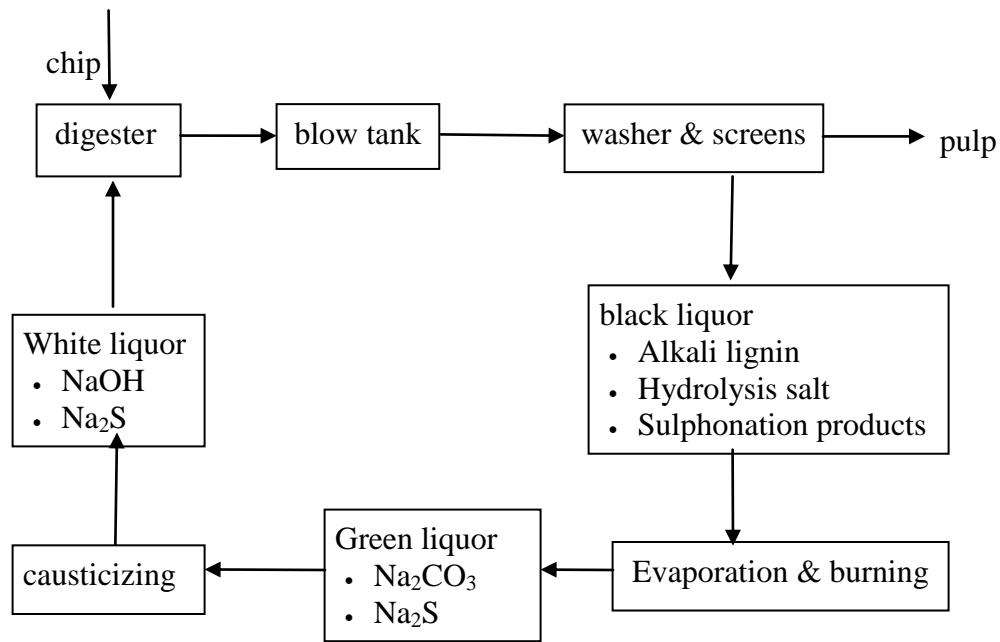


Figure 3- 4 Flow Sheet of the Kraft Pulping Process

### 3.1.3 Previous Kinetic Models in Kraft pulping Process

Since the Kraft pulping method was commercialized in Sweden, it has been playing the important role in pulp industry worldwide, and seems to maintain its dominant role for the near future. Therefore, modeling Kraft pulping process is essential and significant for optimization of the process conditions.

Kraft pulping models with various complexities have been developed for control and design purposes. An early well-known kinetic model was developed by Vroom (Vroom 1957) who combined the effect of cooking temperature and time into one variable named the H factor to describe the impact of temperature on the reaction rate. The H factor is still used in many control schemes for the pulping process. However, the correlation based on H factor did not take into account the influences of wood composition and concentration of pulping chemicals. Therefore, some models have been developed in which temperature and concentration factors were considered. Typical of these is Hatton's model (Hatton 1973) that predicted the kappa number and yield for a variety of wood species:

$$X = a - b[(\log H) \times (EA)^n] \quad (3-1)$$

Where X is the yield or kappa number; a and b are parameters; H is H factor, which is defined as the area under the curve which represents the relative reaction rate as function of the cooking time in hours; EA is the effective alkali concentration (Total of NaOH+1/2 Na<sub>2</sub>S).

Wilder and Daleski (Wilder and Daleski 1965) assumed that the effects of sulfide and hydroxide were additive. Therefore, they explored the delignification kinetics of the Kraft pulping process starting with study of the soda system. The model was given by the Equation.

$$-\frac{dL}{dt} = (k_1[\text{OH}^-] + k_2[\text{S}]^n)L \quad (3-2)$$

Where  $k_1$  and  $k_2$  are rate constants of  $\text{OH}^-$  and S, respectively; [S] denotes the concentration of sulphide. In their kinetic model, sulfide, as the active delignification agent, was taken into account.

Kerr (Kerr 1970; Kerr and Uprichard 1976) developed a semi-theoretical model

$$\frac{dL}{dt} = -k[\text{OH}^-]L \quad (3-3)$$

Where L is the lignin content; k is the rate constant;  $[\text{OH}^-]$  is the concentration of alkali. Kerr believed that  $[\text{OH}^-]$  was the function of the pulp lignin content. Their relationship has been observed to be well represented by two intersecting straight lines over most course of the cook (Aurell and Hartler 1965; Kerr 1970), indicating a two-stage reaction involved. In the first stage,  $[\text{OH}^-]$  decreased dramatically with a little amount of lignin removed, and most of the lignin was removed in the second stage in which  $[\text{OH}^-]$  was consumed at a much slower than that in the first stage. The kinetic model was expressed as the form.

$$\left[ \frac{1}{b_1} \ln \frac{L}{L + b_1/a_1} \right]_{L_t}^{L_i} + \left[ \frac{1}{b_2} \ln \frac{L}{L + b_2/a_2} \right]_{L_f}^{L_t} = \int_0^t k dt = a_3 H + a_4 \quad (3-4)$$

Where  $a_1$  is the slope of the alkali concentration versus lignin yield line in the first stage;  $b_1$  is the intercept of the same line;  $a_2$  the slope of the alkali concentration versus lignin yield line in the second stage;  $b_2$  is the intercept of the same line;  $a_3$  is the constant related to the delignification rate constant;  $a_4$  is a constant added to correct from the failure of a lot of the left-hand side of Eqn. (3-4) vs H-factor to pass through the origin;  $L_i$  is the lignin content of the wood at the initial time;  $L_f$  is the lignin content of the wood at the final time;  $L_t$  is the

lignin content at the transition point of the transition point of two reaction stages. This model did not include the reactions of carbohydrates.

Smith and Williams (Smith and William 1974) proposed that lignin was composed of two classes, each class possessed different reactivity in 70% and 30%, respectively, and was degraded by two different reactions with hydroxide ion alone and with a combination of hydroxide and hydrosulfide ions. This reaction scheme is shown below



where  $L_1$  and  $L_2$  are the two fractions of lignin with different reactivity in the wood, and  $L_d$  is the fraction of dissoluble lignin. The delignification kinetic model was given in general form

$$\frac{dC_i}{dt} = -k_1[OH^-]C_i - k_2[OH^-][HS^-]C_i \quad (3-9)$$

Where  $C_i$  is the concentration of the wood components;  $[OH^-]$  is the concentration of alkali;  $[HS^-]$  is the concentration of hydrosulfide ion;  $k_1$  and  $k_2$  are the rate constants. In their study, wood was divided into 5 species: two classes of lignin with different reactivity, cellulose, galactoglucomannan, and araboxytan.

In a commercial Kraft pulping process, the typical liquor-to-wood ratio is about 3-5:1 L/kg, so the concentration of hydroxide and hydrosulfide ions decreases during the cooking process. Only under the condition of high Liquor-to-wood ratios, the concentrations of hydroxide and hydrosulfide ions can be assumed as constant. Therefore, when a typical Liquor-to-wood ratio is employed, a model should take into account the consumption of chemicals while lignin and carbohydrates are removed. As described by the other investigations (Sjostom 1981), the chemicals are consumed mainly in four reactions: hydrolysis of acetyl side groups associated with hemicellulose polymers; neutralization of the acid products in the wood; peeling reactions of carbohydrate; the formation of lignin degradation products. Thus, it is difficult to determine the amounts of chemicals only consumed by delignification reaction. Rekunen, et al. (Rekunen et al. 1980) conducted the experimental study on the dependence of the yields of carboxylates and lignin on the concentration of the effective alkali, the reaction underwent two stages, and the carbohydrate reaction rate was linear with the delignification rate for each stage.

In Smith (Smith and William 1974) model, the rate of reaction for the chemical consumption was related to the wood component reaction as follows

$$\frac{d[\text{OH}^-]}{dt} = \frac{1}{r_{L/W}} \left( a_1 \frac{dL}{dt} + a_2 \frac{dC}{dt} \right) \quad (3-10)$$

$$\frac{d[\text{HS}^-]}{dt} = \frac{1}{r_{L/W}} a_3 \frac{dW}{dt} \quad (3-11)$$

Where  $a_1$ ,  $a_2$  and  $a_3$  are the proportionality constant, they were calculated by using chemical data from an industry kraft cook.  $W$  is the undissolved wood, (g/g o.d.w), and

$$\frac{dW}{dt} = \frac{dL}{dt} + \frac{dC}{dt} \quad (3-12)$$

The approach of Smith and Williams, which incorporated a rather complete set of chemical steps, seems most promising. It will be used as a starting point in the development of an improved kinetic model for Kraft pulping in both batch and continuous flow digesters.

Except for the kinetic model mentioned above, there are numerous studies to explore the kinetics of Kraft pulping. Some models divided the Kraft pulping into three periods (Gustafson et al. 1983; Kleinert 1966; Rekenen et al. 1980): initial, bulk and residual. The kinetic model of each period was developed. The initial period is characterized by rapid delignification, significant hemicellulose degradation, and large alkali consumption. Olm and Tistad (Olm and Tistad 1979) derived the delignification rate in the initial period of Kraft pulping, which was independent on the concentration of effective alkali and hydrosulfide. This may be caused by the fact that the cleavage of phenolic  $\alpha$  aryl-ether groups takes place at a very high rate at the pulping temperature as long as the PH is above 12, the delignification in the initial period is mainly attributed to the cleavage of aryl-ether linkages (Ljunggren 1980). Gustafson (Gustafson 1982) derived the delignification rate equation for the initial period from Olm's data

$$\frac{dL}{dt} = 36.2T^{1/2}e^{(-4807.69/T)}L \quad (3-13)$$

Where L is the lignin content (% on wood); T is temperature (K); t is time, (min).

Most of the lignin is removed in the bulk stage, and carbohydrate degradation continues in this stage at a much slower rate than that in the initial period. In this period, chemical reaction is assumed to be the rate-controlling step. The bulk delignification kinetics has been the main subject of the research (Christensen et al. 1983; Kleinert 1966; Lemon and Teder 1973; Wilder and Daleski 1965). The models currently shown in the literature can be expressed as:

$$-\frac{dL}{dt} = (k_{01}e^{-E_{a1}/(RT)}[OH^-]^a + k_{02}e^{-E_{a2}/(RT)}[OH^-]^b[HS^-]^c)L \quad (3-14)$$

Where L is the concentration of lignin in wood;  $[OH^-]$  is the alkali concentration;  $[HS^-]$  is the hydrosulfide concentration; and  $k_{01}$  and  $k_{02}$  are the frequency factor; and  $E_{a1}$  and  $E_{a2}$  are the activation energy, whose values reported in the literature are in the range of 120-150 kJ/mol for softwood. Different values of parameters a, b, and c were found in the different models.

The residual period is characterized by a very slow delignification and significant alkali consumption. Norden and Teder (Norden and Teder 1979) derived that the kinetic model in the residual period was a zero-order with respect to hydrosulfide concentration. The equation was expressed as

$$-\frac{dL}{dt} = k_{01}e^{-E_a/(RT)}[OH^-]^a L \quad (3-15)$$

In this period, activation energy  $E_a$  is estimated to be in the range of 90-125 kJ/mol (Chiang and Yu 1989).

As for the carbohydrate reaction rate during the three-delignification periods, the researchers assumed that the carbohydrate reaction rate was a linear

function of the delignification rate, as shown by Olm and Tistad (Olm and Tistad 1979),

$$-\frac{dC}{dt} = a \cdot \left(-\frac{dL}{dt}\right) \quad (3-16)$$

The different values of proportionality constant,  $a$ , were found for the three-delignification stages.

The alkali consumption rates in the three-delignification periods were also expressed as a function of the dissolution rate of wood species (Giudici and Park 1996)

$$-\frac{d[\text{OH}^-]}{dt} = a\left(-\frac{dC}{dt}\right) + b\left(-\frac{dL}{dt}\right) \quad (3-17)$$

$$-\frac{d[\text{HS}^-]}{dt} = c\left(-\frac{d[\text{OH}^-]}{dt}\right) \quad (3-18)$$

All these kinetic modeling studies started with the assumption of pseudo-homogeneous pulping process. The heterogeneous nature of pulping process has been noticed by Larocque and Maass (Larocque and Maass 1941) who observed adsorption during the alkaline pulping process. The cooking chemicals adsorbed at the interface between the liquid alkali and the lignin. Therefore, the consideration of pseudo-homogenous assumption causes error during the modeling of pulping process, thus the development of a heterogeneous delignification kinetic model is essential and significant to explore the state-of-the-art kraft pulping process.

Although Kraft pulping has significant advantages in pulp properties, such as high pulp strength, there are still some issues needed to be resolved, such as

low yield from wood, and the comparatively high residual lignin content of bleachable grades. Therefore, many researchers strived to improve Kraft pulping process over the years, and the various pulping modifications have been developed, including cooking additives, chip pretreatments and two-stage cooks, and so on.

As previously discussed, the carbohydrate degradation is caused by the “peeling” reaction in which terminal reducing groups are stripped one by one from the end of the polysaccharide chains. New reducing end groups, at which peeling can begin, are produced by hydrolytic splitting once the temperature exceeds 150 °C. The challenging question is rising: is it possible to terminate the peeling reaction to prevent carbohydrate degradation from happening? The answer is positive. The method is to modify the reducing end groups so that they cannot take part in the peeling reaction, including oxidation to an organic acid, reduction to an alditol group, or substitutions with an alkali stable end group.

AQ is now widely accepted as a popular additive for alkaline pulp mills. A small addition of AQ accelerates the kraft pulping reactions, and gives a 1 to 2 % (on dry wood) increase in yield (Fleming et al. 1978; Holton and Chapman 1977; Macleod et al. 1980; Macleod and Kingsland 1990). The mechanism of the dual function of AQ has been the subject of researches (Fleming et al. 1979; Obst et al. 1979). It is generally accepted that AQ functions in a redox sequence. The first step in the sequence is the reaction of AQ with the reducing group of a carbohydrate thus stabilizing the carbohydrate against alkaline peeling and producing the reduced form of AQ(AHQ), which is soluble in alkali. The AHQ

reacts with the quinonemethide segment of the lignin polymer increasing the rate of delignification. At the same time, the AHQ is converted back to AQ which can participate again in the redox cycle.

The use of polysulfide in the cooking liquor to obtain higher pulp yields has been known for over 50 years (Ahlgren and Teder 1967; Green and Prusas 1975; Obiaga and Wayman 1969; Pekkala 1982). Under alkaline conditions and relatively low temperature (100 to 120 °C), polysulfide will oxidize the active end group of the polysaccharide polymer to an alkali-stable aldonic acid, thus stabilizing the polymer against alkaline peeling. This selective reaction is critical because no other polysaccharides are oxidized.

Because the addition of AQ or polysulfide increases the yield, some mills are utilizing both additives together to obtain a maximum yield increase (Jiang 1996; Parthasarathy et al. 1995).

It is generally accepted that Kraft pulp and Kraft + additives have the similar kinetics of delignification. Therefore, for the studies on kinetics of Kraft pulping with additives, for example, Kraft-AQ and Kraft polysulfide, researchers have applied the kinetic model proposed for Kraft pulping to Kraft-AQ or Polysulfide as shown in Eqn. 12. Different exponential factors were found for the different modified Kraft pulping process (Li et al. 2002; Varma and Krishnagopalan 1998).

### 3.2 Development of the kinetic model

In view of the heterogeneous nature of Kraft pulping, the delignification may be considered to occur in a stepwise manner, as follows:

1. Transport of hydroxide and hydrosulfide ions from the bulk liquor to the exterior surface of the chip;
2. Diffusion of the chemical ions to the interior of the chip;
3. Chemisorptions occur on the interior surface;
4. Chemical reaction between the chemical ions and the lignin;
5. Desorption of the dissoluble lignin degradation products;
6. Diffusion of the dissoluble lignin degradation products to the chip exterior;
7. Transport of the dissoluble lignin degradation products in the bulk liquor.

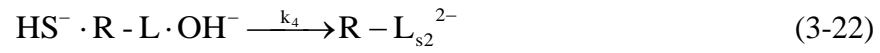
Under normal conditions, the transport steps 1 and 7 are probably unimportant but the diffusion steps of 2 and 6 play a significant role unless the effective thickness of the chips less than the critical thickness (2-3 mm) (Hatton and Keays 1973; Wilder and Daleski 1964). To develop the pure kinetics of pulping process, some factors, for instance, diffusion of cooking chemicals should be eliminated to maintain each wood component freely accessible to the chemical agents. Therefore, the chips with the thickness of 2-3 mm or less can be cooked to reach such point that the transport steps have a negligible effect on the overall observed pulping rate. The chemical reactions involved are said to be rate-controlling steps, which means the overall reaction rate is dependent on steps of 3-5 directly, provided that the chips with the thickness of 2-3mm or less

are cooked. In this project we are interested in the intrinsic kinetics, i.e., steps 3 through 5 only.

### **3.2.1 Reaction Mechanism**

The proposed kinetics of delignification consists of three steps: adsorption of hydroxide and hydrosulfide ions on the active sites on wood cells; chemical reactions in which insoluble lignin is reacted with hydroxide and hydrosulfide ions to produce dissoluble products; desorption of dissoluble reaction products formed on the solid wood cell surface. In our case, the active sites for adsorption of hydroxide and hydrosulfide ions are the sites on the lignin; the adsorption of hydroxide and hydrosulfide ions follows non-competitive mechanism of adsorption. Assuming that lignin in the wood is of identical reactivity. Considering lignin reacts in parallel with sodium hydroxide and sodium sulfide in Smith's model (Smith and William 1974), at the same time, to avoid too many parameters and to reduce the complexity of the kinetic model developed, the lignin was treated as one class with the same reactivity, and the two delignification reactions exist during cooking: one is that lignin reacts with sodium hydroxide only, and the other one is that lignin reacts with both sodium hydroxide and sodium sulfide simultaneously. Moreover, the developed heterogeneous pulping model is based on a lumped parameter approximation, in which the chemical species in wood are lumped, for example, to lignin and carbohydrates, without referring to a specific chemical compound, removing the

complexity of the detailed chemistry involved. A simplistic mechanism has been proposed:



Where R-L denotes the native lignin segments connected with the fibers, on which hydroxide and hydrosulfide can be adsorbed, denoted by  $\text{R-L} \cdot \text{OH}^-$  and  $\text{R-L} \cdot \text{HS}^-$ ;  $\text{HS}^- \cdot \text{R-L} \cdot \text{OH}^-$  denotes the active site occupied by hydroxide and hydrosulfide ions simultaneously; and  $\text{R-L}_{s1}^-$  and  $\text{R-L}_{s2}^{2-}$  denote two kinds of undesorbed reaction products of lignin, and  $\text{L}_s^-$  and  $\text{L}_s^{2-}$  denotes the dissolved lignin degradation products.

Equations (3-19) and (3-20) represent the adsorptions of hydroxide and hydrosulfide ions onto the lignin surface, respectively. The active site for adsorption is assumed to be the sites on the lignin. We assume that one active site for adsorption can adsorb one hydroxide ion and one hydrosulfide ion simultaneously as well, therefore, the adsorptions of hydroxide and hydrosulfide ions are not competitive. There is no doubt that hydrosulfide ion happens to be

adsorbed on the vacant active site, but for the mechanism proposed, such adsorption doesn't appear in the surface reaction mechanism because hydrosulfide ion alone have no effect on the delignification reaction. Equations (3-21) and (3-22) are the surface reaction steps, where the delignification reactions occur that the lignin is converted into dissoluble lignin degradation products. Considering the process of soda pulping, delignification reaction takes place without addition of hydrosulfide ion, Equation (3-20) may occur. Moreover, we assume that the other delignification reaction takes place on the active sites occupied by both hydroxide and hydrosulfide ions simultaneously. Thus, two kinds of lignin degradation reactions proceed by following different reaction path. Equations (3-23) and (3-24) are the desorption of the dissoluble lignin fracture formed.

### **3.2.2 Assumptions**

The Kraft pulping of a wood chip is a very complex phenomenon. Therefore, simplifying assumptions are needed to model the process mathematically. The assumptions are summarized as following:

1. The active sites with the same activity for adsorption are located on the lignin surface, and one active site for adsorption can adsorb one hydroxide ion and one hydrosulfide ion simultaneously;
2. The active site concentration is proportional to the percentage of lignin in wood;

3. Adsorption conforms to Langmuir adsorption model, and surface reactions are the rate-controlling steps;

4. There is no redeposit of dissolved material. It means that the delignification reactions are irreversible, no condensation reactions in which dissolved lignin condenses back on to the wood phase take place. All of the delignification products are desorbed from the lignin surface and dissolved into the cooking liquor;

5. The extent of carbohydrates dissolution is determined only by the amount of lignin dissolved. Therefore, the consumption rate of chemicals by carbohydrates degradation is assumed to be proportional to that by delignification reaction.

### 3.2.3 Adsorption isotherm

According to the assumption 3, it is reasonable to think that the adsorption and desorption reactions occur at a much faster rate than that of surface reactions on the lignin surface. Therefore, one can assume that the adsorption and desorption steps are always in equilibrium. The adsorption process can be represented as the elementary reversible reactions shown by Equations (3-19) and (3-20). Thus, at the time scale of the surface reaction, the equilibrium of adsorption of hydroxide and hydrosulfide ions are given by

$$k_1[\text{OH}^-]C_{v1} - k_{-1}C_{R-L.OH^-} = 0 \quad (3-25)$$

$$k_2[\text{HS}^-]C_{v2} - k_{-2}C_{R-L.HS^-} = 0 \quad (3-26)$$

Where  $C_{v1}$  (mol/kg o. d. wood) and  $C_{v2}$  (mol/kg o. d. wood) denote the vacant surface concentration of the active sites that have not been occupied by hydroxide and hydrosulfide ions, respectively.  $C_{R-L\text{OH}^-}$  (mol/kg o. d. wood) and  $C_{R-L\text{HS}^-}$  (mol/kg o. d. wood) denote the surface concentration of the active sites occupied by hydroxide and hydrosulfide ions, respectively. The rate constants,  $k_1$  ( $M^{-1} \text{ min}^{-1}$ ) and  $k_2$  ( $M^{-1} \text{ min}^{-1}$ ), are the adsorption rate constants of hydroxide and hydrosulfide ions, respectively, and  $k_{-1}$  ( $\text{min}^{-1}$ ) and  $k_{-2}$  ( $\text{min}^{-1}$ ) are the desorption rate constants of hydroxide and hydrosulfide ions, respectively. Equation (3-27) can be reduced to

$$C_{R-L\text{OH}^-} = \frac{k_1}{k_{-1}} [\text{OH}^-] C_{v1} = K_1 [\text{OH}^-] C_{v1} \quad (3-27)$$

Where  $K_1$  ( $M^{-1}$ ) is the adsorption (equilibrium) constant of hydroxide on the active site.

One may expect that the total available active sites be shared by three portions: the vacant sites, coverage of hydroxide and coverage of hydrosulfide if the two adsorptions are competitive. However, hydroxide adsorption is not competitive to the hydrosulfide adsorption, although both adsorptions occur on the same type of active sites, both chemisorptions can occur on one single site simultaneously. As the total number of active sites available is finite, a site concentration balance leads to:

$$C_t = C_{v1} + C_{R-L\text{OH}^-} \quad (3-28)$$

Where  $C_t$  (mol/kg o.d. wood) is the total surface concentration of the active sites on the wood cell surface.

Combining Equations (3-27) and (3-28)

$$C_{v1} = \frac{C_t}{1 + K_1[\text{OH}^-]} \quad (3-29)$$

$$C_{R-L.OH} = \frac{K_1[\text{OH}^-]C_t}{1 + K_1[\text{OH}^-]} \quad (3-30)$$

Which is typical of Langmuir isotherm.

For the adsorption of hydrosulfide ion, the adsorption isotherm can be derived in a similar fashion as for the adsorption of hydroxide

$$C_{v2} = \frac{C_t}{1 + K_2[\text{HS}^-]} \quad (3-31)$$

$$C_{R-L.HS} = \frac{K_2[\text{HS}^-]C_t}{1 + K_2[\text{HS}^-]} \quad (3-32)$$

Where  $K_2$  ( $M^{-1}$ ) is the adsorption (equilibrium) constant of hydrosulfide on the hydroxide-adsorbed active sites.

Therefore, the amounts or concentrations of the hydroxide and hydrosulfide ions on the surfaces of wood cells are directly related to their respective bulk concentration in the liquid phase.

### 3.2.4 Reaction Rate

Based on the reactions depicted by Equation (3-21), we can obtain the rate of the delignification rate by action of the hydroxide ion

$$r_3 = k_3 C_{R-L.OH} \quad (3-33)$$

and the rate of delignification is depicted by Equations (3-22)

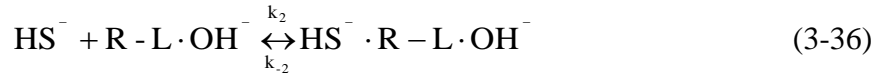
$$r_4 = k_4 C_{HS \cdot R-L.OH} \quad (3-34)$$

Where  $r_3$  and  $r_4$  are the intrinsic rates of delignification for Equations (3-21) and (3-22) as they are written.

The overall rate of delignification is

$$r_s = r_3 + r_4 = k_3 C_{R-L.OH^-} + k_4 C_{HS^-\cdot R-L.OH^-} \quad (3-35)$$

Where  $r_s$  (mol active sites/min/kg wood) is the surface reaction rate expressed by active site concentration.  $C_{HS^-\cdot R-L.OH^-}$  (mol/kg o.d. wood) is the concentration of the active sites occupied by both hydroxide and hydrosulfide ions simultaneously.  $C_{HS^-\cdot R-L.OH^-}$  can be derived by the adsorption of hydrosulfide ion onto the hydroxide-adsorbed active sites or the adsorption of hydroxide onto the hydrosulfide-adsorbed active sites as well, both adsorption will give the same result. Here, we use the adsorption of hydrosulfide onto the active sites preoccupied by hydroxide as an illustrative instance.



The concentration of the active sites occupied by both hydroxide and hydrosulfide ions can be derived from the adsorption equilibrium

$$C_{HS^-\cdot R-L.OH^-} = \frac{k_2}{k_{-2}} [HS^-] C_{v3} = K_2 [HS^-] C_{v3} \quad (3-37)$$

Where  $C_{v3}$  (mole/kg o. d. wood) is the concentration of the hydroxide-adsorbed active sites not occupied by hydrosulfide ion. The site concentration balance leads to

$$C_{R-L.OH^-} = C_{v3} + C_{HS^-\cdot R-L.OH^-} \quad (3-38)$$

Combining Equation (3-37) with Equation (3-38), we obtain

$$C_{v3} = \frac{C_{R-L.OH^-}}{1 + K_2[HS^-]} \quad (3-39)$$

$$C_{HS^- \cdot R-L.OH^-} = \frac{K_2[HS^-]C_{R-L.OH^-}}{1 + K_2[HS^-]} \quad (3-40)$$

Substituting Equation (3-30) into Equation (3-40)

$$C_{HS^- \cdot R-L.OH^-} = \frac{K_1 K_2 [OH^-] [HS^-] C_t}{(1 + K_1 [OH^-]) (1 + K_2 [HS^-])} \quad (3-41)$$

Substituting Equations (3-30) and (3-41) into Equation (3-35), we obtain

$$r_s = \frac{k_3 K_1 [OH^-] C_t}{1 + K_1 [OH^-]} + \frac{k_4 K_1 K_2 [OH^-] [HS^-] C_t}{(1 + K_1 [OH^-]) (1 + K_2 [HS^-])} \quad (3-42)$$

Where  $k_3$  ( $\text{min}^{-1}$ ) and  $k_4$  ( $\text{min}^{-1}$ ) are the rate constants of reactions depicted by Equations (3-21) and (3-22), respectively. The active site concentration  $C_t$  is proportional to the percentage of lignin in wood. i.e.

$$C_t = k_0 \cdot L \quad (3-43)$$

Where  $k_0$  (mol/kg lignin) is proportional constant between lignin content and the active site (i.e. reactive lignin segment) concentration, and  $L$  (kg lignin/kg o.d. wood) is the content (percentage) of lignin in the wood.

Substituting Equation (3-43) into Equation (3-42) and we obtain

$$-r_L = \frac{k_0 k_3 K_1 [OH^-] L}{1 + K_1 [OH^-]} + \frac{k_0 k_4 K_1 K_2 [OH^-] [HS^-] L}{(1 + K_1 [OH^-]) (1 + K_2 [HS^-])} \quad (3-44)$$

Where  $-r_L$  (mol lignin/min/kg wood) is delignification rate expressed by the lignin content.

In a commercial Kraft pulping process, the typical liquor-to-wood ratio is about 3-5:1 L/kg, so the concentration of hydroxide and hydrosulfide ions

decreases during the cooking process. Therefore, when a typical Liquor-to-wood ratio is employed, a model should be necessary to incorporate the consumption of chemicals while lignin and carbohydrates are removed. As described by other investigations(Sjostom 1981), the chemicals are consumed mainly in reactions: hydrolysis of acetyl of wood; peeling reactions of carbohydrate; the formation of delignification products. Thus, it is difficult to determine the amounts of chemicals merely consumed by delignification reaction. Kleinert (Kleinert 1966) assumed that the carbohydrate reaction rate is a linear function of the delignification rate, and the constant of proportionality is independent of pulping conditions. His assumption was proved by later research of Rekenen(Rekenen et al. 1980). To estimate the alkali reaction rate, Gustafson (Gustafson et al. 1983) assumed that the alkali consumption be expressed as a linear function of the acetyl, lignin and carbohydrate degradation rate. In this study, the factors  $f_1$  and  $f_2$  are introduced into the consumption rate of chemicals associated with chemicals consumed by other components in wood, for example, carbohydrate, the consumption rate of hydroxide and hydrosulfide ions are expressed as

$$-r_{\text{OH}^-} = f_1 \cdot (-r_L) = f_1 \left( \frac{k_0 k_3 K_1 [\text{OH}^-] L}{1 + K_1 [\text{OH}^-]} + \frac{k_0 k_4 K_1 K_2 [\text{OH}^-] [\text{HS}^-] L}{(1 + K_1 [\text{OH}^-]) (1 + K_2 [\text{HS}^-])} \right) \quad (3-45)$$

$$-r_{\text{HS}^-} = f_2 \cdot r_4 = f_2 \frac{k_0 k_4 K_1 K_2 [\text{OH}^-] [\text{HS}^-] L}{(1 + K_1 [\text{OH}^-]) (1 + K_2 [\text{HS}^-])} \quad (3-46)$$

One should note that under batch pulping conditions, mass balance of the whole system leads to

For lignin:

$$-r_L = -k_0 \frac{dL}{dt} \quad (3-47)$$

For hydroxide ion in the system, hydroxide ion is distributed in the bulk of liquor and on the surface of lignin by adsorption effect, so mass balance of  $[\text{OH}^-]$  is obtained:

$$-\frac{d([\text{OH}^-]V_L + C_{R-L,\text{OH}^-}W)}{dt} = -r_{\text{OH}^-}W \quad (3-48)$$

For  $[\text{HS}^-]$ , the case is the same as hydroxide ion, mass balance is:

$$-\frac{d([\text{HS}^-]V_L + C_{R-L,\text{HS}^-}W)}{dt} = -r_{\text{HS}^-}W \quad (3-49)$$

Where  $W$  (g o.d. wood) denotes mass of dry wood, and  $V_L$  (L) denotes volume of liquid. So we obtain

$$-\frac{dL}{dt} = \frac{1}{k_0}(-r_L) = \frac{k_3 K_1 [\text{OH}^-] L}{1 + K_1 [\text{OH}^-]} + \frac{k_4 K_1 K_2 [\text{OH}^-] [\text{HS}^-] L}{(1 + K_1 [\text{OH}^-])(1 + K_2 [\text{HS}^-])} \quad (3-50)$$

$$-\frac{d[\text{OH}^-]}{dt} = \frac{1}{\frac{V_L}{W} + \frac{k_0 K_1 L}{(1 + K_1 [\text{OH}^-])^2}} \left( f_1 - \frac{K_1 [\text{OH}^-]}{1 + K_1 [\text{OH}^-]} \right) (-r_L) \quad (3-51)$$

$$-\frac{d[\text{HS}^-]}{dt} = \frac{1}{\frac{V_L}{W} + \frac{k_0 K_2 L}{(1 + K_2 [\text{HS}^-])^2}} \left[ f_2 \cdot r_4 - \frac{K_2 [\text{HS}^-]}{1 + K_2 [\text{HS}^-]} \cdot (-r_L) \right] \quad (3-52)$$

When Equations (3-50)-(3-52) are solved simultaneously, the dynamic (or kinetic) behavior of the delignification can be predicted during the kraft pulping process, and then the lignin and concentration of chemicals can also be predicted.

### 3.3 Estimation of Kinetic Parameters

The Equations (3-50)-(3-52) are highly non-linear, coupled ordinary differential equations. The solution to these equations must be obtained numerically. The parameters in the kinetic model can be estimated by minimizing the variance between the model prediction and experimental data (Giudici and Park 1996; Liu 2004), that is the least squares criterion shown as

$$\min_{\beta} S = \min_{\beta} \sum_{i=1}^n [y(t_i, \beta) - y(t_i)]^2 \quad (3-53)$$

Where  $\beta$  denotes the parameters in the kinetic model of Equations (3-50)-(3-52);  $y(t_i)$  denotes the vector of the measured variables; and  $y(t_i, \beta)$  denotes the vector of the estimated of the corresponding variables.

For the model Equations (3-50)-(3-52), one has:

vector of the measured variables

$$y = [L, [OH^-], [HS^-]]^T \quad (3-54)$$

vector of the initial conditions:

$$y_0 = [L_0, [OH^-]_0, [HS^-]_0]^T \quad (3-55)$$

vector of parameters

$$\beta = [K_1, K_2, k_3, k_4, f_1, f_2, k_0]^T \quad (3-56)$$

In our work, the data of Santos, et al. (Santos et al. 1997) and Wilder and Daleski (Wilder and Daleski 1965) were used to compare with the model prediction. The cooking conditions used by Santos, et al. and Wilder are given in Tables 3-1 and 3-2.

Table 3- 2 Cooking Conditions Used by Santos, et al. (1997)

species	Eucalyptus globules
chip size	3mm × 5mm × 20mm
lignin content	22.1% on dry wood
cellulose content	50.4% on dry wood
pentosans content	23.2% on dry wood
extractives and ash	1.9% on dry wood
moisture	41.2% on dry wood
cooking temperature	100 – 180 °C
liquor-to-wood ratio	5:1 L/kg, 50:1 L/kg
[OH <sup>-</sup> ]	1.2 M
[HS <sup>-</sup> ]	0.18 M

Table 3- 3 Cooking Conditions Used by Wilder and Daleski (1965)

species	loblolly pine
chip size	1 mm × ¼ in. × 2 in
lignin content	29.1% on wood
cooking temperature	142, 150, 160, 171 °C
liquor-to-wood ratio	200:1 L/kg
active alkali concentration	60 g/L as NaOH
Sulfidity	40%

In the work of Santos, et al, two sets of isothermal runs were performed. One set of experiments was carried out at a low liquor-to-wood ratio of 5, in which the concentrations of hydroxide and hydrosulfide ions decreased during the cook. The other was carried out at high liquor-to-wood ratio (50:1 L/kg) in

which the concentration of chemicals kept constant throughout the cook. Data from the two sets of runs were selected to model the kinetics of delignification during Kraft pulping process. Because a comprehensive set of data could not be procured in the open literature, only data at 140, 150 and 160 °C in the experiment of Santos, et al. were employed to compare with the kinetic model of delignification.

If the same cook material, such as Eucalyptus globules in the work of Santos, et al., was cooked under different cooking condition, the parameters in kinetic model are only the function of temperature, and they are independent on liquid-to-wood ratio. Therefore, whether high liquor-to-wood ratio or low liquor-to-wood ratio was employed in the work of Santos, et al., the parameters obtained were the same for these two conditions. To obtain such parameters suitable for both low and high liquor-to-wood ratios, we combined the two set of experimental data under low and high liquor-to-wood ratios to minimize them at the same time.

Considering that the real initial concentration of hydroxide and hydrosulfide ions is lower than that before mixing of liquor with chips because of adsorption effects, mass balance were made at initial time (t=0):

$$V_L[\text{OH}^-]^0 = V_L[\text{OH}^-]_0 + C_{\text{R-L,OH}^-} W_0 \quad (3-57)$$

$$V_L[\text{HS}^-]^0 = V_L[\text{HS}^-]_0 + C_{\text{R-L,HS}^-} W_0 \quad (3-58)$$

Where  $[\text{OH}^-]^0$  and  $[\text{HS}^-]^0$  are the concentrations of hydroxide and hydrosulfide ions in the liquor before mixing with chips. In Santos's work,  $[\text{OH}^-]^0 = 1.2 \text{ M}$ ,  $[\text{HS}^-]^0 = 0.18 \text{ M}$ .  $[\text{OH}^-]_0$  and  $[\text{HS}^-]_0$  are the initial concentrations of hydroxide and

hydrosulfide ions when the reactions start. The parameters estimated are shown in Table 3-3. Figures 3-7, 8, and 9 compare the model predictions with the experimental data under low liquor-to-wood ratio.

Table 3- 4 Kinetic Parameters Estimated from the Experimental Data of Santos, et al.

T, °C	$K_1, M^{-1}$	$K_2, M^{-1}$	$k_3, \text{min}^{-1}$	$k_4, \text{min}^{-1}$	$f_1$	$f_2$	$k_0, \text{mol/kg}$
160	5.63	1.00	0.043	0.0571	2.17	4.78	9.48
150	8.42	1.45	0.0208	0.0179	1.93	4.30	10.1
140	10.6	1.62	0.00872	0.0075	1.65	3.90	11.8

As can be seen from Figures 3-4, 5, and 6, for all of the lignin test cases, the data fit rather well. But for the hydrosulfide ions, the results at the low temperature are not as affirmative as lignin, especially. While at higher temperature, such as at 160 °C, the fits are quite reasonable.

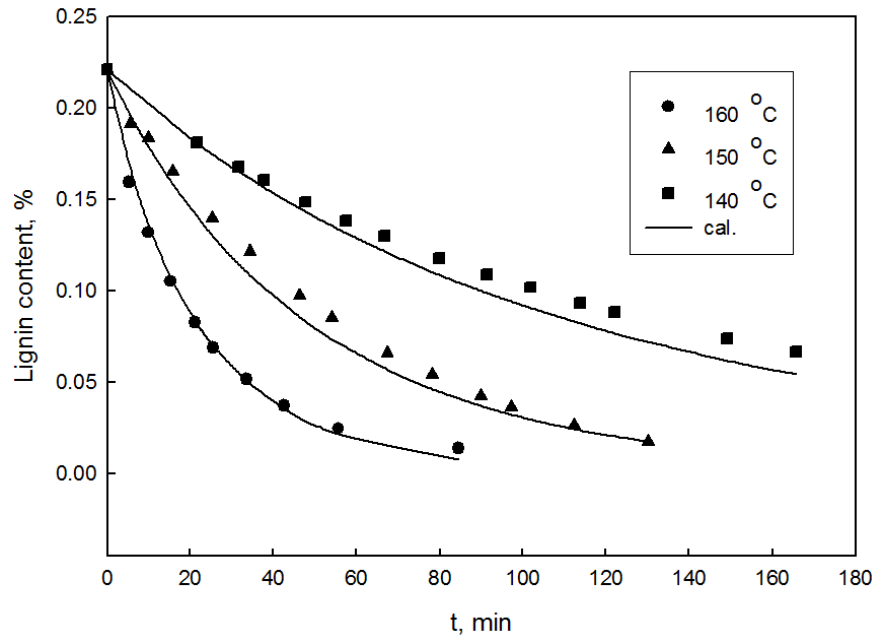


Figure 3-5 Lignin Removal at Different Temperatures with Low Liquor-to-wood Ratio(5:1)

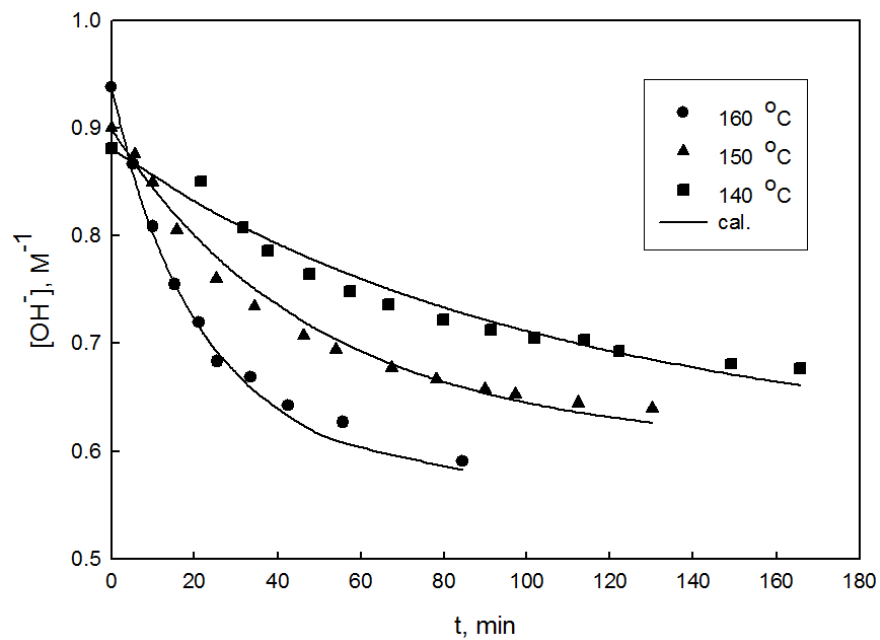


Figure 3-6 Effective Alkali Consumption at Different Temperature with Low Liquor-to-wood Ratio (5:1) vs Time

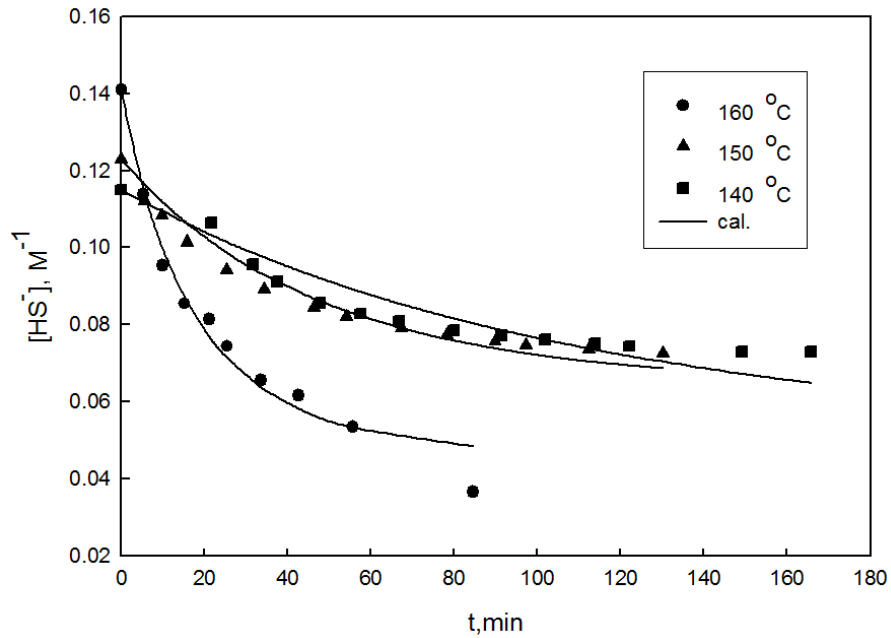


Figure 3-7 Hydrosulfide Ion Consumption at Different Temperature with Low Liquor-to-wood Ratio (5:1) vs Time

Figures 3-7, 8, and 9 compare the model predictions with the experimental data under high liquor-to-wood ratio.

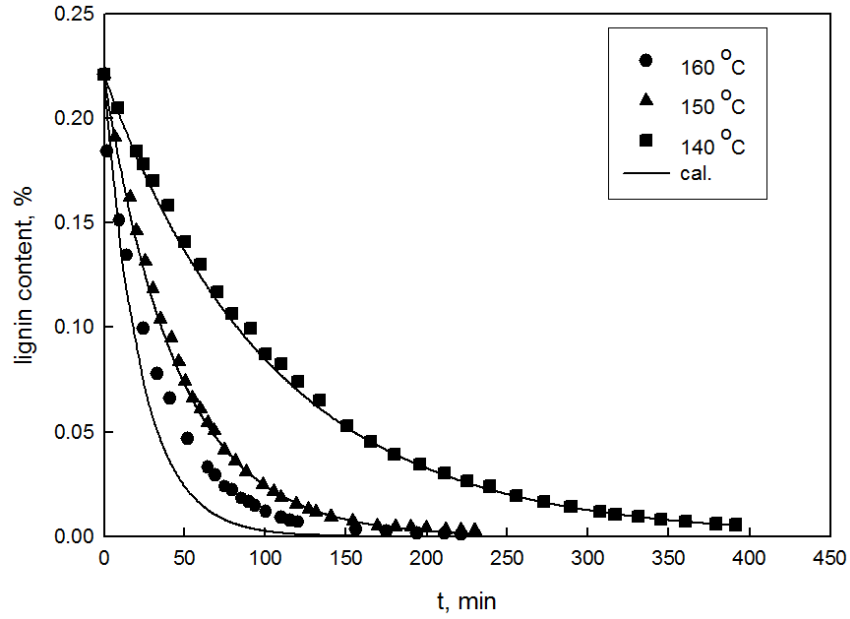


Figure 3-8 Lignin Removal Rate at Different Temperatures with High Liquor-to-wood Ratio (50:1). The symbols are Experimental Data of Santos, et al.

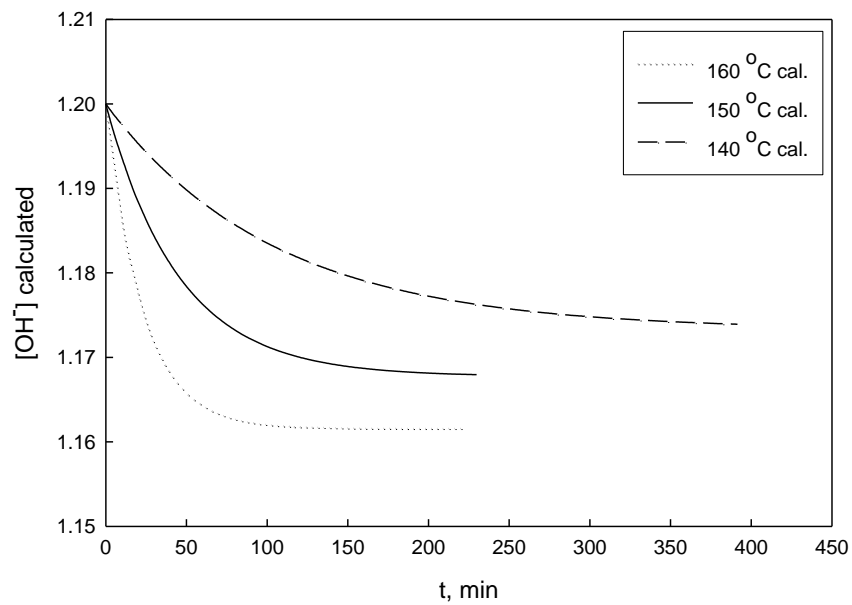


Figure 3-9 Effective Alkali Consumption at Different Temperature with High Liquor-to-wood Ratio (50:1) vs Time

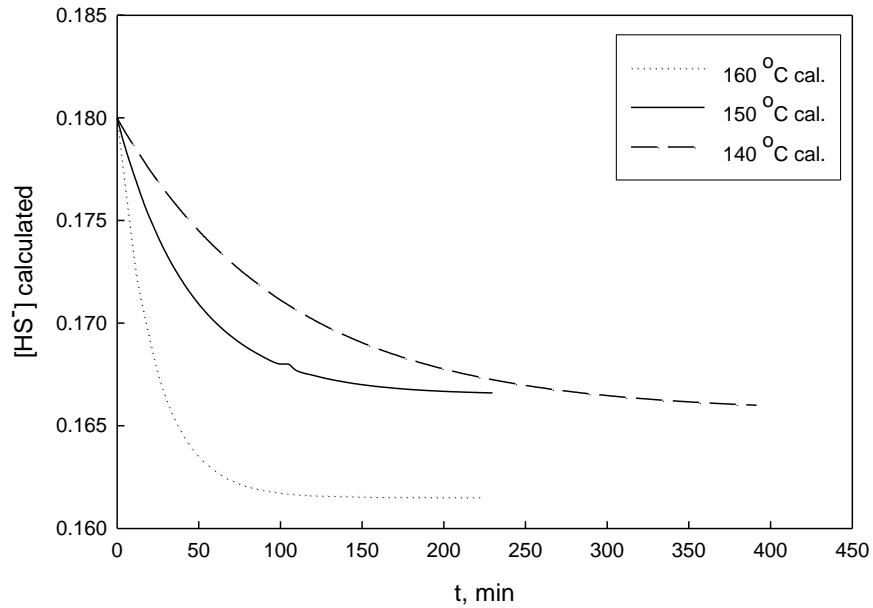


Figure 3-10 Hydrosulfide Consumption at Different Temperature with High Liquor-to wood Ratio (50:1) vs Time.

As can be seen from Figures 3-7, 8 and 9, the good agreement was achieved between the model prediction and the experimental data in three cases. It is also found that under high liquor-to-wood ratio of 50, the concentrations of hydroxide and hydrosulfide decrease slightly during cooking.

Wilder and Daleski (Wilder and Daleski 1965) carried out the experimental study on delignification kinetics of loblolly pine. In their work, the high liquor-to-wood ratio (200:1) was employed to keep the concentration of liquor composition constant, and thin wood shavings were used for digestion to eliminate the effect of liquor penetration and diffusion. As can be seen in Figure 3-10, the line fits experimental data very well.

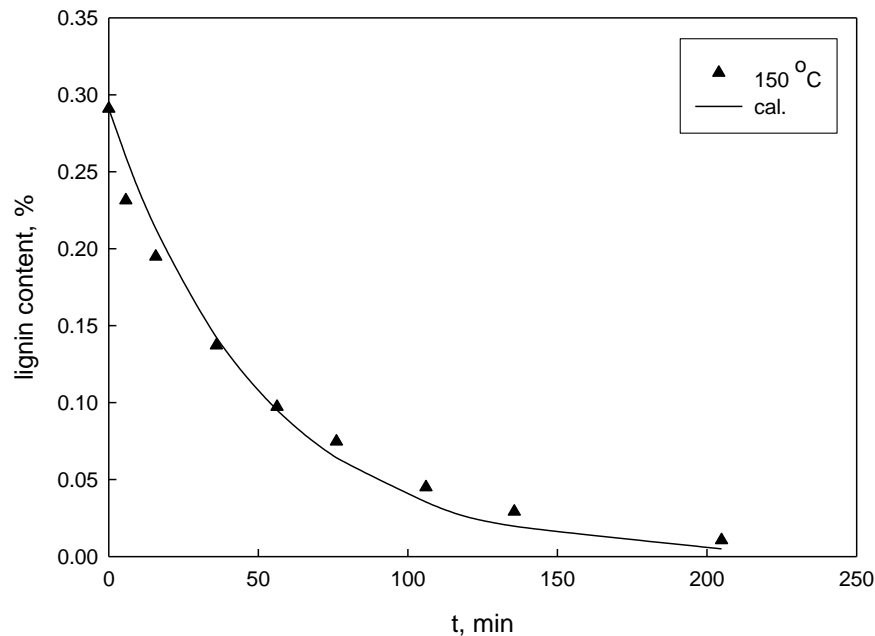


Figure 3-11 Lignin Removal Rate at High Liquor-to-wood Ratio (200:1)

### 3.4 Discussion

#### 3.4.1 Model Prediction at the Low Liquor-to-wood Ratio

The experimental data from Santo's work have been employed to compare with the model prediction at the low liquor-to-wood ratio of 5 (Figure 3-7, 8, and 9). As can be seen from Figures 3-7, 8, and 9, for all of the lignin test cases, the data fit rather well. But for the hydrosulfide ions, the results at the low temperature are not as affirmative as lignin, especially. While at higher temperature, such as at 160 °C, the fits are quite reasonable. Higher deviations occur for the model predictions of hydrosulfide ion at the low temperature (140 °C). The one reason for this behavior may be caused by the experiment error. As can be seen from Figure 3-4, the difference between the data of 140 °C and 150

$C$  is very small, although the reaction takes place at the different temperature. The other reason may attribute to the assumption made for model that the consumption of hydroxide and hydrosulfide ions by other components in wood is proportional to that by lignin. This assumption for hydrosulfide consumption may be somewhat weak at the low temperature. That means, introduction of proportional constant to explain the consumption of hydrosulfide by other components in wood chips may result in the error.

The calculated vs experimental lignin content and chemical concentrations under low liquor-to-wood ratio are shown in Figures 3-11, 12, and 13.

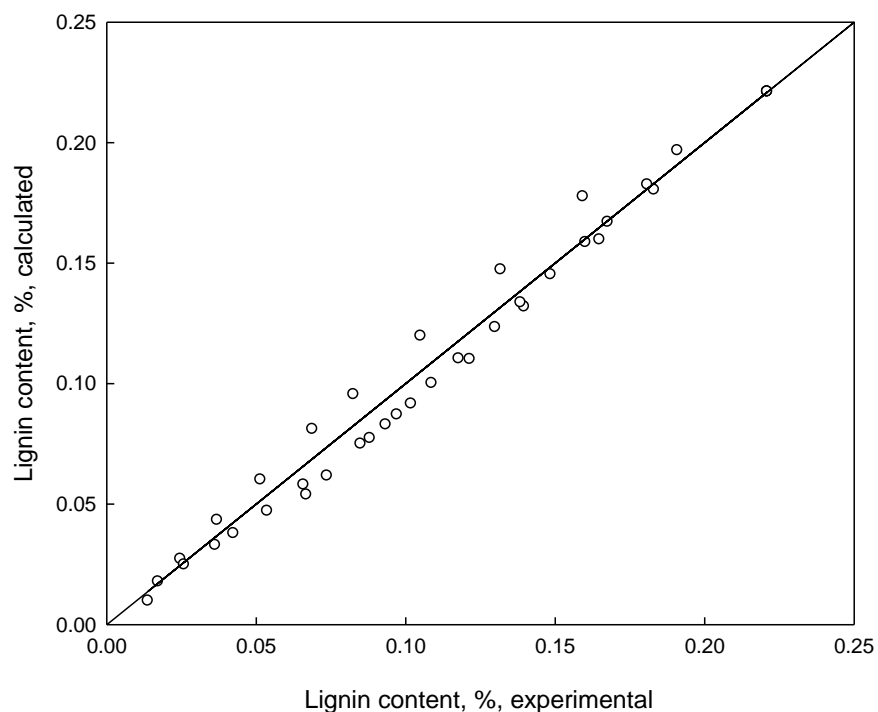


Figure 3-12 Calculated vs Experimental Lignin Content under Low Liquor-to-wood Ratio

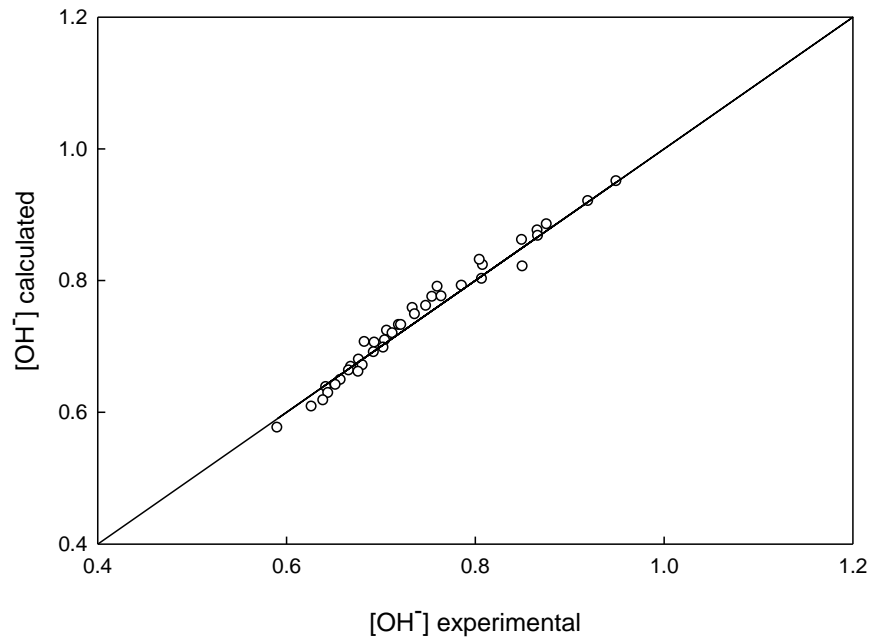


Figure 3-13 Calculated vs Experimental Hydroxide Concentration under Low Liquor-to-wood Ratio

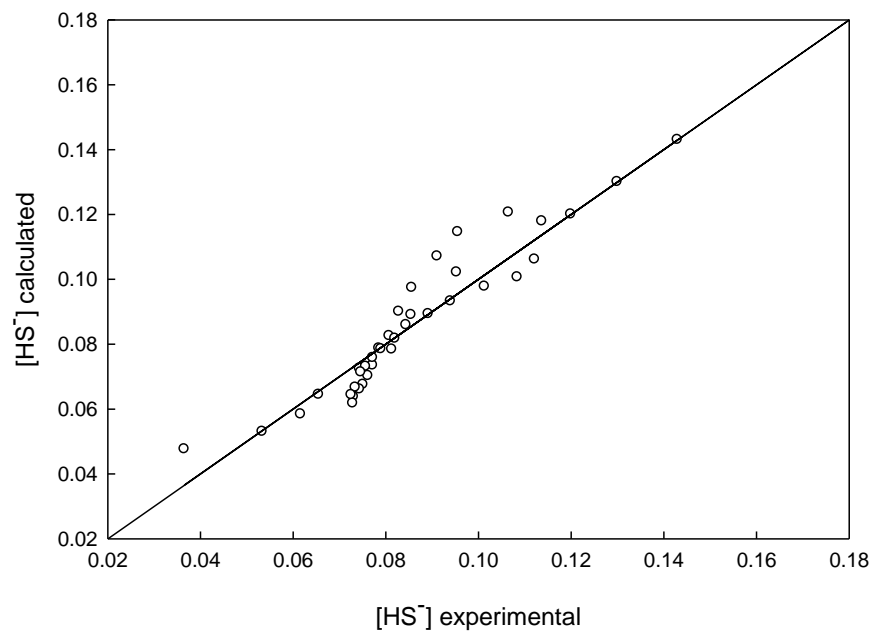


Figure 3-14 Calculated vs Experimental Hydrosulfide Concentration under Low Liquor-to-wood Ratio

In the work of Santos, et al., the proportionality factor between the consumption rate of hydroxide and delignification rate is 1.67 and 0.3 for initial and bulk delignification respectively, and the proportionality factor between the consumption rate of hydrosulfide and delignification rate is 0.44 and 0.042 for initial and bulk delignification respectively.

To make a comparison among the proportionality factors  $f_1$  and  $f_2$  with that in Santos's work, Equations (3-51) and (3-52) are rearranged into the similar fashion to that in Santos's work.

$$-\frac{d[\text{OH}^-]}{dt} = \frac{L_0 \times k_0}{\frac{V_L}{W} + \frac{k_0 K_1 L}{(1 + K_1 [\text{OH}^-])^2}} \left( f_1 - \frac{K_1 [\text{OH}^-]}{1 + K_1 [\text{OH}^-]} \right) \left( -\frac{d(1 - X_L)}{dt} \right) = F_1 \left( -\frac{d(1 - X_L)}{dt} \right) \quad (3-59)$$

$$-\frac{d[\text{HS}^-]}{dt} = \frac{L_0 \times k_0}{\frac{V_L}{W} + \frac{k_0 K_2 L}{(1 + K_2 [\text{HS}^-])^2}} \left[ \frac{f_2}{1 + \frac{k_3 (1 + K_2 [\text{HS}^-])}{K_2 k_4 [\text{HS}^-]}} - \frac{K_2 [\text{HS}^-]}{1 + K_2 [\text{HS}^-]} \right] \left( -\frac{d(1 - X_L)}{dt} \right) = F_2 \left( -\frac{d(1 - X_L)}{dt} \right) \quad (3-60)$$

Seen from the above equations,  $F_1$  and  $F_2$  are the function of the parameters, such as rate constant, and the proportionality factor  $f$  as well as the concentration of hydroxide and hydrosulfide ions. During the pulping process at the low liquor-to-wood ratio, the chemical concentrations undergo changes. That is,  $F_1$  and  $F_2$  aren't constant in our work. Although  $F_1$  and  $F_2$  change with cooking time, the results show that their changes are minimal. Therefore, the average values of  $F_1$  and  $F_2$  are shown in Table 3-4.

Table 3- 5 Proportionality Factors: F<sub>1</sub> and F<sub>2</sub>

T, °C	140	150	160
F <sub>1</sub>	0.274	0.331	0.397
F <sub>2</sub>	0.071	0.073	0.093

Compared with the value of proportionality factors in the work of Santos, F<sub>1</sub> and F<sub>2</sub> are not constant as the temperature is varied. As can be seen from Table 3-4, the values of F<sub>1</sub> and F<sub>2</sub> in our work are between the values of initial and bulk delignification in Santos, et al.

### 3.4.2 Heats of Adsorption and Activation Energy

According to the Arrhenius equation, the rate constant k conforms to the following equation:

$$k = Ae^{-E_a/RT} \quad (3-61)$$

Where E<sub>a</sub> is the activation energy for the irreversible reaction under consideration (Equations 3-21 and 3-22), for reversible reaction (Equations 3-19 and 3-20), it denotes the heat of the reaction. T is the absolute temperature. Taking natural logs of both sides,

$$\ln k = \ln A - \frac{E_a}{RT} \quad (3-62)$$

Plotting lnk versus (1/T), if straight line is obtained based on the model prediction, we think the kinetic model developed in this work is validated. Figure 3-17 shows the relationship between rate constant (or equilibrium constant) and reciprocal of temperature.

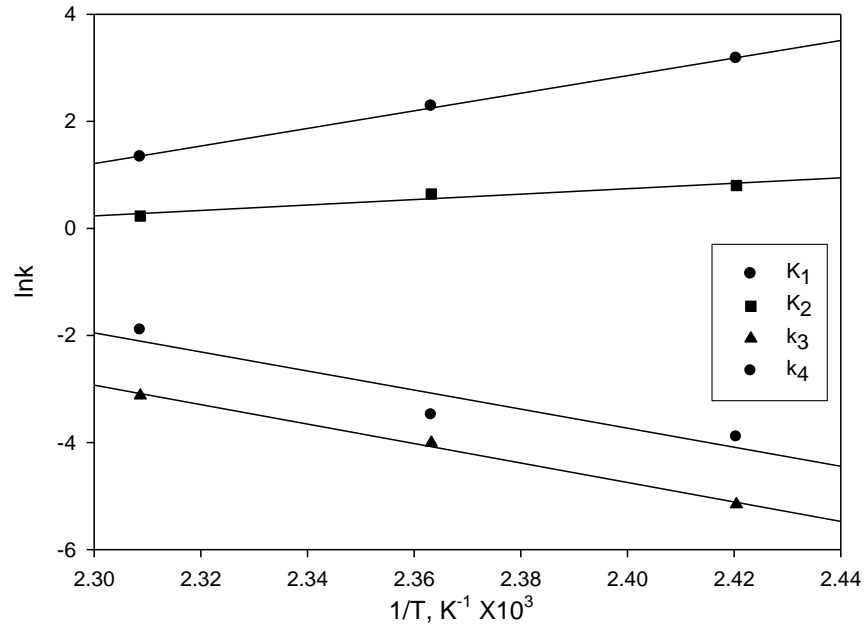


Figure 3-15 lnk versus Reciprocal of Temperature

It can be seen from Figure 3-14 that natural Log of rate constant is linear with the reciprocal of temperature. Equilibrium constant of chemisorption reactions (Equations. 3-19 and 3-20) increases with temperature decreases. This behavior can be explained those chemical adsorptions are exothermic. As the temperature of the system decreases, adsorption equilibrium moves to the production side, so the equilibrium constant increases. The activation energy (based on  $k_3$  and  $k_4$ ) or heat value (based on  $K_1$  and  $K_2$ ) can be obtained by the slope of straight lines, the calculation of responding parameters are shown in Table 3-5.

Table 3-6 Calculation of Activation Energy and Frequency Factors

	Eqn. 3-19	Eqn. 3-20	Eqn. 3-21	Eqn. 3-22
$\Delta H$ or $E_a$ (kJ/mol)	-46.96	-35.73	151.21	118.76
$\ln A$	-11.28	-9.88	39.07	29.85
correlation coefficient, $R^2$	0.97	0.90	0.99	0.99

### 3.5 Recommendations

In the present study, only a kinetic mechanism of delignification reactions was proposed. Degradation of carbohydrates was ignored in the kinetic model, and the change of the chemical concentration due to carbohydrate dissolution was incorporated in the kinetic mode by introducing the proportionality factors, and such treatment results in deviation at the low temperature. Therefore, both experimental and theoretical works are required to extend this work.

#### 3.5.1 Experimental Studies

Due to few of data of delignification in Kraft pulping were reported in the open literature, it is difficult to validate the model prediction with limited experimental data. Therefore, in order to obtain the comprehensive set of data, the sets of experiments will be inevitably required. Through the experimental studies, the data that the lignin content, carbohydrate content, and chemical concentration vary against time will be obtained at the different cooking temperatures.

The wood chemical composition is obtained as described in TAPPI test method, the chemical compositions of wood related to the project are: lignin

(TAPPI test method T222), Cellulose (TAPPI test method T203), Pentosans (TAPPI test method T223), Extractives (TAPPI test method T204), and ash (TAPPI test method T211). The lignin concentration in black liquors is determined by UV spectrophotometry (Alen and Hartus 1988; Kleinert and Joyce 1957; Trinh 1988).

### **3.5.2 Theoretical Studies**

As described in the subsection 3.2, a kinetic model was developed theoretically; and mass transfer in the pulping process has been ignored, which is reasonable when the thickness of the wood chips used in the cook is less than 2-3 mm. However, it is difficult to maintain the thickness of the commercial chips uniform but a chip-thickness distribution. Therefore, an accurate pulping model should integrate the pulping kinetics with transport of cooking chemical agents definitely. The further work is recommended to modify the existing kinetic model by incorporating a better equation for the diffusion of sodium hydroxide and sodium hydrosulfide.

## References

- Ahlgren, P., and Teder, A. (1967). "Delignification rate in polysulfide pulping." *Svensk Papperstidning*, 70(4), 135.
- Alen, R., and Hartus, T. (1988). "UV spectrophotometric determination of lignin from alkaline pulping liquors." *Cellulose Chem. Technol.*, 22, 613-618.
- Aurell, R., and Hartler, N. (1965). "Kraft pulping of Pine, part I. The changes in the composition of the wood residue during the cooking process." *Svensk Papperstidning*, 68(2), 59.
- Chiang, V. L., and Yu, J. (1989). "Isothermal reaction kinetics on Kraft delignification of Douglas-fir." *Wood and Pulping Chemistry*, 271-274.
- Christensen, T., Albright, L. F., and William, T. J. (1983). "A kinetics mathematical model for the Kraft pulping of wood." *Tappi Annual Meeting*, 15-20.
- Fleming, B. I., Kubes, G. J., Macleod, J. M., and Bolker, H. I. (1978). "Soda pulping with anthraquinone a mechanism." *Tappi J.*, 61(6), 43-46.
- Fleming, B. I., Kubes, G. J., Macleod, J. M., and Bolker, H. I. (1979). "Soda pulping with nitrogenous redox catalysts." *Tappi J.*, 62(6), 57-60.
- Giudici, R., and Park, S. w. (1996). "Kinetic model for Kraft pulping of hardwood." *Ind. Eng. Chem. Res.*, 35, 856-863.
- Green, R. P., and Prusas, Z. C. (1975). "Polysulphide pulping of two Canadian softwood blends." *Pulping and Paper Canada*, 76(9), 69-72.

- Gustafson, R. (1982). "A theoretical model of the Kraft pulping process." *Thesis of PhD, University of Washington*.
- Gustafson, R., Snelcher, C. A., Mckean, W. T., and Finlayson, B. A. (1983). "Theoretical model of the Kraft pulping process." *Ind. Eng. Chem. Process Des. Dev.*, 22, 87-96.
- Hatton, J. V. (1973). "Development of yield prediction equations in Kraft pulping." *Tappi J.*, 56(7), 97-100.
- Hatton, J. V., and Keays, J. L. (1973). "Effect of chip geometry and moisture on yield and quality of Kraft pulps from western hemlock and black spruce." *Pulping and Paper Magazine of Canada*, 74(1), 79-87.
- Holton, H. H., and Chapman, F. L. (1977). "Kraft pulping with anthraquinone." *Tappi J.*, 60(11), 121-125.
- Jiang, E. J. (1996). "Extended delignification of southern pine with anthraquinone and polysulfide." *Tappi J.*, 78(2), 126-133.
- Kerr, A. J. (1970). "The kinetics of Kraft pulping progress in development of a mathematical model." *Appita*, 24(3), 180-188.
- Kerr, A. J., and Uprichard, J. M. (1976). "The kinetics of Kraft pulping refinement of a mathematical model." *Appita*, 30(1), 48-54.
- Kleinert, T. N. (1966). "Mechanism of the alkaline delignification, I. the overall reaction pattern." *Tappi J.*, 49(2), 52-57.
- Kleinert, T. N., and Joyce, C. S. (1957). "Short wavelength ultraviolet absorption of various lignin and related substances, IV. Lignin determination in sulphate pulping liquors." *Pulping and Paper Magazine of Canada*(October), 147-152.

- Larocque, G. L., and Maass, O. (1941). "the mechanism of the alkaline delignification of wood." *Canadian Journal of Research*, 19, 1-15.
- Lemon, S., and Teder, A. (1973). "Kinetics of the delignification in Kraft pulping: I. Bulk delignification of pine." *Svensk Papperstidning*, 11, 407-414.
- Li, Z., Li, J., and Kubes, G. J. (2002). "Kinetics of delignification and cellulose degradation during Kraft pulping with polysulphide and anthraquinone." *JPPS*, 28(7), 234-239.
- Liu, S. (2004). "Parametric estimation and error structure, Dyn. Cont., Discrete impulsive system." *Ser. B: Applied Algorithms*, 11(1), 1.
- Ljunggren, S. (1980). "The significance of aryl ether cleavage in Kraft delignification of softwood." *Svensk Papperstidning*, 83(13), 363-369.
- Macleod, J. M., Fleming, B. I., Kubes, G. J., and Bolker, H. I. (1980). "The strengths of Kraft-AQ and Soda-AQ pulps bleachable-grade pulps." *Tappi J.*, 61(1), 57-60.
- Macleod, J. M., and Kingsland, K. A. (1990). "Kraft-AQ pulping of sawdust." *Tappi J.*, 73(1), 191-193.
- Norden, S., and Teder, A. (1979). "A modified Kraft processes for softwood bleached-grade pulp." *Tappi J.*, 62(7), 49-51.
- Obiaga, T. I., and Wayman, M. (1969). "Kraft and polysulphide delignification of a tropical hardwood." *Pulping and Paper Magazine of Canada*, 70(16), 64-72.

- Obst, H. R., Landucci, L. L., and Sanyer, N. (1979). "Quinones in alkaline pulping,  $\beta$ -Ether cleavage of free phenolic units in lignin." *Tappi J.*, 62(1), 55-59.
- Olm, L., and Tistad, G. (1979). "Kinetics of the Initial Phase of Kraft pulping." *Svensk Papperstidning*, 87(5), 458.
- Parthasarathy, V. R., Smith, G. C., Rudie, G. F., Detty, A. E., and Steffy, J. J. (1995). "Application of anthraquinone in extending the delignification of Kraft and polysulfide pulps, Part 1. Pulping and bleaching of mixed hardwoods." *Tappi J.*, 78(2), 113-125.
- Pekkala, O. (1982). "The extended delignification using polysulfide or anthraquinone in Kraft pulping." *Paperi Ja Puu-Paper and Timber*, 64(11), 735.
- Rekunen, S., Jutila, E., Lahtenmaki, E., Lonnberg, B., and Virkola, N. E. (1980). "Examination of reaction kinetics in Kraft cooking." *Paperi Ja Puu-Paper and Timber*, 2, 80.
- Santos, A., Rodriguez, M. A., Moreno, D., and Garcia-Ochoa, F. (1997). "Kinetic modeling of Kraft delignification of eucalyptus globules." *Ind. Eng. Chem. Res.*, 36, 4114.
- Sjostom, E. (1981). "Wood Chemistry, Fundamentals and Applications." *Academic, New York*.
- Smith, C. C., and William, T. J. (1974). "Mathematical modeling simulation and control of the operation of a Kamyr continuous digester for the Kraft process." *Thesis of PhD, Purdue University*.

- Smook, G. A. (2002). "Handbook for Pulp & Paper Technologists, 3rd Edition."
- Trinh, D. T. (1988). "The measurement of lignin in Kraft pulping liquors using an automatic colorimetric methods." *JPPS*, 14(1), 19-22.
- Varma, V., and Krishnagopalan, A. (1998). "Kinetics of extended delignification using alkali profiling and on-line liquor analysis." *Appita*, 51(1), 50.
- Vroom, K. E. (1957). "The H-factor: a means of expressing cooking times and temperature as a single variable." *Pulping and Paper Canada*, 58, 228-231.
- Wilder, H. D., and Daleski, E. J. (1964). "Kraft pulping kinetics, Part I. Literature review and research program." *Tappi J.*, 47(5), 270-275.
- Wilder, H. D., and Daleski, E. J. (1965). "Delignification rate studies, Part II. of a series on Kraft pulping kinetics " *Tappi J.*, 48(5), 293-297.

## APPENDIX A Reaction of Model Compounds of Naphthenic Acids

Butyric acid was initially selected as a model compound, and decane was used as the solvent of butyric acid to achieve desired concentration. The effects of the reaction temperature (100-150 °C), catalyst loading (5-15% wt), and the concentration of butyric acid (0.2-2%) on the decarboxylation of butyric acid were investigated. The diagram of the experimental setup is shown in Figure A-1. The mixture of butyric acid and decane in an open flask with three angle necks was heated, and the temperature was controlled by the temperature controller (digital II heat controllers from Sigma). The products at different reaction time were sampled and analyzed by a gas chromatography (GC, Hewlett Packard-5890 with FID) to observe the concentration change of butyric acid against the reaction time.

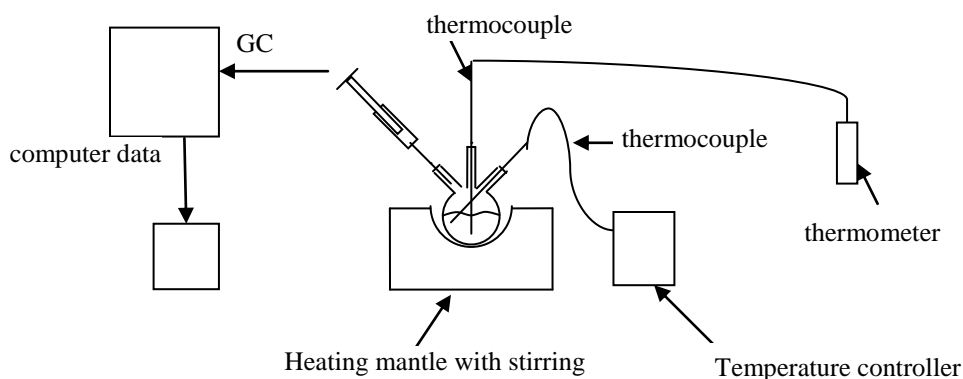
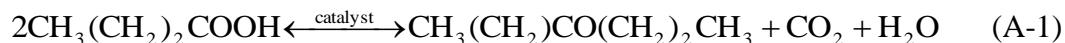


Figure A-1 Schematic of the Experimental Setup for the Model Compound Reaction System

The expected decarboxylation reaction is illustrated by Equation (A-1)



Therefore, the main product is 4-heptanone. In GC analysis, in order to separate the peaks of reactants and main products well, several different temperature programs containing one or more isothermal and ramp stages were tried to improve detectability of all components. The mixture of decane (Aldrich, 99+%) and butyric acid (Aldrich, 99+%) and 4-heptanone (Aldrich, 98%) was prepared as the sample and analyzed by GC to optimize the temperature program. The optimized temperature program is shown in Figure A-2, and the chromatogram at the optimized condition is shown in Figure A-3.

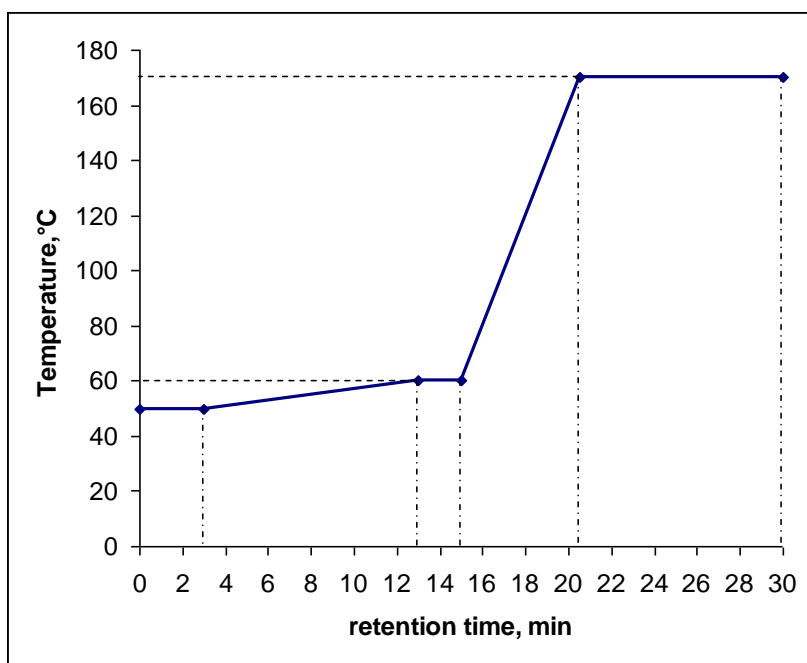


Figure A-2 The Optimized Temperature Program for GC

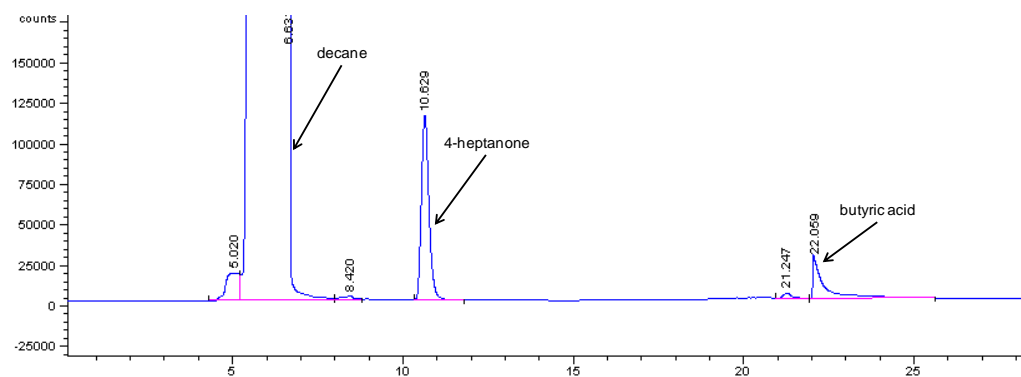


Figure A-3 Chromatogram of the Mixture of Decane and Heptanone and Butyric Acid

As can be seen from Figure A-3, the retention time of decane, 4-heptanone, and butyric acid are 6.631, 10.629 and 22.059 minutes at the operation condition, respectively.

The mixture of butyric acid (2 volume%) and decane was transferred to the flask and heated up at 150 °C. 0.2  $\mu\text{L}$  of solution was sampled and analyzed by GC to obtain the chromatogram of the reactants at the initial time. Then certain amounts of catalysts were added, and the reaction was timed. During the reaction, the samples at the different reaction time were taken out and injected into GC to trace the concentration of butyric acid and the product components. There are 35 min apart between two sampling because each GC run lasts 30 min, and 5 min was needed for a stable baseline restoring.  $\text{Li}_2\text{O}/\text{TiO}_2$  extrudates, commercial  $\text{Li}_2\text{O}$  and  $\text{CaO}$  were employed as catalyst and tested in the experimental runs. The typical chromatogram of the reaction with addition of  $\text{Li}_2\text{O}/\text{TiO}_2$  is shown in Figure A-4.

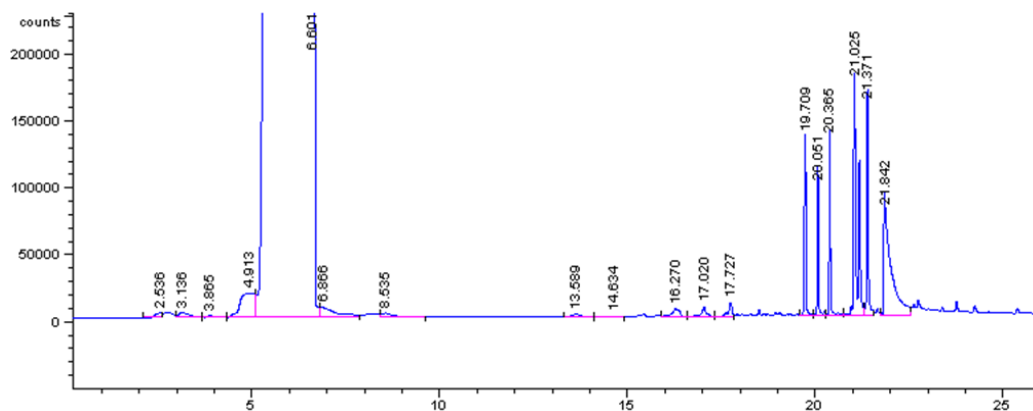


Figure A-4 Chromatogram of the reaction products

As data shown in Figure A-4, no peak was found at 10.629 minutes which corresponds to the retention of 4-heptanone. Therefore, no heptanone was produced under the reaction conditions. The reason for no heptanone produced in liquid-phase reaction could be that the temperature of the liquid-phase reaction is much lower than that of gas phase, although the ketonization happens in gas phase in the presence of  $\text{Li}_2\text{O}/\text{TiO}_2$  (Schommer et al. 1990). Therefore, the reaction temperature was increased. In Guarino's work (Guarino 2006), it has been observed that the ketonization reaction took place at over  $360\text{ }^\circ\text{C}$  in the presence of  $\text{MgO}$ . Due to the critical temperature limitation imposed by butyric acid and decane ( $T_c$  of butyric acid is  $342.5\text{ }^\circ\text{C}$  and that of decane is  $344.6\text{ }^\circ\text{C}$ ), it is not practical to keep butyric acid and decane in the liquid phase at the temperature of  $350\text{ }^\circ\text{C}$  or higher even with increasing the pressure. Therefore, butyric acid and decane were substituted by NA and carrier oil which are stable at temperatures approaching  $400\text{ }^\circ\text{C}$ .

## **APPENDIX B Simulation of Vapor-Liquid Equilibria of Model System Using HYSYS**

To predict reaction conditions in which decarboxylation reaction of the carrier oil mixture system occurs in the liquid phase at the certain reaction temperature, the vapor-liquid equilibria of the oil mixture was simulated by using HYSYS.

Boiling point (BP) distribution of NA was analyzed by using ASTM 2887 at the National Center of Upgrading Technology, Canada. The BP distribution is listed in the Table B-1. BP distribution of carrier oil (Table B-2) was provided by the supplier. The simulation results of HYSYS are listed in Table B-3.

Table B-1 Boiling Point Distribution of NA

Mass,%	BP, °C						
0.5	147.4	26	273	52	306.4	78	330.6
1	160.2	27	275.2	53	307.4	79	331.6
2	175.6	28	277	54	308.2	80	332.6
3	189.2	29	278.6	55	309.2	81	333.6
4	194.6	30	280.6	56	310	82	334.8
5	199.4	31	282.2	57	311	83	336.2
6	207.2	32	283.6	58	311.8	84	337.4
7	208.8	33	285.2	59	312.8	85	338.8
8	213.2	34	286.4	60	313.8	86	340.2
9	215.6	35	287.8	61	314.6	87	341.8
10	221.6	36	289	62	315.4	88	343.6
11	224.8	37	290.4	63	316.2	89	345.2
12	228.8	38	291.6	64	317.2	90	347.2
13	231.8	39	292.8	65	318	91	349.4
14	236.6	40	294	66	318.8	92	352.2
15	241	41	295.2	67	320	93	355.2
16	244.8	42	296.4	68	320.8	94	359.2
17	248.2	43	297.4	69	321.6	95	364.8
18	252.2	44	298.4	70	322.6	96	374.2
19	255.6	45	299.4	71	323.6	97	388.6
20	258.8	46	300.6	72	324.4	98	411.2
21	261.6	47	301.6	73	325.4	99	466
22	264.2	48	302.4	74	326.4	99.5	509.8
23	266.6	49	303.4	75	327.4		
24	269	50	304.4	76	328.4		
25	270.8	51	305.4	77	329.4		

\

Table B-2 BP Distribution of the Carrier Oil

Mass,%	BP, °C						
IBP	362.5	26	470.5	52	502.0	78	532.5
1	373.0	27	472.0	53	503.0	79	533.5
2	387.5	28	473.5	54	504.0	80	535.0
3	397.5	29	475.0	55	505.0	81	536.5
4	405.0	30	476.0	56	506.0	82	538.0
5	411.0	31	477.5	57	507.0	83	539.5
6	416.5	32	479.0	58	508.5	84	541.0
7	421.0	33	480.0	59	509.5	85	543.0
8	425.5	34	481.5	60	510.5	86	544.5
9	429.5	35	482.5	61	511.5	87	546.5
10	433.0	36	484.0	62	512.5	88	548.5
11	436.5	37	485.0	63	514.0	89	550.5
12	439.5	38	486.5	64	515.0	90	553.0
13	442.5	39	487.5	65	516.0	91	555.0
14	445.0	40	488.5	66	517.0	92	558.0
15	448.0	41	490.0	67	518.5	93	560.5
16	450.5	42	491.0	68	519.5	94	563.5
17	453.0	43	492.0	69	520.5	95	567.0
18	455.0	44	493.0	70	522.0	96	571.0
19	457.5	45	494.5	71	523.0	97	576.0
20	459.5	46	495.5	72	524.5	98	583.0
21	461.5	47	496.5	73	525.5	99	594.0
22	463.5	48	497.5	74	527.0	99.5	605.5
23	465.5	49	498.5	75	528.0		
24	467.0	50	499.5	76	529.5		
25	469.0	51	501.0	77	531.0		

Table B-3 Results of HYSYS Simulation of the Mixture of NA and Carrier oil with Different TAN at 385 °C

Stream name	TAN=3	TAN=45
Vapour/phase fraction	0	0
Temperature, C	385	385
Pressure, kPa	36.33	249.9
Molar flow,kgmole/h	1.866e-3	2.841e-3
Mass flow, kg/h	1.015	1.25
Std ideal liq vol flow, m <sup>3</sup> /h	1.171e-3	1.448e-3
Molar enthalpy, kJ/kgmole	-6.137e5	-5.014e5
Molar entropy, kJ/kgmole-C	2543	1958
Heat flow, kJ/h	-1145	-1425
Liq vol flow at std cond, m <sup>3</sup> /h	1.175e-3	1.507e-3

Based on the calculation of HYSYS, when the temperature reaches 385 °C, the saturated pressure of the mixture of NA and carrier oil with TAN of 3 is 36 kPa, and for a mixture of NA and carrier oil with TAN of 45, the vapor pressure is 250 kPa.

## APPENDIX C Reaction of the Model System in A Parr Reactor

In view of the bad leak proofness and small capacity of the micro reactor, a system including a Parr reactor with the capacity of 500 ml was designed for the kinetic study. The Parr reactor was used as a semibatch in which multiple gas and liquid samples could be taken out of the reactor for analysis with reactions undergoing. The experimental setup including a Parr reactor is shown in the Figure C-1.

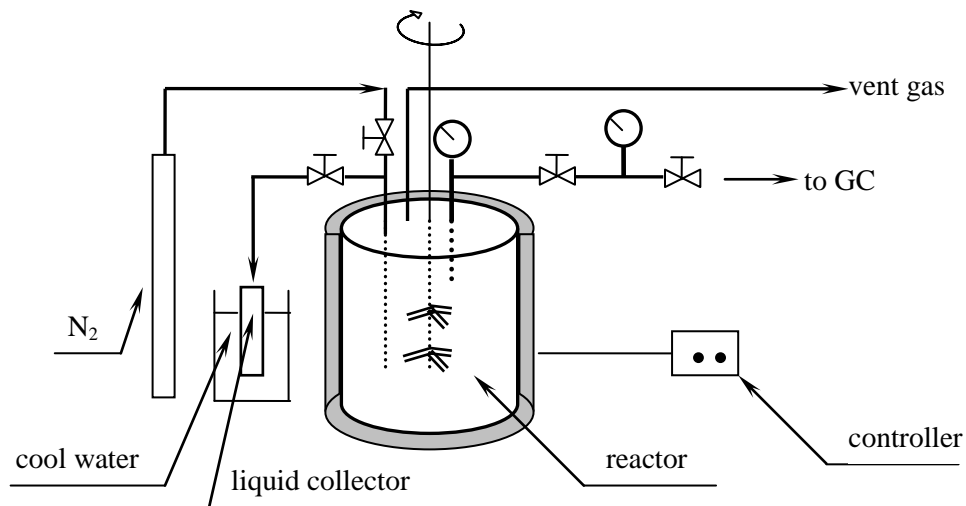


Figure C-1 Parr Reactor System

The mixture of NA and carrier oil with certain mixing ratio was introduced in the reactor, and the certain amount of CaO was charged in the reactor. After the reactor is hooded and tightened up, it was placed in the heater. Nitrogen as an inert gas was applied to purge air, and the reactor was pressurized at 250 psia. Turn the stir operating at 60 rpm for a little while to mix NA, oil ,

and CaO very well. And then Heat the reactor up at about 8.5 °C/minute (heating control set at II) to reach 300 °C, then at about 3 °C/minute (heating control set at I) to reach the reaction temperature, and 385 °C was applied for the preliminary run. Once the temperature of the reactor reached the reaction temperature, started the timing as the initial time, and collected the liquid and gas samples. The liquid collector, pre-purged by Nitrogen, is kept in cool water to quench the reaction. TAN of the liquid samples were measured by an automatic titrator to monitor the acid change. The gas samples were injected in GC to trace the formation of CO<sub>2</sub>. With the reaction running, the liquid and gas samples were collected every 30 minutes. Between two collections of liquid samples, the tubing was firstly blew with nitrogen to remove the dead volume left during the last collection, and then flushed with the liquid in reactor. After a reaction finished, the spent solid samples were analyzed by TGA to trace the formation of calcium naphthenate.

After a trial in the new design, it was found that although continuous samplings were accomplished, the pressure in the reactor dropped down significantly upon each sampling, the reaction conditions could not be kept consistent within the Parr reactor system. Moreover, it took more than 60 minutes for a reaction system to reach the reaction temperature, which was too long to make assumption of isotherm reaction reasonable. Therefore, this design was abandoned, and the kinetics of decarboxylation was also studied experimentally using a microbatch reactor.

## APPENDIX D Calibration Curve of TAN Measurement

Five mixtures of NA and carrier oil with different mixing ratio were prepared. The TAN of each mixture was measured by following the procedure of ASTM standard method D664. The TAN versus concentration of NA was plotted to give the calibration curve of TAN measurement (Figure D-1).

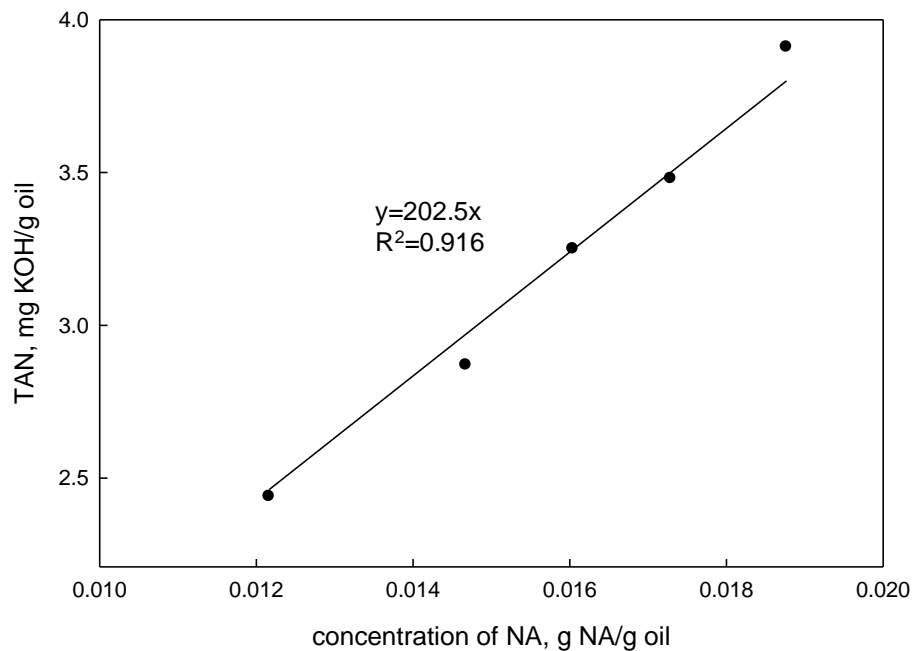


Figure D-1 Calibration Curve for TAN Measurement Relating TAN of Oil Sample and Mass Ratio of NA to Carrier Oil

## APPENDIX E GC Calibration Curves

To obtain the calibration curves of nitrogen and carbon dioxide in GC analysis, different volume of nitrogen and carbon dioxide with high purity were injected into GC, respectively. The peak areas corresponding to nitrogen and carbon dioxide versus the injected volume were plotted to obtain the calibration curves Figure E-1 and E-2.

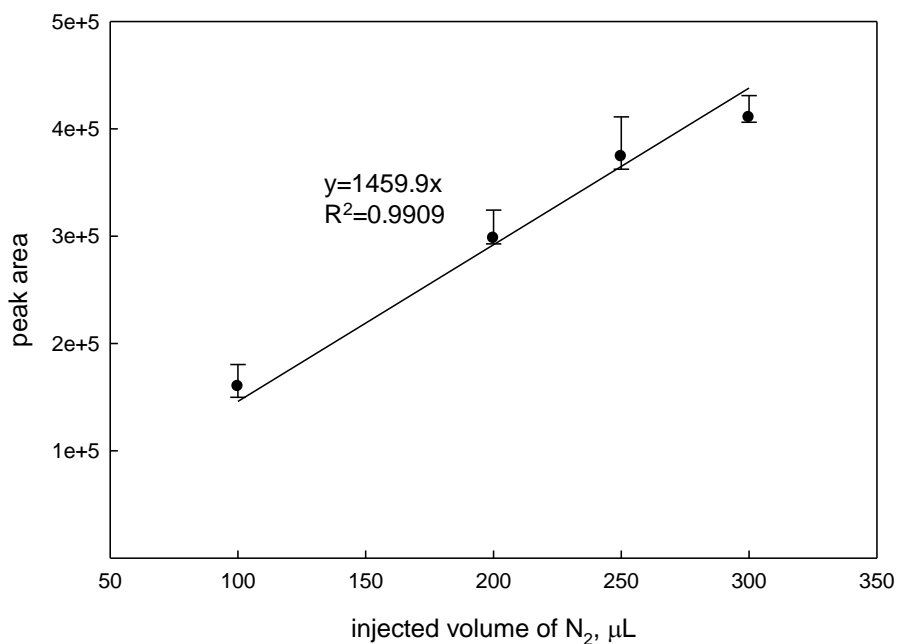


Figure E-1 Calibration Curve for Nitrogen Relating Peak Area Registered by GC and Volume of Nitrogen injected

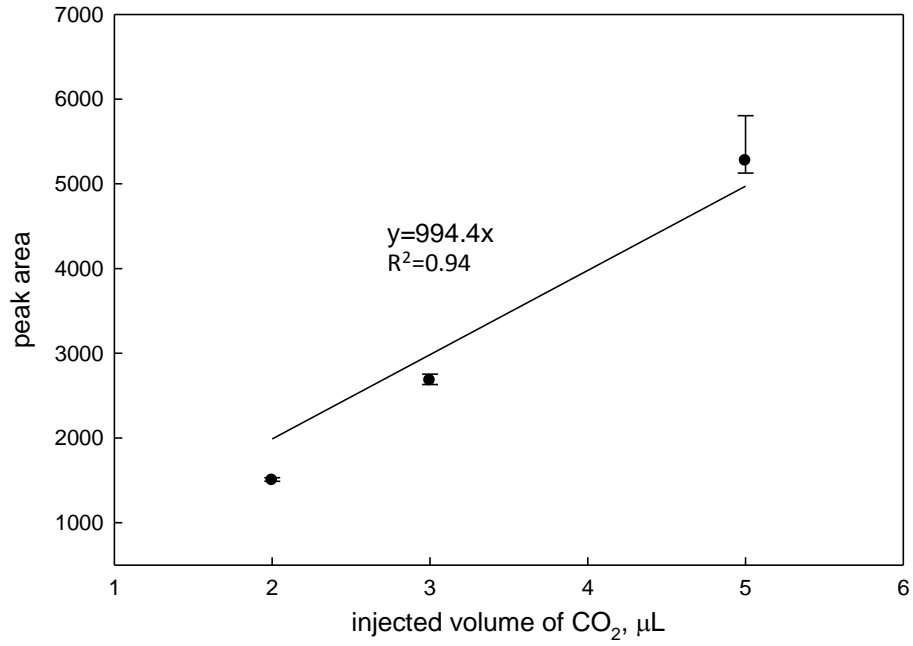


Figure E-2 Calibration Curve for Nitrogen Relating Peak Area Registered by GC and Volume of Nitrogen injected.